Hydroclimate variability and environmental change in Eurasia over the past millennium and its impacts

Mukund Palat Rao

Submitted in partial fulfillment of the
requirements for the degree of
Doctor of Philosophy
under the Executive Committee
of the Graduate School of Arts and Sciences

COLUMBIA UNIVERSITY

2020

Abstract

Hydroclimate variability and environmental change in Eurasia

over the past millennium and its impacts

Mukund Palat Rao

Streamflow records in many regions of Eurasia including South Asia are short and fragmentary. This makes it challenging to contextualise natural climate variability relative to anthropogenic climate change and evaluate the severity of recent extreme events. In the first section of the dissertation (Chapter 1 and 2) we use tree rings to reconstruct centennial-scale streamflow of the Indus and Brahmaputra Rivers in South Asia for the past six centuries. These two rivers and their tributaries are fed by Himalayan glaciers and the South Asian Monsoon and are the basis of economic, social, and cultural life of over 700 million people in the region. These centennial reconstructions of past discharge provide valuable information about long-term hydroclimate variability, drought and flood hazard. They also help us to interpret recent climate extremes relative to those in the past and benchmark projections of climate change for the region.

Large tropical (and extratropical) volcanic eruptions can release large quantities of reflective sulphate aerosols into the stratosphere where they may persist for up to 3 years. In Chapter 3 we discuss how these aerosols can impact European and Mediterranean hydroclimate by causing dry conditions over northwestern Europe and the British Isles and wet conditions over the western Mediterranean. We examine this hydroclimate response using Superposed Epoch Analysis (SEA), a statistical method used to identify consistent responses to events by testing for the possibility of random occurrence. Finally, in Chapter 4 we describe in further detail (cf.

Chapter 3) the modified double-bootstrap SEA that we developed in Chapter 3 to examine the uncertainty inherent in SEA within a probabilistic framework. We describe our modified SEA by applying it to two datasets, a reconstruction of northern hemisphere summer temperature for the past millennium, and a compilation of tree ring fire scar records for the western U.S. Using these two datasets we examine post-eruption northern hemisphere cooling following volcanism and the synchrony between drought conditions and fire events in the western U.S. respectively.

Table of Contents

List of Figures

1950-2002 (in black). Red lines represent monthly c.) North Atlantic Oscillation (NAO) and d.) East Atlantic Pattern (EAP) index data from the NOAA-CPC dataset for the same time period. Pearson correlations between c.) NOAA-CPC monthly NAO and PC1 and d.) NOAA-CPC monthly EAP and PC4 are 0.75 and 0.73 respectively (p=0, N=636, 2-sided Student's t-test). 174

List of Tables

Acknowledgments

I am very grateful to my thesis committee Dr. Edward Cook, Dr. Rosanne D'Arrigo and Prof. Kevin Griffin and to Dr. Benjamin Cook for their support and mentorship over the past few years. This work would been impossible without their guidance and encouragement. I would not be here if it were not for Prof. Nicole Davi and Dr. Brendan Buckley who introduced me to the fascinating world of tree-rings. I am also thankful to my external committee members Dr. Dorothy Peteet and Dr. Naresh Devineni.

I would also like to thank my friends and colleagues at the Tree Ring Lab and Griffin-Boelman Labs, my academic home here at Columbia. I also benefitted immensely from interactions with faculty, students, and post-docs in the Department of Earth and Environmental Science (DEES), Department of Ecology, Evolution, and Environmental Biology (E3B), Lamont-Doherty Earth Observatory (LDEO), and the M.A. programme in Climate and Society at Columbia University. I am also very thankful to my colleagues and collaborators who have contributed to the research presented here.

I am deeply grateful to my parents, sister, Mili Rodriguez, and to my extended family for their continuous and unwavering support and love.

This research was made possible by support from DEES, the Biology and Paleoenvironment (BPE) division at LDEO, and the Graduate School of Arts and Science (GSAS) at Columbia University. I also acknowledge the following funding sources: National Science Foundation (#1737788, #1303976, #1137729), the Lamont Climate Center, the Lamont Chevron Student Initiative Fund.

Dedication

In memory of my grandmother Kalyani Madhavan for her unconditional love.

Introduction

Variability in the width of annual tree rings and their many other wood properties are influenced by climate variability [*Fritts*, 1976]. The most limiting climate factor is the one that exerts the primary control on tree growth. This principle is known as Leibig's Law of the Minimum [*Liebig*, 1841]. The primary climate variables that control tree-growth across the world are most commonly found to be local soil moisture conditions and growing season temperature [*St. George and Ault*, 2014]. The factors that control which climate variable is most 'limiting' can however depend on the site location, local climatology, species, the wood parameter used (e.g. ring-width, isotopes, density), and the individual trees [*Buckley et al.*, 1997; *Bunn et al.*, 2018; *Gagen et al.*, 2006; *Pederson et al.*, 2004; *Stine*, 2019].

In a similar fashion river discharge and its seasonality are also controlled by climate variables [*Dettinger and Diaz*, 2000]. The most relevant climate variables are commonly precipitation (rain and or snow), temperature, and evapotranspiration. When tree growth and river streamflow are under similar climatic controls, tree rings can be used to reconstruct past river discharge [*Martin et al.*, 2019; *Meko et al.*, 1995]. Climate variables that can drive both river discharge and tree-growth may include winter snowpack and summer temperatures [e.g. *Woodhouse and Lukas*, 2006], summer hydroclimate [e.g. *Cook and Jacoby*, 1983; *Devineni et al.*, 2013], and monsoonal precipitation [e.g. *D'Arrigo et al.*, 2011].

Some of the earliest efforts to reconstruct past streamflow using tree rings were for the Colorado River in the United States (U.S.) by *Schulman* [1942] and by *Stockton and Jacoby* [1976] (also see [*Stockton*, 1971]). In their work *Stockton and Jacoby* [1976] found that long term reconstructed mean flow of the Colorado River was ~10% lower than average observed instrumental flows up to that point. Their findings helped elucidate how instrumental

observations of discharge that were used to allocate Colorado River water among U.S. basin states in the Colorado River Compact of 1922 (México was initially excluded) were among the wettest of the past 400 years. Impacts of the overallocation of Colorado River water beyond what is 'naturally' available in the system have had serious consequences [*Owen*, 2017] that are now being exacerbated by climate change [*Milly and Dunne*, 2020; *Woodhouse et al.*, 2016b].

The relevance of developing longer-term streamflow records is particularly high in the context of South Asia. Gauged records of streamflow in South Asia are limited, with few gauged records longer than 20 years [*Dettinger and Diaz*, 2000]. This leaves a large gap in our understanding of long-term decadal to centennial-scale natural climate variability in the region. At the same time human society in the South Asian countries of Bangladesh, India, and Pakistan experience some of the highest water scarcity in world due in part to a combination of strong seasonality in the availability of fresh water, the high human pressure on the resource, and the lack of built storage capacity [*Mekonnen and Hoekstra*, 2016].

The Indus River and the Brahmaputra River flank the western and eastern edges of the Himalaya. Along with the Ganga River they are among the most important perennial South Asian rivers that originate in the Himalaya [*Amrith*, 2018]. Despite starting close to the same glacial complex near Lake Mansarovar, the Indus and Brahmaputra rivers have contrasting fates [*Pranavananda*, 1939]. The Indus flows westwards through western Tibet and India, and then south through Pakistan where it drains into the Arabian Sea. The Brahmaputra on the other hand flows eastwards along the Tibetan Plateau, and then exits southwards through northeastern India and Bangladesh where it drains into the Bay of Bengal. Additionally, while most of the Indus watershed is arid to semi-arid and receives less than 1,000 mm mean annual precipitation, the

Brahmaputra watershed is among the wettest in the world with some regions receiving in excess of 5,000 mm/year of precipitation (Figure 0.1).

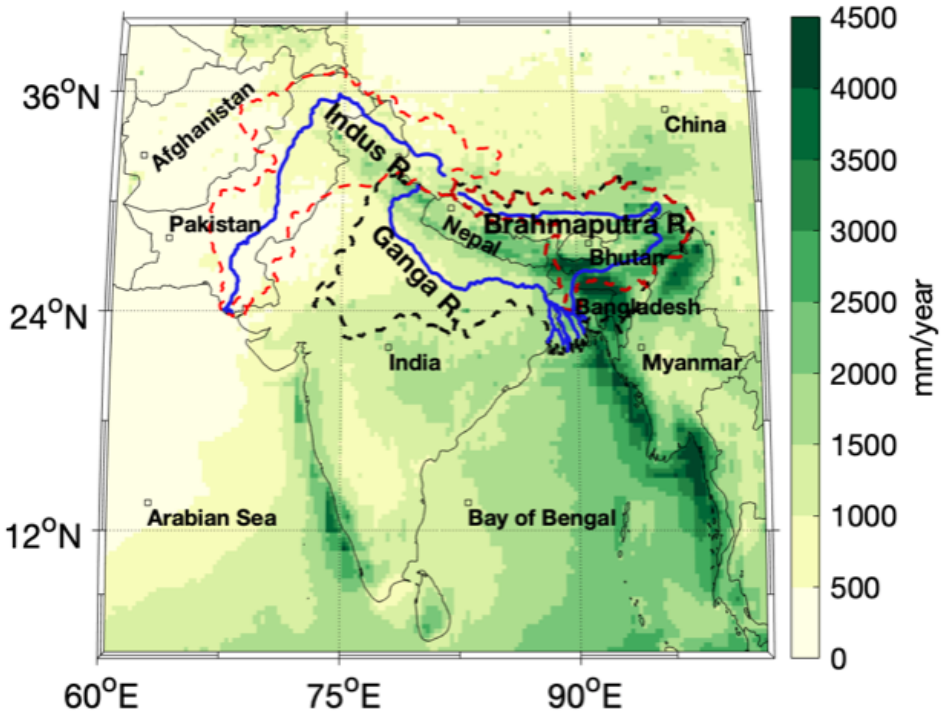

Figure 0.1 Mean annual precipitation averaged between 2001 and 2015 as estimated by the TRMM dataset (mm/year) over South Asia and the Indus River and Brahmaputra River watersheds (in red). The larger Ganga-Brahmaputra-Meghna watershed is demarcated as black dashed lines. TRMM – Tropical Rainfall Monitoring Mission [*Huffman et al.*, 2007]

The underlying climate regime also shifts in moving east from the Indus to the Brahmaputra watersheds from being winter precipitation dominated to summer monsoon precipitation dominated [*Greene and Robertson*, 2017; *Lutz et al.*, 2014]. This can be observed in the transition in the percentage of total annual precipitation received in the months of January-February-March (JFM) and June-July-August (JJA) for the two watersheds shown in Figure 0.2. The northwestern section of the Indus watershed that constitutes the Upper Indus Basin (UIB) (see Chapter 1) is located in the far western Himalaya and Karakoram Ranges. This region forms the principal headwater for the Indus and receives a majority of its precipitation as wintertime

precipitation (primarily as snowfall due to the high mean elevation of the region) [*Greene and Robertson*, 2017; *Kapnick et al.*, 2014]. The Brahmaputra watershed on the other hand receives almost all of its annual precipitation in the summer months from the South Asian Summer Monsoon (Figure 0.1b).

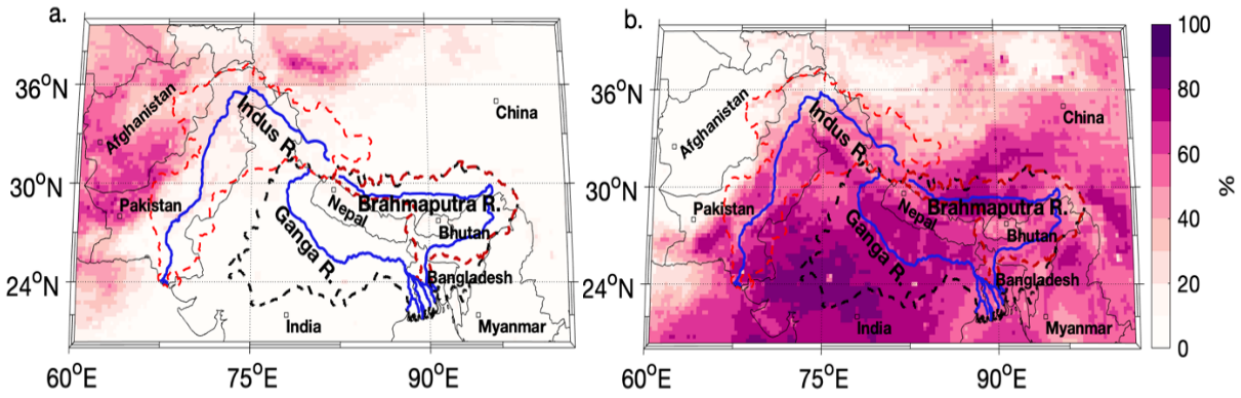

Figure 0.2 Percentage of annual precipitation received between (a.) January-March and (b.) June-August for the Indus and Brahmaputra River watersheds. Percentages are calculated between 2001 and 2015 from the TRMM data set. The Indus River watershed is located at a transition between the wintertime westerly dominated precipitation regime of West Asia and the South Asian Summer Monsoon (SASM) dominated precipitation in the Indian sub-continent. The Brahmaputra River watershed on the other hand receives almost all its annual precipitation during the summer.

In the first half of this dissertation we reconstruct streamflow discharge variability in the UIB (Chapter 1) and the Brahmaputra rivers (Chapter 2) respectively. In both chapters we also evaluate the climatic factors that contribute to streamflow variability in the watershed. As the gauged instrumental data available in the region is sparse, we developed our streamflow reconstructions using Hierarchical Bayesian Regression (HBR) [*Devineni et al.*, 2013]. In Chapter 1, we find that HBR with partial pooling [Devineni et al., 2013] provides a powerful framework to simultaneously reconstruct streamflow at multiple gauges within a watershed when discharge is correlated across the gauges being reconstructed. However, at one gauge that has a long enough instrumental record to allow for split calibration-validation of the tree-ring

reconstruction model we found that HBR compares well with Principal Components Regression (PCR) in terms of their estimates of past discharge, width of uncertainties, and reconstruction skill statistics. As PCR is much more commonly used in dendroclimatology is it reassuring that tree-ring reconstructions are not dependent on the choice of statistical method used. This also opens the avenue to harness the inherent hierarchy in streamflow discharge in a watershed (e.g. upstream to downstream gauges) to develop HBR based tree-ring reconstructions across a complex watershed network [e.g. *Ravindranath et al.*, 2019].

In the second half of the dissertation in Chapter 3 and Chapter 4, we examine the response of European and Mediterranean hydroclimate to tropical volcanism and describe a modified version of the statistical method of superposed epoch analysis (SEA) to identify consistent responses to randomly occurring events (e.g. volcanic eruption). The modified SEA method we implement in Chapters 3 and 4 helps better quantify multiple inherent uncertainties in the conventional application of SEA. These include, the out-sized leverage of one or more events (e.g. fire year, volcanic eruption) on the mean response, uncertainty in the timing of the events themselves, and the exact definition of what constitutes an event. In this dissertation we exclude one additional study that I lead during my PhD, *Rao et al.* [2015], where we evaluate how extreme winters and summer drought can contribute to mass mortality events of livestock in Mongolia (known as *dzud*).

Chapter 1: Six centuries of Upper Indus Basin streamflow variability and its climatic drivers

This chapter is published as *Rao et al.* [2018], Six Centuries of Upper Indus Basin Streamflow Variability and Its Climatic Drivers, *Water Resour. Res.*, *54*(8), 5687-5701.

Abstract

Our understanding of the full range of natural variability in streamflow, including how modern flow compares to the past, is poorly understood for the Upper Indus Basin (UIB) because of short instrumental gauge records. To help address this challenge, we use Hierarchical Bayesian Regression (HBR) with partial pooling to develop six centuries long (1394-2008 C.E.) streamflow reconstructions at three UIB gauges (Doyian, Gilgit, and Kachora), concurrently demonstrating that HBR can be used to reconstruct short records with interspersed missing data. At one gauge (Partab Bridge), with a longer instrumental record (47 years), we develop reconstructions using both Bayesian Regression (BR) and the more conventionally used Principal Components Regression (PCR). The reconstructions produced by PCR and BR at Partab Bridge are nearly identical and yield comparable reconstruction skill statistics, highlighting that the resulting tree-ring reconstruction of streamflow is not dependent on the choice of statistical method. Reconstructions at all four reconstructions indicate flow levels in the 1990s were higher than mean flow for the past six centuries. While streamflow appears most sensitive to accumulated winter (January-March) precipitation and summer (MJJAS) temperature, with warm summers contributing to high flow through increased melt of snow and glaciers, shifts in winter precipitation and summer temperatures cannot explain the anomalously high flow during the 1990s. Regardless, the sensitivity of streamflow to summer temperatures

suggests that projected warming may increase streamflow in coming decades, though long-term water risk will additionally depend on changes in snowfall and glacial mass balance.

1.1 Introduction

The Indus River and its tributaries provide the main source of water for Pakistan's vast irrigation network and hydropower generation for its power grid in an otherwise arid to semi-arid country. The river basin consists of seven main rivers, the Indus, Kabul, Jhelum and Chenab, known collectively as the western tributaries, and the Beas, Ravi and Sutlej known as the eastern tributaries [*Zawahri*, 2009]. Of these, the Indus is the most important as it contributes close to half of the overall discharge of the basin. The Indus River Basin is typically divided into two sections, the Upper Indus Basin (UIB) and Lower Indus Basin (LIB). The UIB refers to the section of the river above the Tarbela reservoir, an important source of water for Pakistan's irrigation network and hydropower potential [*Rashid et al.*, 2018] and located on the main Indus before its confluence with its other major tributaries [*Archer*, 2003]. The headwaters of the UIB originate in the upper reaches of the Karakoram and Himalaya ranges. Approximately three-fourths of UIB discharge is estimated to be a result of melting snow and ice, while summer rainfall plays a smaller role in contributing to the total discharge [*Immerzeel et al.*, 2009]. The interannual variability in UIB discharge is largely controlled by variability in the ablation of glacial mass balance and seasonal snowfall [*Forsythe et al.*, 2017]. Consequently, future changes in UIB flow will likely be regulated by changes in glacial mass balance and seasonal snowfall and the melt rate of both of these components. These melt rates are primarily controlled by changes in temperature and humidity [*Harpold and Brooks*, 2018; *Immerzeel et al.*, 2010]. Overall, for the Indus Basin (LIB and UIB) climate model projections of future runoff exhibit high uncertainty due to a large spread in precipitation (winter and summer) projections [*Ali et al.*,

2015; *Immerzeel et al.*, 2013; *Lutz et al.*, 2016]. However, there is a broad consensus that as glaciers recede, annual glacial runoff volume will likely increase until a maximum point known as 'peak water', beyond which runoff will decrease due to the reduced glacial area becoming unable to sustain the same runoff [*Huss and Hock*, 2018; *Lutz et al.*, 2014]. Future water management strategies (e.g., at the Tarbela reservoir) will therefore naturally depend on expected changes in UIB discharge [*Tahir et al.*, 2011].

Conflicting interpretations of recent climate and glacier trends have been observed over the high ranges of the Karakoram Mountains. While glaciers have declined over much of the Himalayas, glaciers in the Karakoram have either remained stable, or even expanded in certain cases [*Bolch et al.*, 2012; *Brun et al.*, 2017; *Gardelle et al.*, 2012; *Kapnick et al.*, 2014; *Minora et al.*, 2013]. This anomalous behavior of glaciers has been referred to as the 'Karakoram Anomaly' [*Hewitt*, 2005]. Two-thirds of high-altitude snow over the Karakoram accumulates in the winter, and is caused by synoptic westerly disturbances, while the remainder is attributed to monsoonal influences [*Benn and Owen*, 1998; *Greene and Robertson*, 2017; *Palazzi et al.*, 2014]. While the underlying causes of the Karakoram Anomaly remain unclear, it has been attributed to increases in summertime cloudiness [*Bashir et al.*, 2017; *Hewitt*, 2005; *Zafar et al.*, 2015], decreasing summertime temperature [*Fowler and Archer*, 2006], increases in wintertime snowfall [*Farhan et al.*, 2014; *Kapnick et al.*, 2014; *Ridley et al.*, 2013; *Tahir et al.*, 2011], high debris loading on the glaciers which insulates the underlying glaciers [*Kraaijenbrink et al.*, 2017; *Minora et al.*, 2013], land-surface feedbacks due to intensified lowland irrigation [*de Kok et al.*, 2018], and a southward shifted summertime westerly jet [*Forsythe et al.*, 2017].

Our understanding of recent streamflow trends, if any, is to a large extent limited by the short instrumental streamflow discharge records in the region that extend back two to four

decades at the longest. Having such short instrumental records encumbers our understanding of the full range of natural variability, especially at decadal to centennial timescales, and cannot provide a sufficient long-term context to assess possible recent changes in discharge. Predictions of future water risk may also be improved by a better understanding of the current and past variability and climatic controls of discharge [*Archer et al.*, 2010; *Forsythe et al.*, 2017; *Lutz et al.*, 2014].

To help address these multiple challenges, we present three new and one updated (cf. Cook et al., 2013b) reconstruction of UIB discharge at four discharge gauging stations (Partab Bridge, Doyian, Gilgit, and Kachora) for the past six centuries. These paleohydrologic reconstructions are developed using annually resolved climatically sensitive tree-ring chronologies in the UIB (Figure 1.1). These longer-term estimates of past flow can be used to better assess recent trends in UIB streamflow. Due to the constraints of sparse instrumental discharge data at the three shorter gauges records (Doyian, Gilgit, and Kachora) we develop reconstructions using Hierarchical Bayesian Regression (HBR) with partial pooling [*Devineni et al.*, 2013]. At one gauge with a long instrumental record (Partab Bridge) we test two reconstruction methods, Bayesian Regression (BR) and Principal Components Regression (PCR) (see Methods). The motivation behind developing a reconstruction using both PCR and BR at the same target gauge (Partab Bridge) from the same tree-ring predictor network is to test the hypothesis that streamflow reconstructions and their uncertainties should be highly comparable notwithstanding of the choice of statistical methodology used. The objectives of this are twofold. First, this provides a useful foundation upon which to base the choice of statistical methodology (i.e. PCR vs BR) for future reconstructions of streamflow or climate. Second, it allows us to compare the newly developed HBR reconstructions of streamflow at the three streamflow gauge

records (Doyian, Gilgit, and Kachora) against the reconstruction developed at Partab Bridge (cf. Cook et al., 2013b). We then investigate the potential climate drivers of streamflow at the four gauges for which we develop reconstructions of past discharge, along with the climate drivers of annual growth for the suite of tree-ring predictors used in our reconstruction model. We hypothesize that if the trees show a similar growth response to climate as the streamflow response to climate, that provides additional evidence that the paleo-discharge estimates presented here were caused by the same climatic forcing. Finally, the climate analyses allow us to specifically test how climate may have contributed to the high discharge rates in the 1990s and declining flows in the early 2000s [*Cook et al.*, 2013b; *Forsythe et al.*, 2017; *Hasson et al.*, 2017]. Taken together, we believe that the four long-term reconstructions of past discharge, along with the streamflow-climate and tree-growth-climate response analysis, provides a useful framework and context to better predict UIB hydrological regime changes.

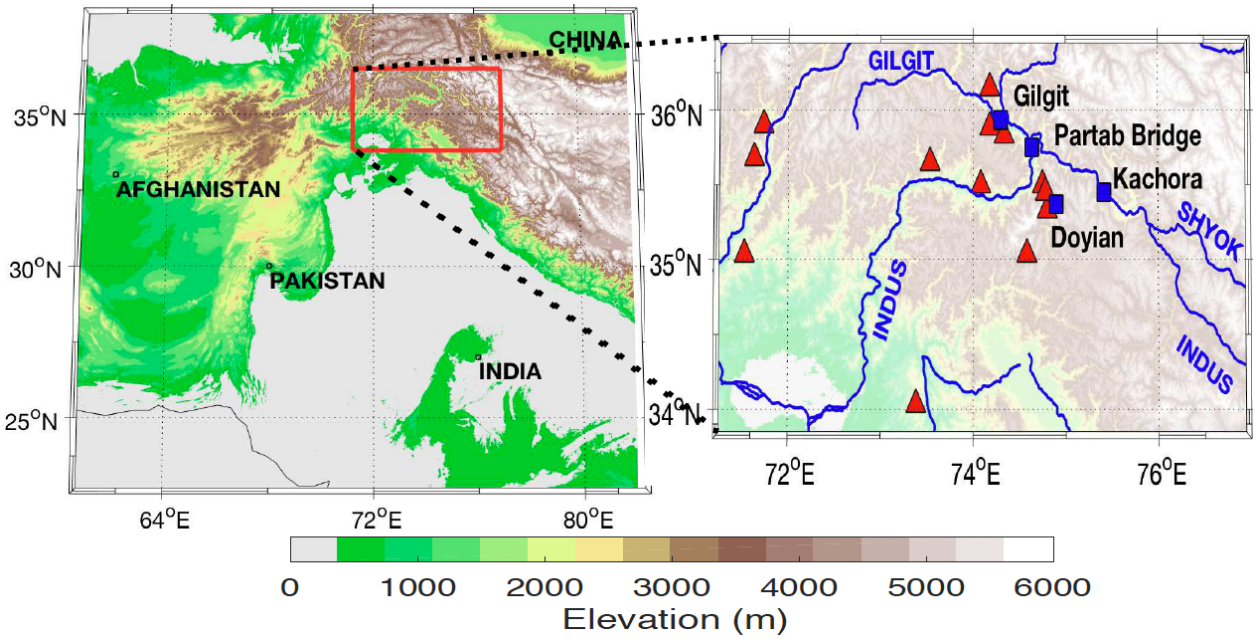

Figure 1.1 Map showing locations of streamflow gauges (blue squares) and tree-ring sites (red triangles) used in this study. The red box in the figure on the left highlights the region for which a close up is shown on the right.

1.2 Data

1.2.1 Instrumental streamflow and climate data

Instrumental streamflow data were obtained from the Pakistan Water and Power Development Authority (WAPDA) at the four target gauges, Partab Bridge, Doyian, Gilgit, and Kachora (Figure 1.1). Mean annual (January-December) discharge at each of these gauges is shown in Figure 1.2, and Table 1.1 describes some additional characteristics of the data (e.g. sub-basin names, mean, standard deviation etc.). The instrumental record for Partab Bridge was updated to 2008 (dashed line Figure 1.2) using estimates from three other gauges (Daiynor, Gilgit and Kachora) as described in Cook et al. (2013). The data quality in the early part of the Gilgit record between 1960 to 1972 exhibits greatly reduced inter-annual variability compared to the later part of the record. Consequently, we assume this to be a data quality issue and disregard the early period of the Gilgit data in subsequent analysis. Discharge at the gauges peaks between May through September as seen in the monthly discharge hydrograph (Figure 1.3). We obtained temperature and precipitation data from the global gridded 0.5° resolution CRU TS.v.4.01 dataset that covers the period 1901-2016. A box plot of monthly climate (temperature and precipitation) averaged across a 2° latitude x 2° longitude grid (73.5°E-75.5°E and 34.5°N-36.5°E) between 1961-2016 is also shown in Figure 1.3. These 2°x2° regionally averaged temperature and precipitation series are used in the climate analyses with streamflow and tree growth.

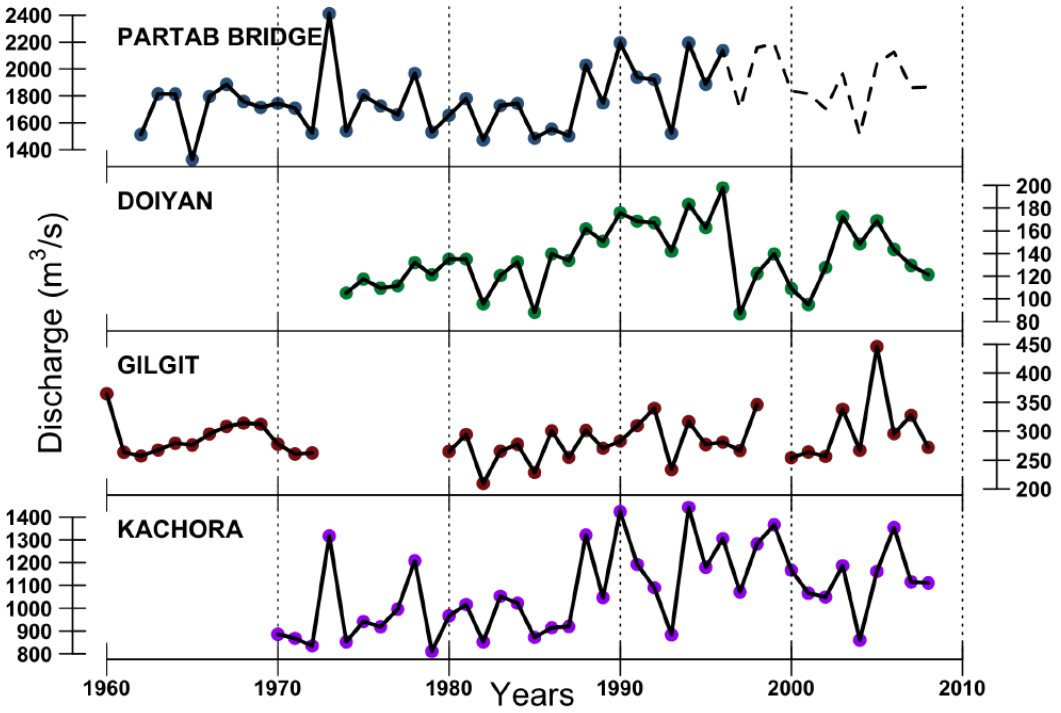

Figure 1.2 Instrumental period mean annual discharge (m^3/s) at four streamflow gauges in the Upper Indus Basin (UIB) watershed (solid black). The Partab Bridge record between 1997-2008 (dashed line) is estimated by using three proximal streamflow gauges (Cook et al. 2013).

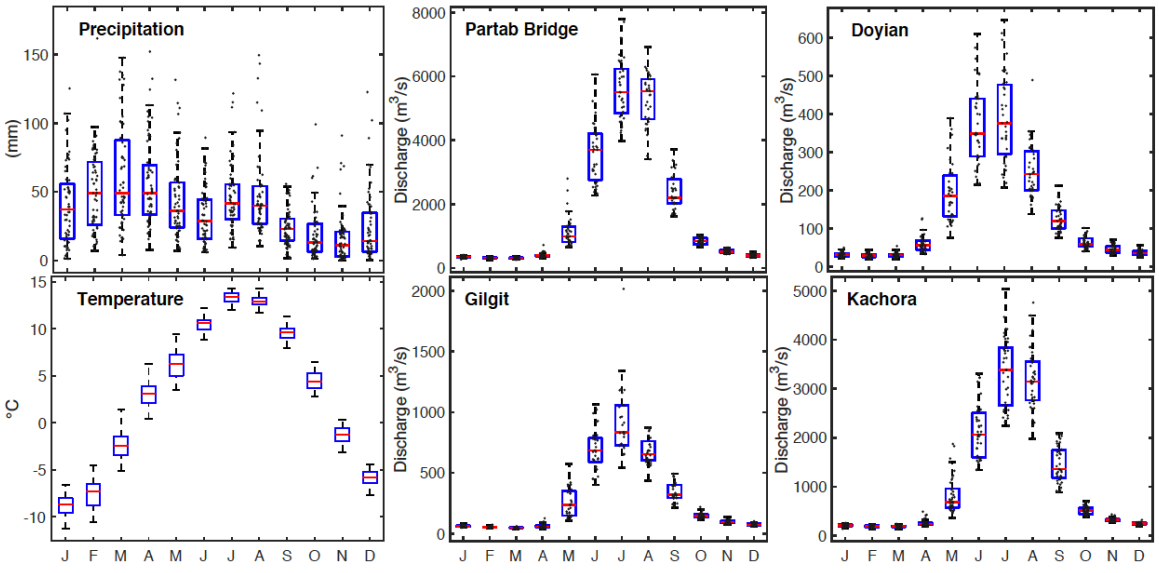

Figure 1.3 Boxplots showing month-by-month variability in precipitation (mm) and temperature (°C) between 1961-2016, and monthly discharge hydrographs (m^3/s) for the instrumental period at four streamflow gauges in the UIB. Note different y-axis ranges. X-axis labels represent months of the year.

1.2.2 Tree-ring network

The annual growth of trees is often controlled on interannual and decadal timescales by the same climatic factors that control streamflow in rivers [*Meko et al.*, 1995]. These may include winter snowpack and summer temperatures [e.g. *Woodhouse and Lukas*, 2006], summer drought [e.g. *Cook and Jacoby*, 1983; *Devineni et al.*, 2013], and monsoonal precipitation [e.g. *D'Arrigo et al.*, 2011]. This underlying principle has allowed for the use of tree-rings to develop reconstructions of past flow and flow extremes, including for one gauge on the UIB (Cook et al., 2013b). These paleohydrologic records from tree rings have found a wide variety of applications, from placing instrumental mean discharge in a long-term context [*Stockton and Jacoby*, 1976], to being used as forecasting, planning and research tools by water managers [*Meko and Woodhouse*, 2011], and understanding continental scale streamflow co-variability and clustering [*Ho et al.*, 2017].

For our study, as an initial screening for useful tree-ring predictors to develop our streamflow reconstruction models we downloaded all tree-ring series located within the broad Karakoram and Western Himalaya region with an end year later than 2005 from the International Tree-Ring Data Bank (ITRDB) (https://www.ncdc.noaa.gov/data-access/paleoclimatology-data/datasets/tree-ring). The raw annual ring-width data for each site were 'standardized' [*Cook and Kairiukstis*, 1990; *Fritts*, 1976] using the 'signal-free' (SF) method [*Melvin and Briffa*, 2008]. The SF method aims to maximize the preservation of common medium frequency variance in tree-ring series and eliminate trend distortion effects with attention paid to preserving multi-decadal to centennial variability due to climate. A series was retained as a predictor in a model if it correlated at $p<0.05$ using a two-sided t-test with the streamflow gauge record. Tree-ring series were also tested as potential predictors with a lag of one year (lag t+1) with respect to

the streamflow data, as often prior year climate can influence current year tree-growth [*Fritts*, 1976]. In our analyses, we develop two sets of models. The first is a reconstruction of May through September (MJJAS) flow at Partab Bridge using two reconstruction methods, PCR and BR (Model I). The second is an HBR reconstruction of annual (January-December) flow at Doyian, Gilgit, and Kachora (Model II). The choice of the MJJAS season at the target for the reconstruction at Partab Bridge is that it coincides with the peak flow season (cf. Cook et al., 2013b). For the HBR reconstructions of flow at Doyian, Gilgit, and Kachora, we first attempted to develop MJJAS season streamflow reconstructions as well, followed by a northern hemisphere water-year (October-September) reconstruction. However, these two models performed poorly compared to a model reconstructing mean annual (January-December) discharge based on their calibration-validation statistics (see Methods Section). Based on our predictor screening criteria we use 15 tree-ring series as predictors for the reconstruction model at Partab Bridge, and 10 series as predictors for the HBR reconstruction model at the other 3 gauges. The final set of predictor tree-ring series used in Models I and II are shown in Table A.1 and plotted in Figure A.1 [*Bunn*, 2010]. The original source for these collections are *Ahmed et al.* [2011], *Ahmed et al.* [2013], and *Zafar et al.* [2010].

Table 1.1 Streamflow gauge network in the Upper Indus Basin. *We only use the 1980-2008 section of the Gilgit gauge record for ensuing analysis

Gauge	River (sub-basin)	Lat.	Lon.	Elev. (m)	Start	End	Missing data	Annual Mean (m^3/s)	St. Dev. (m^3/s)	Skewness
Partab Bridge	Indus	35.78	74.63	1419	1962	1996	-	1763.43	237.34	0.66
Doyian	Astore	35.33	76.42	1195	1974	2008	-	135.79	27.79	0.21
Gilgit	Gilgit	35.11	74.06	1140	1960 *1980	2008	1973-1979, Jul-Dec 1999	286.99	45.50	1.44
Kachora	Indus	35.27	75.25	1460	1970	2008	-	1074.85	181.79	0.38

1.3 Methods

1.3.1 Reconstruction model

A commonly used method to reconstruct a predictand (or dependent) variable such as streamflow or climate from tree rings is principal components regression (PCR) [*Cook et al.*, 1999b; *Cook et al.*, 2010a; *Cook et al.*, 2013b; *Harley and Maxwell*, 2017; *Harley et al.*, 2017]. However, PCR cannot be easily used to reconstruct streamflow at gauges that have extremely short records and data gaps, without an imputation step for the missing data. For the UIB specifically, while the length of each available gauge record is relatively short (Figure 1.2), we are fortunate to have a network of gauging stations that are in close proximity to each other and located on different tributaries in the same watershed (Figure 1.1; Table 1.1). An alternative streamflow reconstruction method to PCR is Hierarchical Bayesian Regression (HBR) with partial pooling [e.g. *Devineni et al.*, 2013]. HBR with partial pooling allows regression coefficients to be correlated across the gauges being reconstructed by modelling the vector of regression coefficients as draws from a common multivariate normal distribution. The physical basis of this assumption is that streamflow discharge tends to be correlated at the scale of a watershed [Figure A.2 and *Ho et al.*, 2017; *Sobkowiak et al.*, 2020]. This partial pooling framework allows us to shrink the number of free parameters to be estimated and reconstruct streamflow at gauges with short instrumental records. This can result in lower uncertainty in estimated parameters and reconstructed discharge, along with improving the skill of the final model by combining the regression strength of the model across gauges [*Devineni et al.*, 2013]. Finally, HBR estimates predicted values by drawing from prior distributions and can therefore handle data gaps in a very natural way.

For the UIB, *Cook et al.* [2013b] used PCR to reconstruct May through September (MJJAS) peak season discharge at Partab Bridge between 1452-2008 C.E. Partab Bridge was chosen as the target gauge for reconstruction by Cook et al. (2013) because it has the longest continuous available record of flow and also includes discharge from both the east and west regions of the UIB (Figure 1.1). We develop PCR and BR models at Partab Bridge to produce a slightly longer reconstruction (cf. Cook et al. 2013) between 1430-2008 C.E. (originally 1452-2008 C.E.). The original Cook et al. 2013 PCR reconstruction at Partab Bridge and the one developed here are nearly identical over the period of overlap between 1452-2008 C.E. In all reconstructions we used a multiple linear regression framework where we estimated streamflow (the predictand variable) using a vector of predictor variables. The vector of predictor variables used are the principal component (PC) scores [*Cooley and Lohnes*, 1971] of the suite of normalized tree-ring-width indices (RWI). The RWI were normalized using their respective calibration period means and standard deviations and the PCs were computed from the RWI suite to be orthogonal during the calibration period (Cook et al., 1999). In each model, only leading PCs with eigenvalues greater than 1 were retained as potential predictors for streamflow as an estimate of common shared 'signal' (versus noise) across the different tree-ring series using the Kaiser-Guttman criteria [*Guttman*, 1954; *Kaiser*, 1960]. We used a 'nested' approach in both models I and II, where shorter tree-ring predictor series were dropped sequentially until the predictor suite was exhausted and reconstructions were made for each nest [e.g. *Meko*, 1997]. To develop the final nested reconstruction, we appended each longer nest to the start year of the shorter nest after scaling its variance to that of the calibration period instrumental data.

For the reconstruction at Partab Bridge using PCR and BR (Model I) we used a 30-year period between 1975-2004 as a model calibration period, and the early part of the data between

1962-1974 (13 years) as the model validation period. This is the same calibration and validation period used in Cook et al. (2013). For the HBR models at Doyian, Gilgit, and Kachora (Model II) we used a 1970-2004 calibration period with a leave-one-out cross-validation (LOOCV) approach to compute model validation statistics. LOOCV was used for the HBR model as the individual instrumental time series were too short to divide into separate calibration and validation periods. After accounting for the varying start years of the gauge records (Table 1.1) the length of the calibration periods for Model II were as follows: Doyian (n=29), Gilgit (n=23), and Kachora (n=33). The longer Partab Bridge record was not included in the HBR reconstruction (Model II) to maintain the independence between the predictand variables (i.e. the streamflow gauge) being reconstructed, as the Partab Bridge record between 1997-2008 was estimated by Cook et al. 2013 using the Gilgit and Kachora records. We used the Shapiro-Wilk normality test [*Shapiro and Wilk*, 1965] to test the null hypothesis that the streamflow data come from normal distributions. For instrumental MJJAS flow at Partab Bridge, and annual flows at Doyian and Kachora we accepted this null hypothesis of normality, while at Gilgit we rejected the null hypothesis that annual flow is normally distributed at $p<0.05$. However, after examining the kernel density plot (not shown) and time series plot of mean annual streamflow at Gilgit (Figure 1.2), we found that if the high flow anomaly in 2005 is excluded, the skewness decreases from 1.44 to 0.14, and we would have accepted the null hypothesis of streamflow being normally distributed at Gilgit. When testing for normality during the calibration period (1975-2004 – Partab Bridge; 1970-2004 – Doyian, Gilgit, and Kachora) at all three gauges we accepted the null hypothesis of normality. Therefore, we chose to not transform (e.g. log or power transform) the original data at Gilgit in our streamflow reconstruction. This was also done to retain the same units across the three gauges being reconstructed using HBR. Prior to developing the PCR, BR,

HBR models, the streamflow data were also normalized by subtracting their respective calibration period means and dividing by their respective calibration period standard deviations. The final reconstructions were then scaled to the calibration period mean and variance.

We tested model calibration and validation fidelity by computing the following statistics, i.) CRSQ (calibration period coefficient of multiple determination or R^2), ii.) CVRE (calibration period reduction of error calculated by leave-one-out cross-validation), iii.) VRSQ (validation period square of the Pearson correlation or r^2), iv.) VRE (validation period reduction of error) and v.) VCE (validation period coefficient of efficiency) [see supplementary material in *Cook et al.*, 2010a]. The VCE is equivalent to the Nash-Sutcliffe Efficiency test [*Nash and Sutcliffe*, 1970]. For the HBR model, we only present CRSQ, CVRE, and RE (reduction of error) statistics as the model does not have a formal validation period due to the shortness of the gauge records. The formulation used for calculating RE for the HBR model is as follows

$$RE = 1 - \frac{SSE_V}{SSE_{null}}$$

where SSE_v is the sum-of-squares of cross-validation errors and SSE_{null} is the sum-of-squares of differences is the calibration mean is used as the prediction for each year [*Meko*, 2006]. In general, models with VRE, VCE, and RE values greater than 0 are considered an indication that the model has skill compared to using the calibration period, validation period, and calibration period means respectively as the estimate for each year. We also compared model performance using median-normalized root mean square error (RMSE) [*Janssen and Heuberger*, 1995] statistic calculated as

$$RMSE = \sqrt{\frac{1}{n}\sum_{t=1:n}(y_t - \hat{y_t})^2}$$

$$median - normalized\ RMSE = 100 * \frac{RMSE}{median(y_t)}$$

where y_t and $\widehat{y_t}$ are the observed and predicted discharge in year t respectively. The median-normalized RMSE can be thought to represent how large the model error is as a percentage of the median discharge, with larger values representing larger error.

1.3.1.1 Principal Components Regression

Principal Components Regression (PCR) is used here to reconstruct streamflow discharge from tree-rings and is the same method used to reconstruct UIB discharge at Partab Bridge by Cook et al. (2013). Following that work, we also estimated model uncertainties in PCR by applying maximum entropy bootstrapping (n=300) [MEBoot - *Vinod*, 2006; *Vinod and López-de-Lacalle*, 2009] to both the tree-ring and streamflow data. MEBoot can be thought of here as a random perturbation method that is applied to both the predictor and predictand series. In so doing, MEBoot preserves the overall stochastic properties of the original time series used in regression line the chronological order of the data being resampled, but changes in a random fashion the principal components derived from the PCR procedure, along with the streamflow data. As such, the MEBoot procedure also produces an empirical probability distribution functions (pdfs) for each reconstructed year that contributes to the uncertainty estimates on the reconstructions (Cook et al., 2013b).

1.3.1.2 Bayesian Regression

1.3.1.2.1 Hierarchical Bayesian Regression with partial pooling

$$y_{i,t}|\alpha_i, \boldsymbol{\beta_i} = \alpha_i + \boldsymbol{\beta}_i * \boldsymbol{X}_t + \varepsilon_{i,t} \text{ (i=1,2,3)}$$

$$\boldsymbol{\beta_i} \sim \text{MVN}(\mu_B, \sum_{\boldsymbol{B}})$$

Priors modelled as:

$$\alpha_i \sim \mathrm{N}(0, 10^4)$$

$$\varepsilon_{i,t} \sim \mathrm{N}(0, 10^4)$$

$$\boldsymbol{\mu_B} \sim \mathrm{MV}N(0, 10^4 \boldsymbol{I})$$

$$\sum_{\boldsymbol{B}} \sim Inv - Wishart_{v0}\,(\boldsymbol{\Lambda_0})$$

HBR reconstructions with partial pooling were developed at each gauge using a multiple linear regression of streamflow ($\mathbf{y_{i,t}}$) at gauge i at year t on a vector of predictors (X_t). The matrix **X** contains the PC score time series of tree-ring predictors used in the current nest. β_i is a vector of the corresponding regression slopes for each predictor in the vector X_t at gauge i. Each regression includes at intercept term α_i and a prediction error term $\varepsilon_{i,t}$. We modeled priors to be vague or non-informative [*Gelman and Hill*, 2006], and the covariance structure of regression coefficients β_i for each streamflow gauge to be derived from a multivariate normal distributions (MVN). This assumption is based on the consideration that annual flows are correlated across gauges (Figure A.2). Parameter β_i is in turn described by two hyperparameters μ_B and a dispersion matrix $\sum_{\mathbf{B}}$ leading to the hierarchical framework in our model [*Gelman and Hill*, 2006]. We assumed the prior for covariance matrices $\sum_{\mathbf{B}}$ to be an inverse-Wishart distribution with scale matrix Λ_0, specified to be an identity matrix I with v_0 degrees of freedom [*Devineni et al.*, 2013]. v_0 is set to be one more than the dimension of the matrix or the total number of predictors used in the nest.

We hypothesise that by modelling the covariance structure of regression coefficients we are able to borrow the strength of the regression estimates at one streamflow gauge and use that for predictions at another gauge [*Devineni et al.*, 2013]. This permits us to derive a better regression estimates during the model calibration period, and consequently make a better

prediction of past streamflow. Unlike in *Devineni et al.* [2013], here we modeled the associated prediction error terms, or residuals, $\boldsymbol{\varepsilon_{i,t}}$ be derived from a normal distribution and not a MVN. This is because each streamflow gauge discharge series spans a different range of years (Figure 1.2). Consequently, it was not possible to compute the spatial covariance of the error term. Also, our matrix **X** uses PC scores and not the standardized tree-ring series directly [c.f. *Devineni et al.*, 2013]. This predictand 'data-reduction' was necessary due to shortness of the gauge records, to reduce the number of 'free-parameters' to be estimated relative to the number of years of streamflow data available for model calibration.

The final joint posterior distribution $\mathbf{P(\theta/y)}$ for the partial pooling case, with regression intercepts α_i slopes β_i, error $\boldsymbol{\varepsilon_{i,t}}$, and covariance $\sum_{\mathbf{B}}$ is described as follows.

$$\boldsymbol{P(\theta/y)} \propto \prod_{i=1}^{3}\prod_{t=1}^{n_t} \begin{matrix} [N(y_i(t)|\alpha_i + \boldsymbol{\beta_i}\, \boldsymbol{X(t)}, \varepsilon_i(t))] * N(\alpha_i|0, 10^4) \\ MVN(\boldsymbol{\beta_i}|\mu_B, \sum_{\boldsymbol{B}}) * InvWish(\sum_{\boldsymbol{B}}|V_0, \Lambda_0) \\ MVN(\mu_B|0, 10^4 I) * N(\varepsilon_i(t)|0, 10^4) \end{matrix}$$

For each model we estimated the parameters θ and the posterior distributions P(θ/y) by employing a Gibbs sampler, a Markov Chain Monte Carlo (MCMC) method using the software Just Another Gibbs Sampler [JAGS - *Plummer*, 2003]. We simulated three chains, where the parameters were assigned random starting values. This was done to test whether starting values affect convergence towards the final parameter estimates. The chains were run for a 1,000-cycle burn-in following which we ran 10,000 simulations. We determined the chains to have converged by visually analyzing the trace plots for the parameters, and checking whether the Gelman-Rubin diagnostic shrink factors were less than 1.1 [*Gelman and Rubin*, 1992]. To validate the fit of our model we computed the Bayesian p values for the mean, and sum of squared errors (SSQ). The Bayesian p value for the mean and SSQ were calculated as the proportion of times the mean and SSQ of the model simulated calibration and validation data

was greater than that of the actual streamflow data. A Bayesian p value of close to 0.50 indicates good model fit. The final reconstructions and our JAGS code are available in Data Set S1 and S2 respectively (in the online version of the published paper).

1.3.1.2.2 Bayesian Regression

While the relatively more complex HBR model was used to reconstruct multiple gauges simultaneously (Doyian, Gilgit, and Kachora), we developed a simplified BR to reconstruct streamflow at Partab Bridge for comparison with the PCR reconstruction. Unlike the HBR model, the BR model has no hierarchy, as only one gauge is being reconstructed. In this model, we assumed the regression slopes β_i to be derived from a normal distribution. Two sets of BR models were used to develop flow estimates at Partab Bridge. The first is a model which uses tree-ring predictors, and the resulting reconstruction from it was then used for comparison with the streamflow reconstruction developed using PCR. In the second model, we use our analysis of the climatic controls of streamflow at Partab Bridge to develop an estimate of streamflow between 2009 through 2016 using a climate-variable driven BR model.

1.4 Results

1.4.1 Streamflow reconstructions

The MJJAS seasonal reconstruction of streamflow at Partab Bridge (Figure 1.4) and the three HBR reconstructions of mean annual streamflow at Doyian, Gilgit, and Kachora (Figure 1.5) all indicate that the period of decadal high flow between 1991-2000 is unusual in the long-term context of the past six centuries. The only comparable period of high flow in the reconstructions occurs during the 1470s. In all reconstructions, the 20-year low-pass filtered discharge exceeds the 90th percentile of reconstructed discharge over the past six centuries (but

remains within reconstruction uncertainties) indicated by the dashed blue horizontal lines. Following this peak in the 1990s, both the instrumental data and reconstructions suggest a decrease in discharge post-2000. Periods of anomalous low flow are indicated in the MJJAS seasonal reconstruction at Partab Bridge in the early 1600s, 1890s, and the 1970s, and in the three-gauge HBR annual reconstruction during the 1650s, and 1820s.

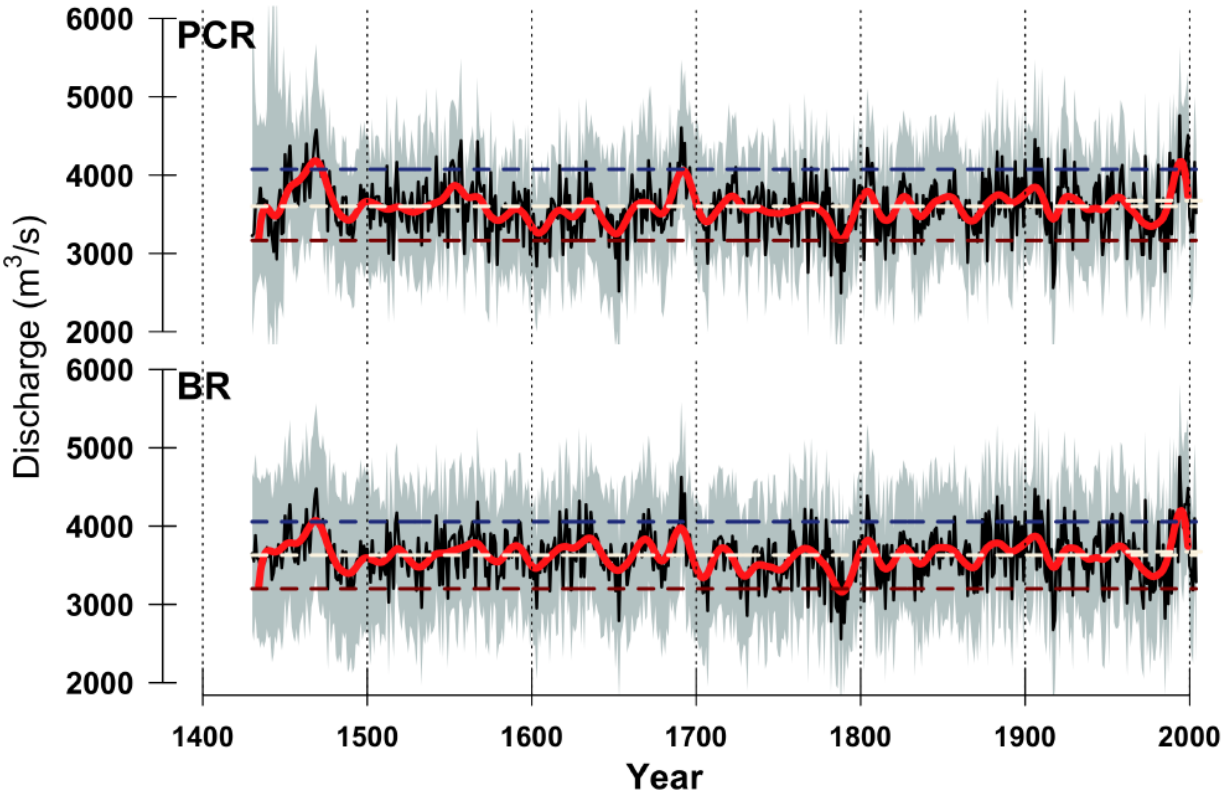

Figure 1.4 Reconstructed mean May through September (MJJAS) discharge (m^3/s) at Partab Bridge 1430-2008 C.E. (solid black) using Principal Components Regression (PCR) and Bayesian Regression (BR) along with 20-year low pass filtered reconstruction (solid red). Horizontal dashed red and blue lines are 5th and 95th percentiles of the reconstructions. The horizontal white line between 1400-2008 C.E. represents the mean of the full reconstruction, and that between 1962-2008 C.E. is the mean of the instrumental period.

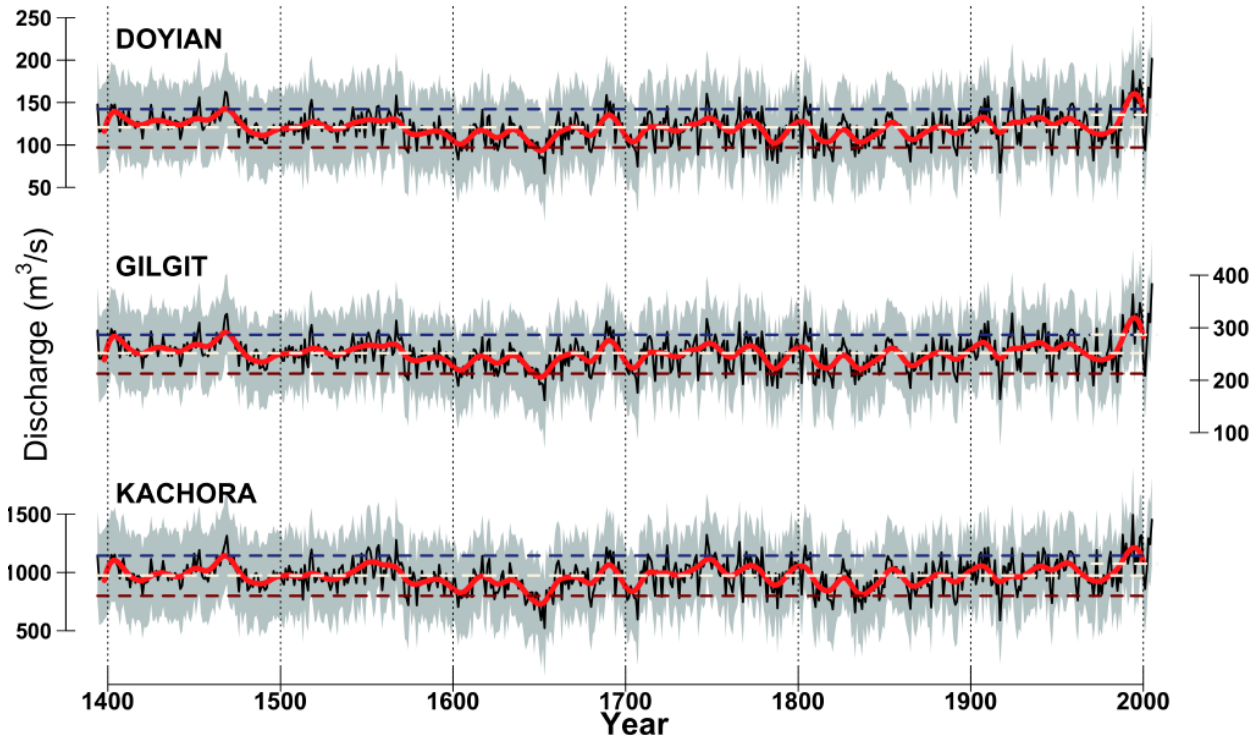

Figure 1.5 Same as Figure 1.4 but showing reconstructed mean annual (January-December) flow (m^3/s) at Doyian, Gilgit, and Kachora between 1394-2008 C.E. using Hierarchical Bayesian Regression (HBR) with partial pooling.

We produced a MJJAS seasonal streamflow reconstruction at the updated Partab Bridge record using PCR and BR (Figure 1.4). The final reconstruction produced by both methods (PCR and BR) are virtually identical, with minor differences in the widths of their uncertainties (Figure A.3). The reconstructions are highly correlated over the 575 years of reconstructed discharge (Pearson's r=0.91). Importantly, the calibration-validation statistics of the two reconstructions, as calculated using the CRSQ, VRSQ, CVRE, VRE, and VCE metrics are comparable for the entire length of the reconstruction between 1430-2004 C.E. (Figure A.4). The median value of these statistics for the full reconstructions are, **i.** CRSQ: PCR - 49.80%, BR - 56.04%; **ii.** VRSQ: PCR - 54.70%, BR - 53.79%; **iii.** CVRE: PCR - 42.50%, BR - 43.68%; **iv.** VRE: PCR - 0.52, BR - 0.54; and **v.** VCE: PCR - 0.50, BR - 0.52. The HBR model annual discharge estimates during the instrumental period are shown in Figure A.5, and the calibration-validation statistics computed

by LOOCV are shown in Figure A.6. The consistently positive VRE and VCE values for each nest in PCR and BR reconstruction at Partab Bridge (Figure A.4) and RE values for the HBR reconstructions at Doyian, Gilgit, and Kachora (Figure A.6) indicates the reconstructions are skillful. Bayesian p values for predictions of the mean, and mean squared errors were consistently close to or equal to 0.50 for all nests for the BR and HBR models.

1.4.2 Climate controls on discharge

We then used the updated Partab Bridge (1962-2008 C.E.) record, the longest of our four records (n=47), to evaluate the relationship between climate and streamflow in the region. We first examined the relationship between monthly climate (precipitation and temperature) and mean MJJAS streamflow (Figure 1.6a) and tested for both contemporaneous and lagged relationships between climate and streamflow. All tests are based on the Pearson correlation and a 2-sided hypothesis test with each series computed as first-differences to minimize the effect of trends and auto-correlation in the data. We found MJJAS streamflow to be positively correlated with current year January through March precipitation ($\rho<0.01$), inversely correlated with prior year July ($\rho<0.05$), and positively correlated with current year June ($\rho<0.05$) and current year July ($\rho<0.01$) mean monthly temperature. When the same monthly climate versus discharge correlation analysis was carried out separately for each month of streamflow between May through September (not shown) we found that monthly discharge in a month was always significantly positively correlated with monthly temperature for that month ($\rho<0.01$). Based on these results, we infer the main climate seasons relevant for MJJAS streamflow at Partab Bridge to be January through March (JFM) precipitation likely in the form of snowfall, inferred from subfreezing temperatures in the region during this season (temperature boxplot Figure 1.3), along

with MJJAS mean temperature.

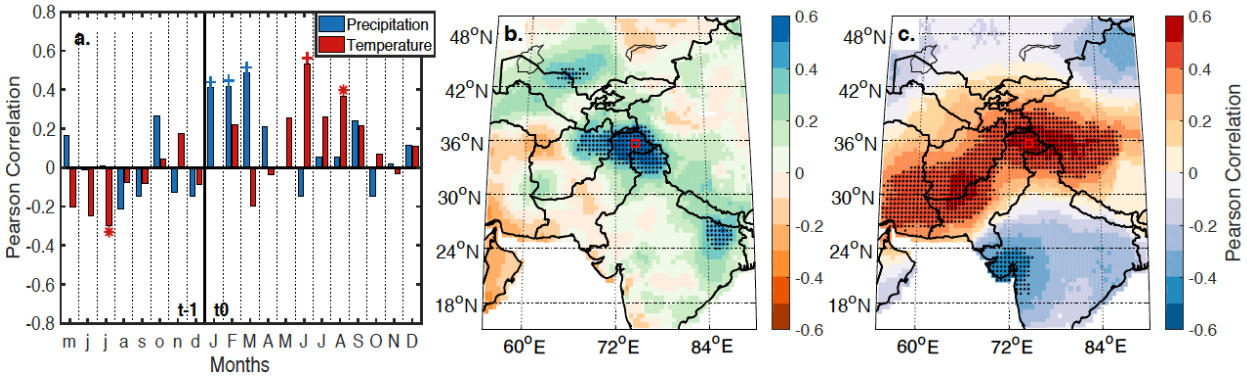

Figure 1.6 Pearson's correlations between MJJAS mean discharge at Partab Bridge (1962-2008) and a) month-by-month precipitation (blue) and temperature (red) ('*' - p<0.05, and '+' - p<0.01) for months between prior year (t-1) May through current year (t0) December, b.) January-March (JFM) mean precipitation (positive-green; negative-red), and c.) MJJAS mean temperature (positive - red, negative - blue). All time series were computed as first-differences. In b. and c. stippling indicates significance at p<0.01, while the red square is location of the gauge station.

Next, we computed spatial correlations between MJJAS discharge at Partab Bridge and JFM monthly mean precipitation and MJJAS monthly mean temperature to assess the spatial footprint of the climate to discharge relationship (Figure 1.6b and 1.6c). We found that MJJAS mean discharge at Partab Bridge is positively correlated (stippled blue shading for $\rho<0.01$) with JFM precipitation within the Karakoram region (Figure 1.6b), and positively correlated with temperature (stippled red shading for $\rho<0.01$) over a broad spatial region spanning the Karakoram, Hindu Kush, and Toba Kakar ranges (Figure 1.6c). To further understand if the climate controls on discharge at Partab Bridge vary through the MJJAS season, we also computed the month-by-month correlations of mean May-July (MJJ) discharge against temperature and precipitation (Figure A.7a), along with similar correlations for mean August-September (AS) discharge (Figure A.7b). For MJJ discharge we find significant positive correlations with JFM precipitation and MJJ temperature ($\rho<0.05$), while for AS discharge

significant positive correlations were found with January and March precipitation and August temperature ($\rho<0.01$).

We also performed a similar month-by-month correlation analysis between climate variables and mean MJJAS flow at Doyian (n=35) Gilgit (n=27), and Kachora (n=38) (Figure A.8). Discharge at all gauges shows a significant positive correlation with February precipitation ($\rho<0.01$). At Doyian there is broad significant positive correlation between discharge and February through May precipitation ($\rho<0.05$), but no significant correlation between discharge and temperature was observed (Figure A.8a). At Gilgit, discharge was found to be positively correlated with February and March precipitation ($\rho<0.05$), and negatively correlated with February temperature ($\rho<0.05$) (Figure A.8b). Finally, at Kachora discharge was significantly positively correlated with JFM precipitation ($\rho<0.01$), and with May, June, and August temperature (Figure A.8c). While the HBR reconstructions at Doyian, Gilgit, and Kachora presented in the previous section are for mean annual discharge, we found that the climate to streamflow relationship was nearly identical for mean annual discharge and mean MJJAS discharge shown in Figure A.8 (not shown).

The positive relationship between wintertime precipitation and summertime temperature at Partab Bridge and Kachora suggests that discharge at these gauges is influenced by both winter snow accumulation and summer snow and glacial melt. However, at Doyian and Gilgit that lack of temperature sensitivity suggests that discharge at these gauges depends primarily on wintertime snowfall and with temperature dependent glacial melt playing little to no contributing role. These findings are consistent with *Mukhopadhyay and Khan* [2014], who use the percentage of watershed within a hypsometric band (i.e. elevation zone) and determine that main Indus sub-basins where Kachora and Partab Bridge are located are more heavily glaciated and

have a higher mean elevation than the Astore and Gilgit sub-basins where the Doyian and Gilgit gauging stations are located (also see Table 1.1 for basin names).

1.4.3 Climate controls on tree-growth

We then examined the climate to tree-growth response of the predictor suite used in the first nest for the MJJAS reconstruction at Partab Bridge. In our reconstruction model, we retained the first four PC time series in the first nest, with the following percentage variance explained, PC1 - 50%, PC2 - 14%, PC3 - 9%, and PC4 - 7%. Cumulatively, these PCs explain 80% to the total variance of the predictor suite. The month-by-month climate to PC1 and PC2 correlations for the time period 1962-2008 are shown in Figure 1.7a and 1.7b, while those for PC3 and PC4 are shown in Figure A.7c and A.7d. We find that PC1 shows a broad January through May positive correlation with precipitation ($\rho<0.01$), while PC2 shows a significant inverse correlation with temperature that peaks in current year May through August ($\rho<0.01$). Both PC3 and PC4 show significant inverse correlations with June ($\rho<0.01$) and July ($\rho<0.05$) temperature. The PC loadings of each tree-ring series on the first four PC time series are shown in Figure 1.7c. All sites except MuaABP.t1 and NltPCS.t1 show strong positive loadings on PC1, as indicated by the shaded green circles. This together with Figure 1.7a, reveals that almost all tree-ring predictors used in our model respond positively to wintertime snowfall. While the PC2-PC4 time series all represent an inverse summer temperature sensitivity, the loadings of each tree-ring series were either positive (green shading) or negative (pink shading). A positive loading on PC2-PC4 indicates that a particular tree-ring series responds inversely to summer temperature, while a negative loading indicates that the tree-ring site responds positively to summer temperature [also see *Ahmed et al.*, 2011]. We also conducted a similar analysis with the first four PC time series with eigenvalues greater than one which were retained as predictors in

the first nest for the HBR reconstruction at Doyian, Gilgit, and Kachora. The PCs showed a nearly identical climate response as the first four PCs retained in the BR model at Partab Bridge (not shown).

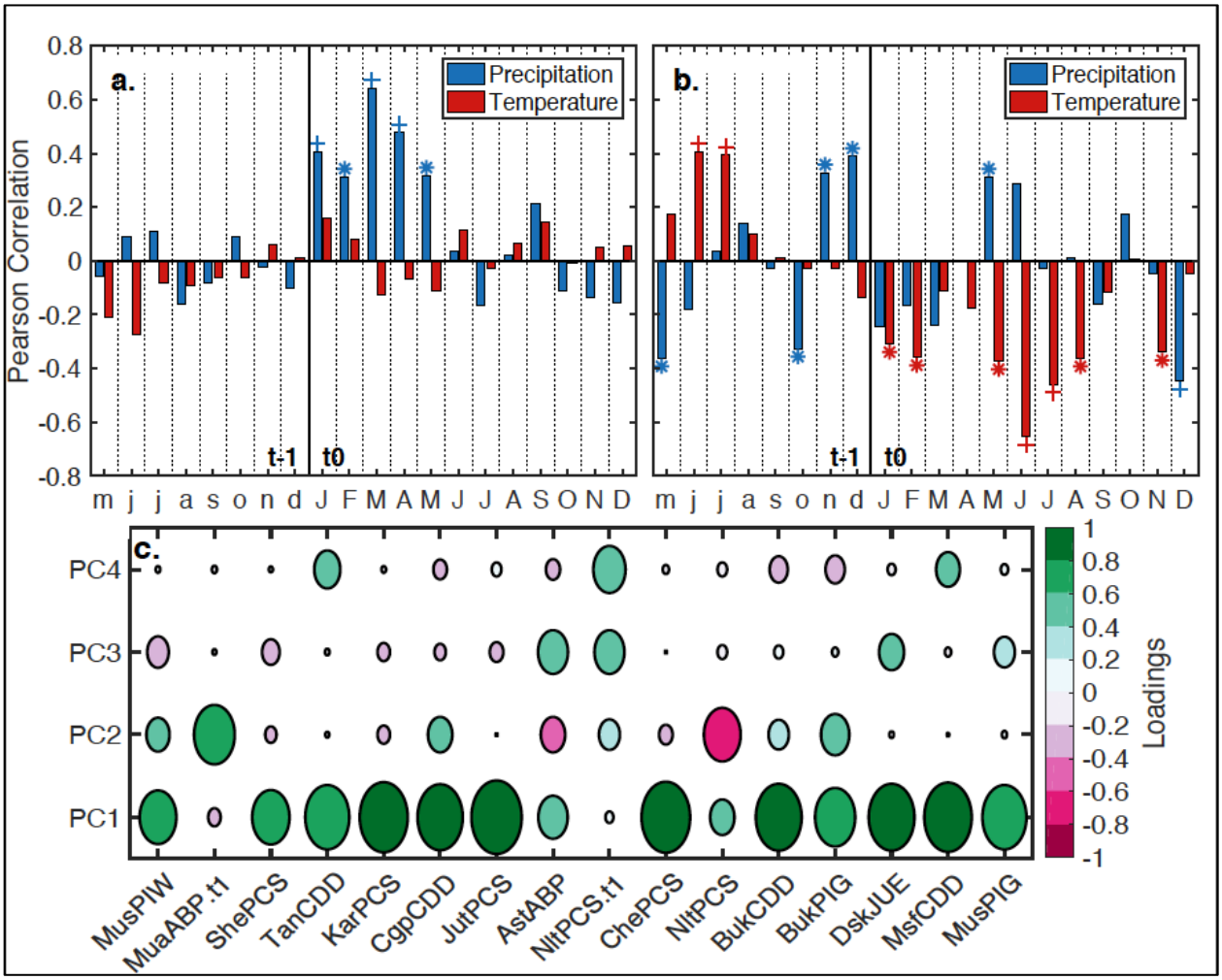

Figure 1.7 Climate response during instrumental period of the tree ring predictor suite of the first nest between 1962-2004. a.) Same as Figure 5a but PC1 time series and, b.) PC2 time series, c.) Loadings of each tree-ring series on PC1 through PC4 used in the Model I at Partab Bridge with the size of the circle and its shading are scaled to magnitude of loading on the respective PC.

1.4.4 Climate informed discharge prediction at Partab Bridge

To test if anomalies in winter precipitation and summer temperature can explain the 1990s high flow (Figure 1.4 & 1.5), we developed a multivariate regression model to predict MJJAS mean streamflow at Partab Bridge using JFM mean precipitation and MJJAS mean temperature as predictors (green line - Figure 1.8). The multivariate regression model was built using the 'raw' (i.e. not first-differenced) climate data and BR with LOOCV. This climate-informed statistical streamflow model explained ~49.34% of the variance in the instrumental data. This climate-based streamflow prediction of instrumental MJJAS discharge at Partab Bridge was compared to that predicted by the PCR and BR reconstructions (red and blue lines in Figure 1.8). The PCR and BR model estimates are significantly correlated at r=0.98 during the instrumental period between 1962-2004, and these modes each explained 52.97% and 54.43% of the variance in the instrumental data. The calibration and validation statistics of the climate-informed statistical streamflow model as measured by the CRSQ, CVRE, and RE metrics for the model are presented in Figure A.9. Using this model, we present discharge estimates of streamflow for the period between 2009 and 2016 beyond the last year of instrumental data which ends in 2008 (Figure 1.8). While the climate based model predicts the high flow in 1973 reasonably well, a year of significant UIB flooding [*Deutsch and Ruggles*, 1978], it under-predicts flow between 1991-2000 while still capturing the direction of inter-annual variability during this period. During the common period of overlap between 1962-2008 the RMSE of the BR, PCR, and climate-variable informed statistical models are 370.93 m^3/s, 373.58 m^3/s, and 421.13 m^3/s respectively, while the median-normalized RMSE are 10.19%, 10.26%, and 11.57% respectively. However, for the period of high flow between 1991-2000 the RMSE for the three models are 397.17 m^3/s, 351.75 m^3/s, and 532.52 m^3/s respectively, while the median-normalized

RMSE are 10.08%, 8.93%, and 13.52%. The greatly increased RMSE and median-normalized RMSE for the climate-variable informed model between 1991-2000 as compared to 1962-2004 indicates that the climate-informed statistical model is performing relatively poorly in this decade compared to its quality of fit over the entire instrumental period.

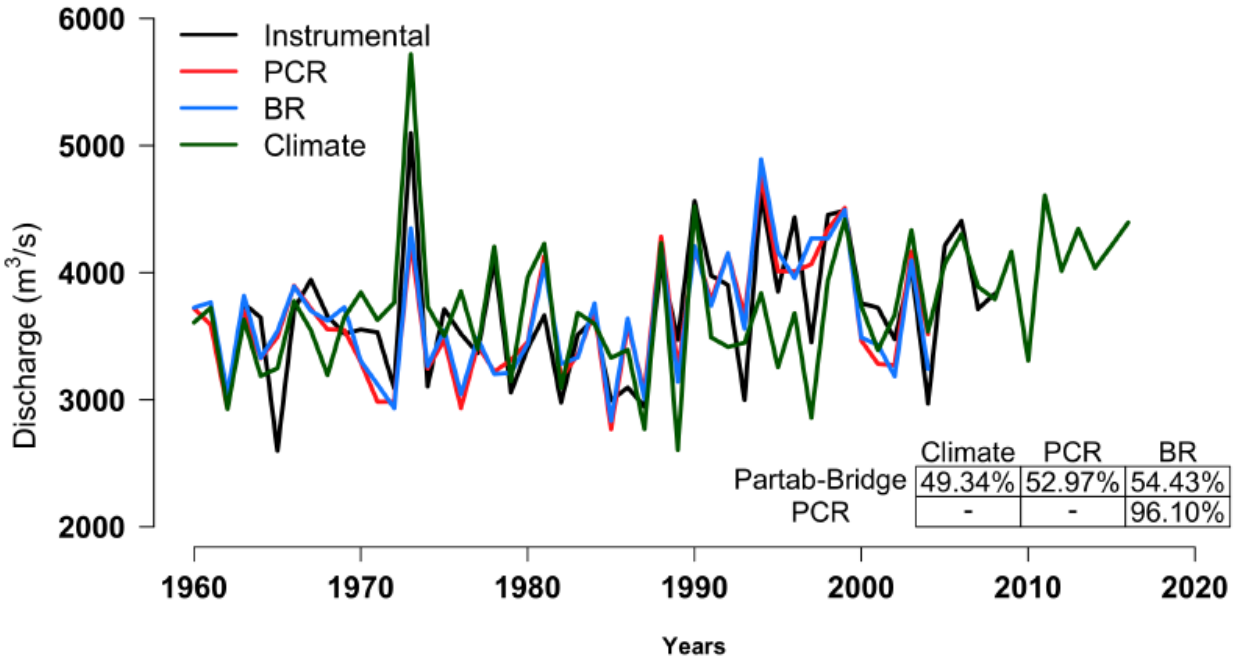

Figure 1.8 Instrumental mean MJJAS discharge at Partab Bridge (black) compared against predictions of flow (m^3/s) generated by models using PCR (red), BR (blue), and climate variables (green). Table shows R^2 across instrumental data and models.

1.5 Discussion and Conclusions

Understanding climate change and assessing recent trends in climate data requires an understanding of long-term natural variability. For the UIB, available instrumental streamflow data only span two to four decades, an insufficient time span to accurately characterize decadal to centennial timescale streamflow variability. Paleohydrologic records can play an important role in helping us extend the instrumental record to better understand these longer-term processes

[*Pages Hydro2k Consortium*, 2017; *Stockton and Jacoby*, 1976]. Our reconstructions of past discharge at four gauging stations (Partab Bridge, Doyian, Gilgit, and Kachora) extend our instrumental record of UIB discharge back six centuries to the 1400s. Our reconstructions highlight extended dry periods during the mid 1600s, late 1700s, and early 1900s that have no analogue in the short instrumental period (Figure 1.4 and 1.5) [also see *Cook et al.*, 2013b]. Further, these longer-term reconstructions of flow help us better contextualize streamflow variability during the past two decades associated with the 'Karakoram Anomaly' [*Forsythe et al.*, 2017; *Hewitt*, 2005]. The high flows in the instrumental period in the late 1980s through 1990s do appear to be unusual in the context of the past six centuries. Using the reconstructions as a reference baseline, the recent post-2000 decrease in discharge [*Archer et al.*, 2010] may represent a return to long-term mean flow conditions following the high discharge rates observed in the 1990s. At the same time, our climate-variable informed discharge predictions between 2009 to 2016 at Partab Bridge (Figure 1.8) suggest that discharge rates might be increasing after the decrease between 2000-2009 due to rising summer temperatures. However, considering the under-performance of the climate-informed model in the 1990s this result should be viewed with caution.

This most recent wet period, however, is difficult to reconcile with the main climate drivers of discharge in the region. Nevertheless, the high flow between 1991-2000 likely has climatic origins. We infer this because the tree-ring based models are able to capture the high instrumental discharge during this period. However, its proximate causes are likely not changes in JFM snowfall or summer MJJAS temperatures. This is shown by the much better prediction of high streamflow between 1991-2000 by the two tree-ring models (BR and PCR) as compared to the climate-informed model, even though all three models exhibit similar overall performance

for the entire instrumental period been 1962-2004. Specifically, the climate variable informed statistical model has a large offset in the magnitude of predicted discharge during this period despite capturing the direction of interannual variability. Although the underlying causes of this wet period still need to be investigated, they may lie in climate variability in the shoulder seasons that may be still relevant to streamflow yet not be primary controls on the interannual variability of streamflow. The reason our tree-ring model captures some of these changes may be because the tree-growth to climate response exhibits a slightly broader climate sensitivity than the streamflow data. When analyzing the instrumental precipitation and temperature data, we did not find any significant changes in monthly climate (e.g. summer precipitation) during this period. However, most of the climate records used in our discharge model come from low-elevation locations relative to the high-elevation runoff generating regions of the UIB. It is possible that some of the poorer discharge estimates maybe be a reflection of this. These low-elevation stations might not be capturing regional processes that might differentially affect high and low elevation regions, such as a preferential increase in high elevation winter snowfall [*Kapnick et al.*, 2014], or land-surface feedbacks from lowland irrigation causing high elevation snowfall [*de Kok et al.*, 2018].

Over the coming few decades, discharge in the UIB is expected to increase based on climate model predictions due to a combination of predicted warming enhancing the rate of glacial melt and increases in winter and summer precipitation [*Ali et al.*, 2015; *Brun et al.*, 2017; *Immerzeel et al.*, 2013; *Kraaijenbrink et al.*, 2017; *Lutz et al.*, 2014; *Wijngaard et al.*, 2017]. At the sub-regional level however, these changes might not be uniform. For example, the climatic controls of MJJAS discharge at Partab Bridge and Kachora are primarily wintertime (JFM) snowfall and summertime temperature, but at Doyian and Gilgit there is no temperature

dependence of streamflow. Consequently, in basins where glacial melt is important (Partab Bridge, Kachora), future warming may increase discharge as long as the remaining glacial mass can support increased flow. Assuming no increase in wintertime snowfall to offset the loss of glacier ice, this meltwater contribution to streamflow will very likely decrease sometime in the future, thus leading to a long-term decrease in discharge. In snowfall dominated sub-basins (Doyian and Gilgit) changes in streamflow are more likely to depend on changes in wintertime snowfall. At no gauge did we find a relationship between peak flow MJJAS season discharge and summertime monsoonal precipitation. This suggests that while monsoonal precipitation may play a minor contributing role in maintaining baseline flow [*Mukhopadhyay and Khan*, 2014], it is not a driver of interannual discharge variability. The spatial correlation between MJJAS flow at Partab Bridge and JFM winter precipitation shows a region of positive correlation that is relatively limited to Karakoram, Hindu Kush, Western Himalaya. This region of positive correlations broadly spans the region where winter is the most important precipitation season [*Greene and Robertson*, 2017; *Kapnick et al.*, 2014]. The region of significant positive temperature correlations with discharge extends west and southwest from the Karakoram broadly tracing the region of the Pakistan-Afghanistan border and does not extend east into the main Himalayas (Figure 1.6c). This suggests that the atmospheric processes that control temperature driven glacial melt in the summer are different for the Karakoram and the main Himalayas, consistent with the findings of *Forsythe et al.* [2017] (their Figure 2); hypothesized by them to be the position of the summertime westerly jet.

We establish that tree-ring reconstruction of past MJJAS discharge at Partab Bridge produced using PCR and BR are nearly identical in terms of the median flow reconstructed for each year. While there are differences in the widths of the uncertainties produced by the two

reconstructions, estimated from regression prediction intervals and Bayesian credible intervals respectively, these differences in uncertainties appear to be minor. We find that BR typically, but not always produces slightly wider uncertainty intervals. Commonly used statistical approaches for tree-ring reconstructions of past streamflow and climate include PCR [e.g. *Allen et al.*, 2018; *Anchukaitis et al.*, 2017; *Cook et al.*, 1999b; *Cook et al.*, 2010a; *Cook et al.*, 2013b; *Palmer et al.*, 2015; *Stahle et al.*, 2016], a Bayesian framework [*Devineni et al.*, 2013; *Luterbacher et al.*, 2016; *Steinschneider et al.*, 2017; *Tingley and Huybers*, 2010]., along with other statistical methods [e.g. *Bracken et al.*, 2016; *Gangopadhyay et al.*, 2009; *Woodhouse et al.*, 2016a]. Our results suggest that for a one predictand variable case at the Partab Bridge gauge, both PCR and BR methods produce comparable reconstructions in terms of their estimates, uncertainties, and reconstruction skill statistics. However, for a multiple-gauge network within a watershed, HBR with partial pooling provides a powerful framework to develop reconstructions of streamflow (or climate) with short instrumental records and missing data. This finding was also supported by our preliminary analysis (not presented here), where we found that our HBR model with partial pooling performed better than alternate HBR models with 'no pooling' and 'full pooling' [also see *Devineni et al.*, 2013]. Finally, we also demonstrate that the suite of tree-ring predictors used in the reconstructions have a nearly identical climate to growth response as the climate to streamflow relationship. This enhances our confidence that the reconstructions presented here capture paleo-hydrologic variability caused by past changes in these climate variables, and that these reconstructions help us better characterize longer term climate-driven decadal to centennial timescale streamflow variability within the UIB.

Acknowledgments and Data Sources

M.P.R. is grateful to funding from the Lamont Climate Center and Chevron Student Initiative Fund and thanks the Past Global Changes Paleo-Floods Working Group and Balaji Rajagopalan (CU Boulder) for helpful feedback and suggestions on the manuscript. Authors acknowledge support from NSF AGS #0402474 and U.S. Agency for International Development (USAID) NAS Grant PGA-P280423 for the original development of the tree-ring datasets used. The authors declare no conflict(s) of interest. Dataset access - CRU TS v.4.01: https://crudata.uea.ac.uk/cru/data/hrg/; Tree-ring data: https://www.ncdc.noaa.gov/data-access/paleoclimatology-data/datasets/tree-ring; Streamflow discharge data and reconstructions: Supplementary Data S1 (available online); JAGS Code: Supplementary Data S2 (available online). Lamont contribution number #8232.

Chapter 2: Seven centuries of reconstructed Brahmaputra River discharge demonstrate underestimated high discharge and flood hazard frequency

Abstract

The lower Brahmaputra River often floods during the monsoon season (July-August-September; JAS). While most climate models predict an intensified monsoon through the twenty-first century, robust baseline estimates of natural climate variability and flood hazard for the region are limited by short and fragmentary observational records. To provide a baseline assessment of Brahmaputra River hydrology, we present a new seven-century (1309-2004 C.E) tree-ring reconstruction of mean JAS Brahmaputra discharge. Our reconstruction demonstrates that the early instrumental period (1956-1986 C.E.) ranks amongst the driest of the past seven centuries (13th percentile). Further, flood hazard as inferred from the recurrence frequency of high discharge is severely underestimated between 24-38% in the instrumental record, independent of future increases suggested by RCP8.5 CMIP5 projections. Thus, a focus on only recent observations will be insufficient to determine the frequency of flood hazard for coming decades, both in the context of natural variability and climate change.

2.1 Introduction

The Brahmaputra River contributes nearly half of the ~40,000 m^3/s mean annual discharge of the Ganga-Brahmaputra-Meghna river system (Figure 2.1). This makes it the joint third largest river system in the world (tied with the Río Orinoco, Venezuela) in terms of its mean annual discharge after the Amazon and Congo rivers [*Best*, 2019]. The high discharge rates

of the Brahmaputra (Jamuna in Bangladesh) are caused, in part, by annual precipitation (rain and seasonal snow) in excess of 3,000 mm/year for much of the watershed (Figure B.1) and snowmelt from its highly glaciated upper basin encompassing the Eastern Himalaya and parts of the Southern Tibetan Plateau [*Bookhagen and Burbank*, 2010; *Immerzeel et al.*, 2013; *Maurer et al.*, 2019; *Pritchard*, 2019; *Smith and Bookhagen*, 2018]. The river and its tributaries provide important societal, ecological, cultural, and economic services to more than 60 million people in Bangladesh, North-eastern India, Bhutan, and Tibet, China [*Best*, 2019; *Mahanta and Saikia*, 2015]. These benefits include fish (a primary source of protein in the region), water to irrigate many seasonal rice varieties that need annual flood waters to survive, the deposition of fresh sediment to sustain the large inhabited riverine islands (known as *chars*), and the prevention of salt-water intrusion from the Bay of Bengal into the low-lying Sundarban delta [*Becker et al.*, 2020; *Mahanta and Saikia*, 2015; *Mondal et al.*, 2015].

Although the Brahmaputra River provides these important benefits, it is also a frequent cause of human suffering from flooding in Bangladesh and Northeast India (primarily in Assam) [*Coleman*, 1969; *Mahalanobis*, 1927]. Long-duration (>10 day) floods that cause the most widespread disruptions are most common during the monsoon season between July and September [*Chowdhury*, 2000; *Mahalanobis*, 1927; *Uhe et al.*, 2019; *Webster et al.*, 2010]. The main driver of monsoon season July-August-September (JAS) discharge in the Brahmaputra is upper basin precipitation (Figure 2.1a and Figures B.2, B.3, and B.4), along with smaller contributions from glacial melt, snow melt, and base flow [*Jian et al.*, 2009; *Lutz et al.*, 2014]. For example, the year 1998 witnessed intense monsoon flooding between July and September in both Bangladesh and Assam, inundating nearly 70% of Bangladesh, affecting over 30 million people and causing a humanitarian emergency in the region [*Chowdhury*, 2000; *Hopson and*

Webster, 2010; *Jian et al.*, 2009; *Webster et al.*, 2010]. Similar floods in 1987, 1988, 2007, and 2010 along with the currently ongoing flooding in 2020 have caused large fatalities, permanent loss of livelihoods, and the displacement of thousands of people to urban centres like Dhaka where they joined the ranks of the urban poor, in addition to raising regional food security concerns due to famine from damaged crops [*Brammer*, 1990; *Chowdhury*, 2000; *Mirza*, 2003; *Webster et al.*, 2010].

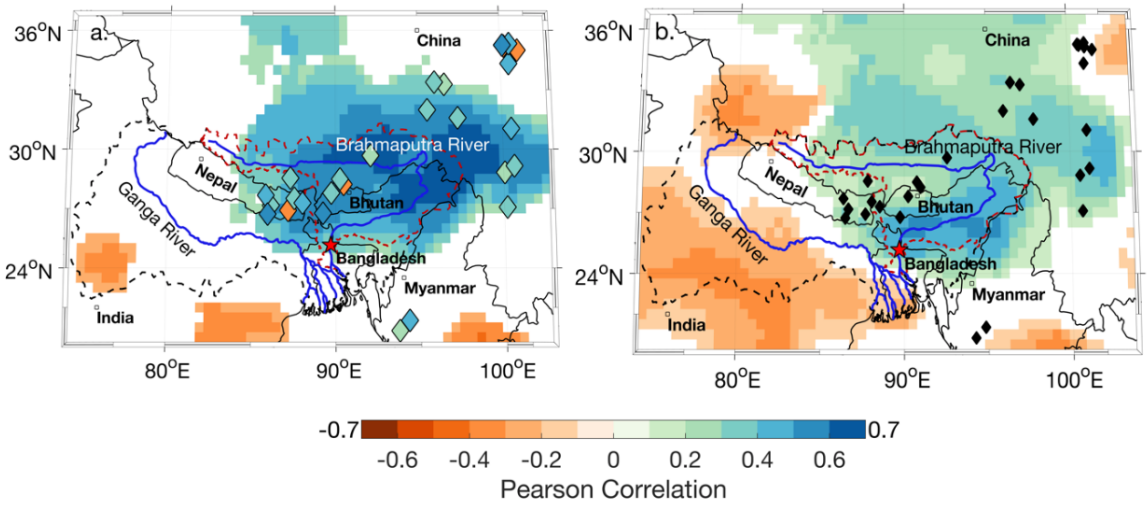

Figure 2.1 The Ganga-Brahmaputra-Meghna and Brahmaputra watersheds (black and red dashed lines), and locations of the 28 tree-ring predictors (diamonds) used in the mean July-August-September (JAS) streamflow reconstruction at the Bahadurabad gauge, Bangladesh (red star). (a.) Infill shading in diamond markers represent the Pearson correlation between mean JAS discharge at Bahadurabad and each tree ring predictor (1956-1998 C.E.). Background shading is the spatial field correlation between mean JAS discharge at Bahadurabad and mean JAS precipitation (1956-2011 C.E.) (b.) Spatial field correlation between the first principal component (PC1) of the 28 tree ring predictors (variance explained: 24.86%) and mean JAS precipitation (1956-1998 C.E.). Spatial correlations in (a) and (b) are against CRU Ts 4.01 precipitation. Together, (a) and (b) show that monsoon season JAS flow in the Brahmaputra is positively related to upper basin precipitation in a region largely co-located with the tree ring predictor network. They also demonstrate that the predictor network effectively captures regional JAS precipitation independent to its correlation with JAS Brahmaputra discharge. Note that the locations of predictors are jittered for display. Only correlations significant at $p<0.05$ using a 2-tailed t-test are shown. See Supplementary Table S1 for more information on the predictor network and Figure B.2 for similar analyses with GPCC precipitation.

While anthropogenic sulphate aerosol emissions caused a reduction in South Asian Summer Monsoon (SASM) activity during the latter half of the twentieth century [*Bollasina et al.*, 2011; *Bollasina et al.*, 2014; *Liu et al.*, 2019; *Shawki et al.*, 2018], increasing carbon-dioxide emissions and decreased aerosol loading are projected to intensify the SASM through the twenty-first century [*Turner and Annamalai*, 2012]. This intensification of the monsoon, along with accelerated warming-driven glacial melt, is expected to lead to greater flow in the Brahmaputra River [*Immerzeel et al.*, 2013; *Lutz et al.*, 2014] and likelihood of flood hazard in the region [*Gain et al.*, 2011; *Hirabayashi et al.*, 2013; *Nepal and Shrestha*, 2015; *Uhe et al.*, 2019].

Studies of long-term flood hazard in the Brahmaputra watershed have however been limited by the relatively short and fragmentary instrumental discharge records available [*Immerzeel*, 2008; *Jian et al.*, 2009]. The longest instrumental record of Brahmaputra discharge comes from the Bahadurabad gauging station in Bangladesh, shortly after the river enters the country from Assam, India (Figure 2.1). The Bahadurabad discharge record spans about six decades from 1956 to 2011, interspersed with some missing data (Figure 2.2 & Figure 2.3a). Such a short record makes it difficult to assess and put into perspective the magnitude of projected future changes relative to natural variability especially at decadal and centennial timescales [*Jian et al.*, 2009; *Turner and Annamalai*, 2012].

Tree-ring reconstructions of hydroclimate (including streamflow) are used to extend instrumental records to evaluate the severity of past droughts and pluvials [*Buckley et al.*, 2010; *Cook et al.*, 2010a; *Gou et al.*, 2007; *Pederson et al.*, 2014; *Stockton and Jacoby*, 1976; *Yang et al.*, 2014], as a reference to interpret recent climate extremes relative to those in the past [*Hessl et al.*, 2018; *Rao et al.*, 2018; *Woodhouse et al.*, 2010], and to contextualise ‘natural’ climate

variability in the system [*Li et al.*, 2019] relative to climate change projections [*Cook et al.*, 2015a; *Cook et al.*, 2010b; *Hessl et al.*, 2018]. To that end, we develop a monsoon season reconstruction of mean JAS Brahmaputra River discharge at Bahadurabad, Bangladesh.

We use our reconstruction, along with historical documentation of flood events [*Coleman*, 1969; *Mahalanobis*, 1927] to evaluate the connections between discharge and monsoon season flooding. Finally, we derive projections of future Brahmaputra River discharge from climate model simulations (historical and RCP8.5) participating in the fifth phase of the Coupled Model Intercomparison Project [CMIP5 - *Taylor et al.*, 2012]. We use these models and our reconstruction to evaluate two situations. The first is how the recurrence of high discharge events (used here as a proxy for flood hazard) in recent decades compares to longer-term estimates over the last several centuries. The second is how the increase in Brahmaputra River discharge caused by projected regional wetting [*Lutz et al.*, 2014] compares to natural climate variability estimated by the instrumental data and our tree-ring derived reconstruction. In this paper we define flood hazard as an exceedance of mean JAS discharge of 48,800 m^3/s corresponding to observed discharge in 2007, the lowest discharge of 6 instrumental period flood years between 1956-2011.

2.2 Results and Discussion

2.2.1 Seasonal hydrograph and recent flood events in the observed record

The most severe monsoon-season floods by the Brahmaputra River are those that cause inundation for more than 10 consecutive days. Such floods most commonly occur during JAS, the season with largest discharge during the year [*Webster et al.*, 2010]. The annual maximum 10-day mean discharge hydrograph at Bahadurabad between 1956-2011 shown in Figure 2.2a

describes the evolution of discharge from a dry, low-flow period between November of the prior year through May of the current year, and a period of peak discharge during the monsoon season in JAS. As tree rings typically provide information regarding seasonal hydroclimate [*Meko et al.*, 1995], we then attempted to determine whether JAS monsoon season discharge is related to sub-seasonal flow at the 10-day timescale relevant to regional flooding. We found a strong and significant positive relationship between mean JAS seasonal discharge and the maximum 10-day mean discharge in each year (Spearman r=0.79; Pearson r=0.82; n=55, $p<0.001$, Figure 2.2b). This coupling between 'instantaneous' and 'seasonal' discharge is a common feature among large river basins across the world including the Brahmaputra [*Immerzeel*, 2008; *Milly et al.*, 2002].

This relationship is further supported by comparing the 10-day mean discharge hydrograph of six instrumental period flood years (i.e. 1966, 1987, 1988, 1998, 2007, and 2010) to the overall 10-day mean discharge hydrograph between 1956-2011 [Figure 2.2a; also see *Jian et al.*, 2009]. In each of these known flood years, 10-day mean discharge exceeded the 50th and 95th percentile of daily discharge for an extended duration. The median number of discharge days that exceeded the 50th percentile and 95th percentile of daily JAS discharge during these flood years were 76 and 17 respectively, representing 82% and 18% of the total of 92 days in the 3-month JAS period (Figure B.5). In particular, in the year 1998, peak 10-day mean discharge was ~94,000 m^3/s. This was greater than twice the median flow for the season [*Best*, 2019; *Chowdhury*, 2000; *Jian et al.*, 2009], with daily flow exceeding the 95th percentile of daily flow for a total of 39 of the 92 days, or 42% of the days in the JAS season. These results confirm the use of JAS discharge as a proxy for 10-day discharge and as an indicator for the likelihood of

flood hazard.

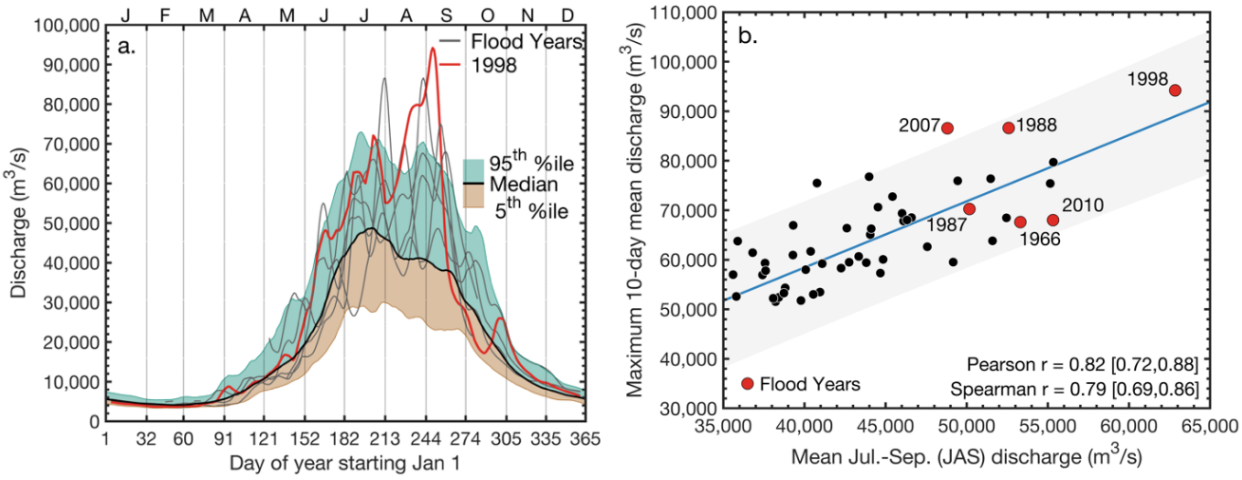

Figure 2.2 Brahmaputra River discharge characteristics at Bahadurabad, Bangladesh between 1956-2011 C.E. (a.) Annual 10-day mean discharge hydrograph. The brown and green envelopes represent the 5th, 50th, and 95th percentiles of 10-day mean discharge respectively. The 5 grey and 1 red line represent 10-day mean discharge during instrumental period flood years in 1966, 1987, 1988, 1998 (in red), 2007, and 2010 C.E. (b.) Scatter plot of mean JAS discharge against maximum 10-day mean daily discharge. The six flood years are highlighted in red. The bootstrapped Pearson and Spearman rank correlations are calculated as the median and 5th and 95th percentile of 1,000 draws with replacement. The grey uncertainty envelope (±2σ) is derived from the best-fit linear regression (blue line).

2.2.2 Predictor selection and reconstruction model fidelity

To extend the short instrumental record, we developed a reconstruction of mean JAS monsoon season discharge extending from 1309-2004 C.E. (Common Era) for the Brahmaputra River at Bahadurabad, Bangladesh, using Bayesian Regression (see Methods section). We used a pool of 28 annually dated tree-ring series that were proximally located to the Brahmaputra watershed boundary (Table B.1). All chosen series correlate well with mean JAS streamflow at Bahadurabad ($p<0.10$, using a 2-tailed t-test) during the 1956-1998 model calibration-validation period. Of these 28 predictors, 5 are located relatively distant (~670 km) to the watershed. We retained these 5 predictors as they contributed additional model skill, as is commonly found in

tree-ring hydroclimate and streamflow reconstructions [*Allen et al.*, 2013; *Chen et al.*, 2019; *Littell et al.*, 2016b; *Martin et al.*, 2019; *Palmer et al.*, 2015; *Stockton and Jacoby*, 1976], consistent with spatial autocorrelation in climate fields [*Harris et al.*, 2014a; *Ljungqvist et al.*, 2016; *Yatagai et al.*, 2012].

The first principal component (PC1) of the 28 tree-ring predictors explained 24.86% of the total variance in the set of predictor chronologies. The PC1 timeseries of these predictors also correlated significantly with JAS discharge at Bahadurabad between 1956-1998 ($r=0.73$, $n=42$, $p<0.01$, 2-sided t-test), and with mean JAS precipitation in the Brahmaputra basin (Figure 2.1b and Figure B.2b). The loadings of each predictor on PC1 (and PC2) are described in Table B.1. The correlation between the PC1 series and regional precipitation in Figure 2.1b indicates that the 'shared variance' between the selected predictors captures regional hydroclimate variability independent to their statistical relationship with Brahmaputra streamflow.

Median calibration-validation statistics of our reconstruction between 1309-2004 C.E. are as follows: i. CRSQ (calibration period coefficient of multiple determination): 65.58%, ii. VRSQ (validation period square of the Pearson correlation): 45.61%, iii. VRE (validation period reduction of error): 0.41, and iv. VCE (validation period coefficient of efficiency): 0.31. A comparison of the correlations between reconstructed discharge and upper basin climate variables indicates that the reconstruction captures the climate-streamflow relationships inherent in the instrumental observations (Supplementary Fig. S4). However, these climate-streamflow relationships are slightly weaker for reconstructed discharge than for instrumental discharge. The calibration-validation statistics for each model nest are shown in Figure B.6 along with the number of tree ring predictors used in each nest (maximum 28, minimum 10). That VRE and

VCE values are consistently greater than zero across the full reconstruction period indicates that the model has some skill [*Cook et al.*, 2010a].

2.2.3 Reconstruction of past discharge

The reconstructed discharge estimates during the observational period are shown in Figure 2.3a and our full reconstruction between 1309-2004 C.E. is presented in Figure 2.3b. While the reconstruction is calibrated to the instrumental mean and variance in the reconstruction procedure (Figure 2.3 c-d), we found that the mean reconstructed discharge over the full reconstructed period between 1309-2004 C.E. was significantly higher than the instrumental mean between 1956-2011 C.E. (46,993 ± 812 m^3/s cf. 43,350 m^3/s, difference of means = 3,644 m^3/s, t-statistic = 5.11, $p<0.01$) (Figure 2.3a). The uncertainty range around the mean was derived from the 5th and 95th percentiles of the means across all 400 iterations of the median reconstruction. The reconstruction was also significantly ($p<0.01$) wetter than the instrumental period even if we used the 1956-2004 C.E. instrumental mean of 43,442 m^3/s or the 1956-1998 C.E. calibration-validation period instrumental mean of 43,233 m^3/s. This difference between the instrumental and reconstructed mean is largely driven by the first three decades of the instrumental observations between 1956-1986 C.E. that was unusually dry in the long-term context of the past seven centuries [*Wang et al.*, 2020]. The instrumental mean between 1956-1986 C.E. was 41,206 m^3/s. We also compared mean JAS discharge during these 4 intervals (i.e. 1956-1986, 1956-1998, 1956-2004, and 1956-2011) to random block bootstrap draws from the full reconstruction. We found all four intervals to be significantly drier ($p<0.05$) than the reconstruction (Figure B.7).

The 31-year 1956-1986 C.E. instrumental mean of 41,206 m^3/s ranked in the 13th percentile of our 696-year reconstruction. The 1956-2004 C.E. mean of 43,233 m^3/s and the full

56-year 1956-2011 C.E. instrumental mean of 43,350 fell in the 22nd percentile of the full reconstruction. These results highlight the unusually dry nature of the modern instrumental period relative to the full reconstructed record, although we do observe dry periods of similar or greater magnitude in the early 1400s, late 1600s, early 1800s, and late 1800s (also see Figure B.8 and refs. [*He et al.*, 2018; *Wang et al.*, 2020] for perspectives on upper Brahmaputra watershed May-June hydroclimate, and refs. [*Shah et al.*, 2014; *Thapa et al.*, 2017]). On the other hand, the reconstruction indicates long multidecadal wet periods of above normal discharge between ~1560-1600 C.E., 1750-1800 C.E., and ~1830-1860 C.E. that have no analogues in the instrumental data (Figure 2.3, Figure B.8, also see ref. [*He et al.*, 2018]). We do note that both instrumental observations and the reconstructions show a return to wetter conditions starting in 1987 [also see refs. *Chen et al.*, 2020; *Shi et al.*, 2018a]. For example, more recent instrumental observations of discharge between 1987-1998 C.E., 1987-2004 C.E., and 1987-2011 C.E. are relatively wetter than the instrumental data prior to 1987 and fall in the 59th, 48th, and 39th percentile of full reconstruction (Figure B.8). However, the lack of more up-to-date streamflow data preclude us from being able to contextualise more recent years of discharge relative to the longer term reconstructed mean.

2.2.4 Historical flood events

Next, we evaluated the relationship between discharge and 12 historical Brahmaputra flood years in 1787, 1842, 1858, 1871, 1885, 1892, 1900, 1902, 1906, 1910, 1918, 1922 C.E. identified [from refs. - *Chowdhury*, 2000; *Coleman*, 1969; *Mahalanobis*, 1927] and 6 recent instrumental period flood years in 1966, 1988, 1987, 1998, 2007, 2010 C.E.[*Jian et al.*, 2009]. These flood years (18 total) are marked as red triangles in Figure 2.3b. The mean observed JAS discharge during these six instrumental period flood years was ~53,800 m^3/s (purple line in

Figure 2.3c). The reconstructed discharge of 60,312 m^3/s in 1998 C.E. that was concurrent with large scale flooding in Bangladesh is only exceeded five times in the 696-year reconstruction. While our reconstruction model underpredicts the instrumental discharge of 62,840 m^3/s in 1998 C.E. by ~2,500 m^3/s (Figure 2.3a), this comparison still suggests that within the reconstruction, discharge that year was unusually high [*Chowdhury*, 2000; *Jian et al.*, 2009] even in the long-term context of the past seven centuries.

Following this, we tested the probability of random association between the 16 flood years and high discharge over the reconstruction period (excluding 2007 and 2010 as the reconstruction ends in 2004) using superposed epoch analysis [SEA - ref. *Rao et al.*, 2019]; see Methods). We found that mean reconstructed flows across these 16 years are significantly wetter ($p<0.001$) and approximately one standard deviation higher than would be expected by chance (Figure 2.4a). This result is consistent with our finding using the instrumental discharge data (Figure 2.2) that flood events co-occur with high seasonal JAS discharge. However, we found this relationship to be much weaker in the reconstructions. Six of the 12 pre-1956 C.E. flood events occurred in relatively dry years. SEA of the 12 flood years prior to 1956 did show a median result of wet conditions in the year in which a flood was documented (Figure B.9). However, this result was not statistically significant at $p<0.05$ despite the 95th percentile of bootstrapped discharge responses being significant at $p<0.001$. This asymmetric response may be partly due to some of these historical flood years being undivided Bengal (Bangladesh, and West Bengal, India) flood years and not solely Brahmaputra flood years, and lack of information regarding the magnitude of flooding in the historical sources that we used.

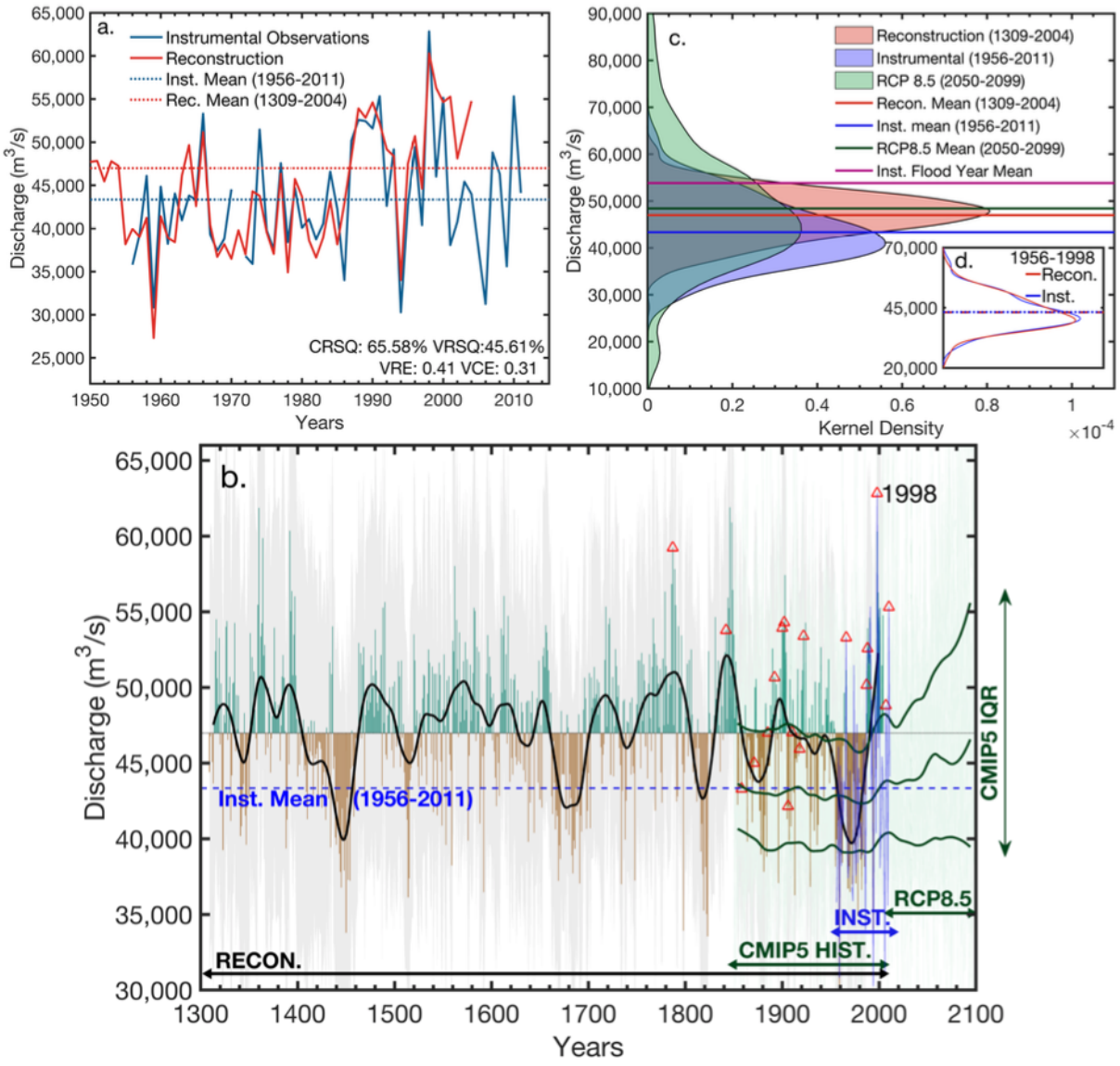

Figure 2.3 Instrumental observations, the reconstruction, and CMIP5 projections of mean JAS discharge at Bahadurabad. (a.) JAS instrumental discharge and its mean (43,350 m3/s) compared against reconstructed JAS discharge and its long-term mean (46,993 ± 812 m3/s). (b.) Reconstructed discharge for each year between 1309-2004 C.E. as a departure from the reconstructed mean (as green and brown bars), along with the 50-year low-pass filtered reconstruction (solid black) highlighting multi-decadal variability. The instrumental JAS discharge and its mean between 1956-2011 C.E. is shown in the blue and dashed blue lines respectively. Red triangles mark 18 documented flood years between 1787 and 2010 C.E. The 3 dark green lines represent the 50-year low-pass filtered interquartile range (IQR – 25th, 50th, and 75th percentiles) of the multi-model CMIP5 RCP8.5 ensemble (20 models; 42 runs; Table B.2) along with the full range of variability (light green lines) during both the 'historical' (1850-2005 C.E.) and 'future' (2006-2099 C.E.) simulation period of these runs. (c.) Kernel density profiles of the median reconstruction (in red), instrumental period (in blue),

the full 42 member CMIP5 RCP8.5 end of the century simulation period (2050-2099 C.E.) ensemble suite (in green) and their respective means. The observed mean discharge of the 6 instrumental period flood years from Figure 2.2 are shown in purple. The inset figure (d) shows the kernel density profiles of mean JAS instrumental discharge (in red) and reconstructed mean JAS discharge (in blue) over the calibration-validation period (1956-1998 C.E.) along with their means. The reconstruction matches the features of instrumental discharge such at its mean and variance in this period.

2.2.5 Projections of future discharge

We calculated projections of runoff for the Brahmaputra River at Bahadurabad using an ensemble of 20 CMIP5 climate models (42 ensemble members) that provided continuous simulations from 1850 through 2099 C.E. (historical simulation from 1850-2005 C.E.; high emissions RCP8.5 scenario from 2006-2099 C.E.) (Table B.2). During the historical simulation period, the multi-model ensemble interquartile range (IQR – 25th, 50th, and 75th percentiles) of the 20 climate models shows a decreasing trend from ~1940-1980 C.E. (shown in solid green, Figure 2.3b), with a recovery in discharge between 1980-2005 C.E. Future projections of the IQR of multi-model ensemble discharge suggest a large increase in discharge relative to the instrumental mean starting ~2025 C.E. that is expected to persist and intensify through to the end of the century.

We find that towards the end of the century, between 2050-2099 C.E., the 25th percentile of CMIP5 multi-model discharge remains relatively constant but there are large increases in the 50th and 75th percentiles of projected discharge. This can also be observed in a comparison of the kernel density profile of all 42 ensemble members of CMIP5 RCP8.5 scenario discharge projections between 2050-2099 C.E., compared to the kernel density profiles of both the instrumental data between 1956-2011 C.E. and the full period of the reconstruction between 1309-2004 C.E. (Figure 2.3c). The kernel density profile of discharge over instrumental observations between 1956-2011 C.E. and the horizontal line representing the instrumental mean

in this period also illustrate that the instrumental observations are drier than the long-term mean variability in the river system suggested by the reconstruction, and likely drier than future projected runoff.

2.2.6 High discharge related flood hazard relative to instrumental observations

We then calculated the difference in the likelihood of high discharge in the instrumental observations (1956-2011 C.E.) against the final median reconstruction (1309-2004 C.E.) and the 20 model CMIP5 RCP8.5 end-of-the-century discharge projections split between 2050-2074 C.E. and 2075-2099 C.E. We divided the end-of-the-century CMIP5 RCP8.5 discharge simulations into two halves (2050-2074 C.E. and 2075-2099 C.E.) to estimate the sensitivity of our results to different levels of global mean warming relative to the pre-industrial era with continued anthropogenic carbon-dioxide emissions under the RCP8.5 scenario (+3.05°C by 2050-2074 C.E., and +4.30°C by 2075-2099 C.E.; Figure B.10). The 3.05°C warming of global mean annual temperatures that we estimate here by 2050-2074 C.E. under RCP8.5 is roughly equivalent to the projected warming that will be achieved by 2099 C.E. under the lower emission RCP4.5 scenario [see Figure 1 in *Knutti and Sedláček*, 2013]. Using these datasets, we then calculated the recurrence interval of JAS discharge greater than 48,800 m^3/s (Figure 2.4b). This discharge exceedance threshold was equal to JAS discharge in 2007 C.E., the lowest discharge of all instrumental period flood years (Figure 2.2b). The recurrence intervals were calculated by sampling 1,000 draws of 30 years with replacement from all datasets (see Methods section).

The median recurrence intervals (in years) were: (i) 4.35 for the instrumental observations between 1956-2011 C.E., (ii) 3.57 for the reconstruction between 1956-2004 C.E., (iii) 2.7 for the full reconstruction (1309-2004 C.E.), (iv) 2.5 across all RCP8.5 discharge projections between 2050-2074 C.E., and (v) 2.17 for RCP8.5 discharge projections between

2075-2099 C.E.. The median recurrence interval for instrumental observations between 1956-2004 C.E. and 1956-1998 C.E. were also 4.35 (Figure B.11).

The estimated difference in the recurrence of high discharge greater than 48,800 m^3/s between the full reconstruction relative to recent decades therefore lies between 24.37-37.93%, calculated as (3.57-2.7)/3.57*100 and (4.35-2.7)/4.35*100. As our reconstruction shows a slight wet bias with more recurrent exceedances of the flooding threshold relative to observations over the instrumental period (3.57 years cf. 4.35 years), the 24.37% lower bound of our estimate accounts for this bias explicitly by comparing the full reconstruction only against tree-ring reconstructed instrumental period flows. However, there is substantial overlap in the full distributions of flood hazard recurrence intervals calculated during the instrumental observations (1956-2011 C.E.) and the reconstruction's instrumental period (1956-2004 C.E.) (first two columns in Figure 2.4b). This result remains consistent even if we use instrumental observations between 1956-2004 C.E. or 1956-1998 C.E. (Figure B.11).

The difference in the recurrence of high discharge greater than 48,800 m^3/s between the instrumental data and CMIP5 RCP8.5 in the intervals spanning 2050-2074 C.E. and 2075-2099 C.E. are 42.53% and 50.11% respectively [also see *Whitehead et al.*, 2015]. Therefore, using the reconstruction as a baseline for long-term discharge variability and the CMIP5-simulated discharge as an estimate of climate change impacts on discharge in the basin, we find that recent decades underestimate the frequency of high discharge and in turn flood hazard from natural variability by 24.37-37.93% and climate change impacts by 42.53-50.11%.

In the instrumental observations, mean JAS discharge exceeded 48,800 m^3/s in 13 years (Figure 2.2b). Despite high discharge during these 13 years, more than half of these years (n=7) experienced no flood. While our recurrence interval analysis focusses on the frequency of high

discharge that is associated with the likelihood of flood hazard, many other factors play a role in determining whether high discharge translates to a flood event. These may include rainfall intensity and pattern, landscape heterogeneities, antecedent soil moisture conditions, and land use and forest cover change [*Blöschl et al.*, 2017; *Bradshaw et al.*, 2007; *Cox et al.*, 2002]. Our return interval analyses also rely on the assumption that these high discharges will continue to be associated with an increased likelihood of flood hazard in the future, disregarding (for example) potential changes in policy, land use, or infrastructure that may ameliorate 'flood risk'. The occurrence of a flood event that impacts society is however closely intertwined with highly localised human exposure and vulnerability [*McGlade et al.*, 2019; *Winsemius et al.*, 2013]. Therefore, our calculations of underestimated high discharge and associated likelihood of flood hazard in the return interval analyses in Figure 2.3b only contributes one component of the multiple dimensions of flood risk.

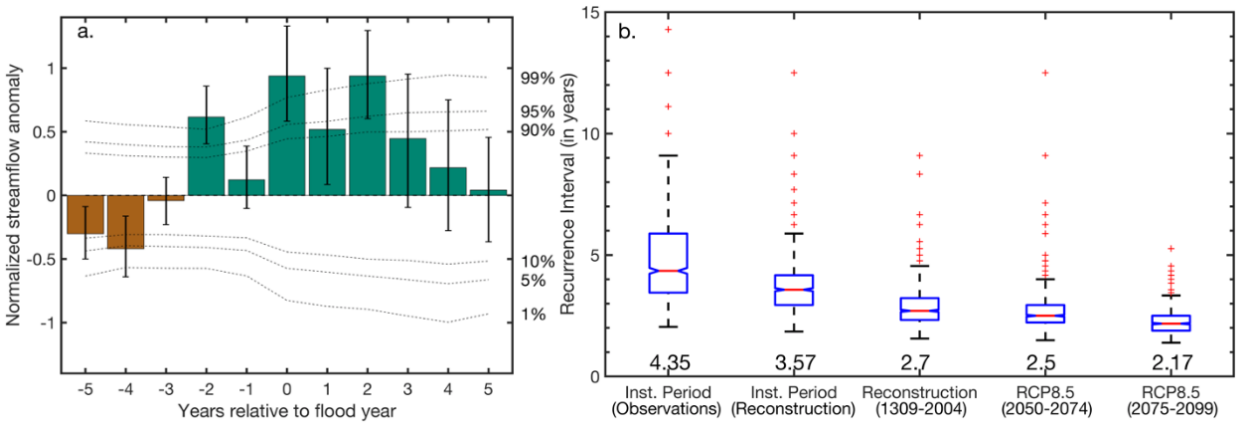

Figure 2.4 Discharge characteristics of wet and dry periods and flood years (a.) Superposed Epoch Analysis (SEA) showing higher than normal flows in historical and instrumental period flood years (in year t+0) between 1780-2004 C.E. than would be expected by chance. The response is the 5th, 50th, and 95th percentiles of mean flow across 1,000 unique draws of 10 flood years at random out of 16. The horizontal dotted lines indicate the threshold required for epochal anomalies to be statistically significant using random bootstrapping at three different statistical thresholds. These thresholds were calculated by compositing 10,000 draws of 10 years at random (or 'pseudo-flood years') from the reconstruction between 1780 and 2004 C.E. (b.) Recurrence intervals (in years) of discharge greater than the 2007 C.E. flood

year JAS discharge calculated from 1,000 draws of 30 years with replacement form the instrumental data (1956-2011 C.E.), the reconstructions (over the instrumental period, 1956-2004 C.E.), and the full 42 ensemble member CMIP5 RCP8.5 simulation suite between 2050-2074 C.E. and 2075-2099 C.E. The median recurrence interval for each dataset is noted below each boxplot. The median recurrence interval for instrumental discharge between 1956-2004 C.E. and 1956-1998 C.E. remains 4.35 (Fig B.8).

2.3 Climate teleconnections

We did not find any meaningful or statistically consistent relationship between monsoon season flow in the Brahmaputra River and variance in ocean sea surface temperatures (SSTs) or indices such as the El Niño-Southern Oscillation (ENSO) or the Indian Ocean Dipole (IOD) (Figure B.12). This is consistent with prior studies [*Immerzeel*, 2008; *Jian et al.*, 2009; *Shaman et al.*, 2005], even though we used a more up-to-date discharge dataset that extends up through 2011.

2.4 Conclusions

We found the magnitude of peak 10-day Brahmaputra River discharge during the JAS monsoon season is tightly coupled to mean discharge for the entire JAS monsoon season. We also show that flood events have almost always occurred during years of high seasonal discharge. Our tree-ring reconstruction of mean JAS Brahmaputra River discharge between 1309-2004 C.E. helps inform us about past and long-term hydroclimate variability in this river system. Additionally, the frequency of recurrence of high discharge in the reconstruction relative to the instrumental observations provides us valuable information regarding the likelihood of flood hazard in the region. While the Brahmaputra River has experienced large floods in the past few decades, most notably in 1998 C.E., our reconstruction suggests that the instrumental period that informs our current baseline assessments of flood hazard in the region is actually one of the

driest periods over the past seven centuries. This finding and the wet and dry periods we described in our reconstruction are also consistent with other hydroclimate reconstructions in the Southeast Tibetan Plateau covering the upper Brahmaputra watershed [*He et al.*, 2018; *Liu et al.*, 2012; *Wang et al.*, 2020]. Climate model simulations under the RCP8.5 scenario suggest wetting over the Brahmaputra River basin leading to increased discharge towards the end of the twenty-first century. While this projected wetting falls within paleo-discharge natural variability estimates, taken in conjunction, the wetter reconstruction and projections relative to the instrumental period suggest that we may be currently underestimating the reconstructed and future frequency of high discharge in the Brahmaputra River watershed.

A limitation of our analyses regarding flood hazard is that we reconstruct Brahmaputra mean JAS monsoon season discharge and not flood years per se. Improved paleo-hydrology work in other archives, such as geomorphic evidence and field stratigraphy [*Ely et al.*, 1996; *Kale et al.*, 1994; 1996; *Thomas et al.*, 2007], the documentation of tree-ring flood-scars that can precisely date past flood events [*Ballesteros-Cánovas et al.*, 2015; *Speer et al.*, 2019; *Wilhelm et al.*, 2019], and additional tree-ring sampling in the region of traditional [*Thapa et al.*, 2017] and non-traditional species [*Chowdhury et al.*, 2016; *Islam et al.*, 2018; *Maxwell et al.*, 2018] can help establish more skillful reconstructions of Brahmaputra discharge, its flooding history, and its flooding frequency in future work [*Allen et al.*, 2020]. Additionally, we focus on the likelihood of high discharge as a proxy for flood hazard, and not on flood exposure and vulnerability [*Kundzewicz et al.*, 2018; *Winsemius et al.*, 2016]. In recent years, large advances have been made in the region with accurate flood warnings being made available with lead times of ~8-10 days. Villages taking specific actions have been able to minimise economic and social loss. Therefore, developing such adaptive capabilities to extreme events lends well towards

better preparedness in times of increased flood hazard to reduce overall risk. Finally, as lower basin Brahmaputra discharge in Bangladesh is closely tied to upper basin discharge and precipitation, greater availability of real-time river discharge data across all basin states (China, India, Bhutan, and Bangladesh) will help advance these efforts.

Acknowledgements

M.P.R. supported by Lamont Climate Center, Lamont Chevron Student Initiative Fund, and National Science Foundation (NSF) Office of Polar Programs (OPP) Arctic Social Sciences award #1737788. E.R.C by the Lamont Climate & Life fellowship. B.I.C supported by NASA Modeling, Analysis, and Prediction program, M.P.R, R.D.D., and B.M.B acknowledge NSF Atmospheric & Geospace Sciences (AGS) award #1303976. D.A.B. supported by the NASA Earth and Space Science Graduate Student Fellowship #80NSSC17K0402. P.J.W. supported by NSF-AGS grant #1638256. M.P.R. thanks Naresh Devineni (CUNY-NY) and Nguyen Tan Thai Hung (SUTD) for helpful discussions. Authors thank Haibo Liu (Columbia Univ.) for assistance with CMIP5 data, Daniel Stahle and Nguyen Trung for helping develop the 2 Myanmar tree ring series, and Matthew Therrell (Univ. of Alabama) and 2 anonymous reviewers for the comments that helped improve our manuscript and analyses. Lamont contribution number: xxx (provided after conditional acceptance).

Author Contributions

M.P.R, E.R.C, and B.I.C. designed research. M.P.R. preformed research and wrote the paper with substantial input from E.R.C., B.I.C. and R.D.D. Research ideas were contributed by

J.G.P., U.L., C.W., B.M.B, M.U., and D.A.B. J.J. and P.J.W. provided the streamflow data and assisted in its interpretation. All authors edited the manuscript.

Competing Interests

Authors declare no competing interests.

Data and Code Availability

Tree Ring Data from International Tree Ring Data Bank (ITRDB) - https://www.ncdc.noaa.gov/data-access/paleoclimatology-data/datasets/tree-ring. Tree ring data are from refs. - [*Cook et al.*, 2003; *Cook et al.*, 2010a; *Cook et al.*, 2013a; *Gou et al.*, 2007; *Krusic et al.*, 2015; *Li et al.*, 2017]. CMIP5 data - https://esgfnode.llnl.gov/search/cmip. *Huffman et al.* [2007] TRMM precipitation data from the IRI Data Library at http://iridl.ldeo.columbia.edu/SOURCES/.NASA/.GES-DAAC/.TRMM_L3/.TRMM_3B42RT/.v7/.daily/.precipitation/; [*Harris et al.*, 2014a] CRU data http://www.cru.uea.ac.uk/data/; [*Schneider et al.*, 2017] GPCC v7 precipitation data - https://www.esrl.noaa.gov/psd/data/gridded/data.gpcc.html#detail; ERA-5 [*Copernicus Climate Change Service (C3S)*, 2019] runoff - https://cds.climate.copernicus.eu/cdsapp#!/dataset/reanalysis-era5-land-monthly-means?tab=form.

We downloaded shapefiles for country boundaries from https://github.com/nvkelso/natural-earth-vector/ and the authors and publisher remain neutral regarding them. Reconstructions and Bangladesh Meteorological Department (BMD)

Bahadurabad instrumental discharge data will be made available through to the NOAA-NCEI Paleoclimatology Data repository at: http:xxx. They are also available in Supplementary Data 1 along with all 28 standardised tree-ring predictor series and our R and JAGS code. Any other associated data may also be made available by request from the authors.

Methods

Tree Ring Network. As an initial selection criterion, we first downloaded tree-ring data located between 20°N-35°N and 86°E-101°E available in the International Tree Ring Databank (ITRDB) that are approximately located within ~670 km or less from the basin boundaries, consistent with spatial auto-correlation in regional hydroclimate [*Cook et al.*, 2010a]. We then 'standardized' [*Cook and Kairiukstis*, 1990; *Fritts*, 1976] each of annual raw ring-width series using the signal free (SF) method [*Melvin and Briffa*, 2008] to reduce the influence of non-climatic growth factors on tree growth and maximize the preservation of common median frequency at decadal to centennial timescales and truncated each chronology to the section with an Expressed Population Signal > 0.85 [*Cook et al.*, 2013b; *Wigley et al.*, 1984]. Finally, we retained a tree-ring series as a potential predictor if it correlated significantly with $p<0.1$ using a 2-tailed t-test with mean JAS flow at Bahadurabad, Bangladesh in its 'raw' and 'pre-whitened' (i.e. serial-autocorrelation removed) forms. We allowed for the inclusion of lag t+1 predictors in our model, where tree-growth lagged climate and consequently streamflow by one year. This is because tree-growth in the current year is often influenced by previous year climate [*Fritts*, 1976]. The details of the series (e.g. species, location, chronology length, lag t+0 or lag t+1) retained as predictors in our reconstruction model are described in Supplementary Appendix, Table S1. The two tree ring series located in Myanmar are developed by us.

Reconstruction. We used the Bayesian Linear Regression model prescribed below [*Devineni et al.*, 2013; *Rao et al.*, 2018] to reconstruct streamflow (y_t) in year t, as function of an intercept, slope, and predictor vector X.

$$y_t|\alpha,\beta = \alpha + \beta * X_t + \varepsilon_t$$

with non-informative priors modelled as

$$\alpha \sim N(0,10^4) \text{ and } \beta \sim N(0,10^4)$$

The matrix **X** in the equation above contained the Principal Component scores ([PCs - ref. *Cooley and Lohnes*, 1971]) for all tree ring predictors with eigenvalues greater than 1. We used this Kaiser-Guttman cutoff criteria [*Guttman*, 1954; *Kaiser*, 1960] as an estimate of common shared signal (versus noise) between the tree ring predictors. In the reconstruction procedure, we explicitly incorporated the covariance between the streamflow series and the tree-ring series by weighting each tree-ring predictor series by a power of its correlation with the streamflow data during the 1956-1998 C.E. calibration period [*Cook et al.*, 2019]. This weighting can be expressed by the following equation

$$wTR = uTR * r^p$$

where wTR represents the final correlation-weighted matrix of tree ring chronologies, uTR is the matrix of unweighted tree-ring series normalized to N(0,1) over the calibration period, r is the absolute value of the calibration period Pearson's correlation, and p is a range of exponent powers (0, 0.1, 0.25, 0.5, 0.67, 1.0, 1.5, 2.0) [*Cook et al.*, 2010a; *Cook et al.*, 2013b]. We use this range of powers, as there is no *a priori* reason for any single correlation weight to be more suitable than any other weight [*Cook et al.*, 2010a; *Cook et al.*, 2013b].

To develop the reconstruction, we chose the 43-year period between 1956-1998 C.E. as calibration-validation period to maximize the number of tree-ring predictors available as most tree-ring series ended in 1998 C.E. We used a 'nested' reconstruction approach where we sequentially dropped shorter tree-ring series until the predictor suite was exhausted and developed a new reconstruction model each time a shorter tree-ring series was dropped. We then appended each reconstruction 'nest' together by scaling its variance to the calibration period to develop the longest possible reconstruction of flow possible. Due to the relatively short instrumental period of 43 years (1971 missing) available for calibration-validation, we used a leave-10-out at random calibration-validation approach. In each iteration we calibrated a model on 32 years of streamflow data and validated it on the remaining 10 years. This choice of a 32-year calibration and 10-year validation period provided a trade-off between retaining sufficient years for calibration while developing a conservative estimate of model skill. This is because leave-one-out-cross-validation skill thresholds are easier to pass than leave-k-out validation. For each nest and for each PCA matrix correlation weight, we developed 50 such reconstructions. These 50 leave-10-out-cross-validations when taken together with the 8 different correlation weights used in the PCA analysis gave us 400 reconstructions. The final reconstruction shown in Fig. 3 was calculated as the median of this 400-reconstruction ensemble.

We evaluated the fidelity of our reconstruction using the following metrics: (i) CRSQ (calibration period coefficient of multiple determination), (ii) VRSQ (validation period square of the Pearson correlation), (iii) VRE (validation period reduction of error), and (iv) VCE (validation period coefficient of efficiency) that is equivalent to the Nash-Sutcliffe efficiency test[*Nash and Sutcliffe*, 1970]. The full description of these metrics is provided in the

supplemental material in Cook et al. [ref. - *Cook et al.*, 2010a]. The CRSQ and VRSQ were calculated on the 32-year calibration and 10-year validation periods respectively.

Flood hazard and recurrence interval. The list of flood years prior to the start of the instrumental gauge records in the 1950s at Bahadurabad were primarily collated from Coleman et al. and Chowdhury et al. [refs. - *Chowdhury*, 2000; *Coleman*, 1969]. Flood years from these two studies include 1842, 1858, 1871, 1885, 1892, 1900, 1902, 1906, 1918, and 1922 C.E. Additional records of Brahmaputra floods in 1910 C.E. and in 1787 C.E., when severe heavy rains in the upper basin caused a major flood, and the Teesta River changed its course to flow into the Brahmaputra River north of Bahadurabad are from *Mahalanobis* [1927].

To calculate the recurrence interval of flood events we computed 1,000 bootstrapped draws with replacement of 30 years each from (i) the instrumental observations (1956-2011 C.E.), (ii) the reconstruction over the instrumental period (1956-2004 C.E.), (iii) the full reconstruction period (1309-2004 C.E.), (iv) CMIP5 RCP8.5 2050-2074 C.E. period runoff simulations, and (v) CMIP5 RCP8.5 2075-2099 C.E. period runoff simulations. For the draws from the reconstruction we used the median reconstruction, while for the CMIP5 data we included all 42 ensemble members of the 20-model suite to represent the full range of variability in the model simulations of discharge. In each draw, we calculated the percentile (P) of the 2007 C.E. JAS discharge of 48,800m^3/s. We then calculated the return interval as 100/(100-P), to give an estimate of the likelihood of the occurrence of high discharge related flood hazard in any given year. For example if in a random draw of 30 years, the 2007 C.E. flood year discharge placed in the 90th percentile, its return interval probability would be once every 100/(100-90)=10 years. However, if it placed in 80th percentile its return interval would be more frequent at once

every 100/(100-80)=5 years. An alternate approach to the bootstrap sampling we apply here could be to explicitly fit an extreme value distribution to the JAS discharge data.

Climate Models. We obtained the surface runoff parameter output in the spatial domain upstream of the Bahadurabad gauging station within the Brahmaputra watershed from a 20-model ensemble suite of phase five of the Coupled Model Intercomparison Project (CMIP5 ref. - [*Taylor et al.*, 2012]). This was done both for the 1850-2005 C.E. 'historical' simulation period, and 2006-2099 C.E. 'future' simulation period. For the future simulation period we used the representative concentration pathway 8.5 (RCP8.5) scenario that represents a net radiative imbalance of 8.5 W/m^2 in earth's radiative budget by the end of the twenty-first century [*Riahi et al.*, 2011]. Table B.2 lists all CMIP5 models and their respective ensemble members used. We only chose a model run where the same simulation scenario was available both for the historical and RCP8.5 simulation period, to be able to compare 'future' and 'historical' discharge against each other. As a preliminary check, we first tested that the standardized annual hydrographs of the instrumental discharge data and the CMIP5 runoff data matched reasonably well both over the 1956-1998 C.E. calibration period from the CMIP5 historical runs and the RCP8.5 2050-2099 C.E. future simulation period (Figure B.13). We did this to ensure that the models accurately capture seasonal runoff dynamics within the watershed, such as the wet JAS monsoon season period and the dry January through April winter period (Figure 2.2a). When comparing the variability across model members for the RCP8.5 2050-2099 C.E. simulation period to the instrumental data and the CMIP5 historical data, we found that it showed a large increase in runoff in the months of June through September. Before computing the annual runoff hydrograph using the CMIP5 models and all runoff projections, we bi-linearly interpolated all the CMIP5

runoff data into a common 0.25*0.25 grid, and lagged regions in the upper basin lying in an isochrone greater than 16 days [refs. - *Jian et al.*, 2009; *Webster et al.*, 2010] by one month to account for the temporal delay between surface runoff in the CMIP5 simulations in the upper part of the basin and the time it would take to reach the Bahadurabad gauging station located in the lower part of the basin (Figure B.14). Finally, to develop the CMIP5 estimates of historical and future discharge, we computed z-scores of each runoff simulation using its 1956-1998 C.E. mean and standard deviation, and then scaled these z-scores to discharge (in m^3/s) by using the 1956-1998 C.E. instrumental mean and standard deviation. This scaling to the 1956-1998 C.E. instrumental period allowed us to directly compare the reconstructions with the CMIP5 projections, and the magnitude of projected change into the 'future' compared to the 'historical' period and instrumental discharge.

Superposed Epoch Analysis (SEA). We tested the probability of the association between higher than normal discharge during flood years occurring by chance using a modified double bootstrap SEA [*Haurwitz and Brier*, 1981; *Rao et al.*, 2019]. To do this, we first calculated the variability in discharge based on 5^{th}, 50^{th}, and 95^{th} percentile of mean discharge across 1,000 unique draws of 10 flood years out of the total 16 between 1780-2004 C.E. We then determined the statistical significance of this response by comparing its probability distribution to that generated from 10,000 unique draws of 10 years at random ('pseudo-flood years') from the reconstruction between 1780 C.E. and 2004 C.E. We subtracted the five-year pre-event mean across both draws of the 'flood years' and 'pseudo-flood year' to reduce the impact of low-frequency variability on the overall composite mean response. We also conducted SEA using only the 12 pre-1956 C.E.

instrumental period in a similar fashion with reconstructed discharge. In this SEA we used 495 unique event year draws 8 of the 12 flood years due to the lower available sample size.

Chapter 3: European and Mediterranean hydroclimate responses to tropical volcanic forcing over the past millennium

This chapter is published as *Rao et al.* [2017], European and Mediterranean hydroclimate responses to tropical volcanic forcing over the last millennium, Geophys. Res. Lett., 44(10), 5104-5112.

Abstract

Volcanic eruptions can have global climate impacts, but their effect on the hydrologic cycle is poorly understood. We use a modified version of superposed epoch analysis, an eruption year list collated from multiple datasets, and seasonal paleoclimate reconstructions (soil moisture, precipitation, geopotential heights, and temperature) to investigate volcanic forcing of spring and summer hydroclimate over Europe and the Mediterranean over the last millennium. In the western Mediterranean, wet conditions occur in the eruption year and the following 3 years. Conversely, northwestern Europe and the British Isles experience dry conditions in response to volcanic eruptions, with the largest moisture deficits in post-eruption years 2 and 3. The precipitation response occurs primarily in late spring and early summer (April-July), a pattern that strongly resembles the negative phase of the East Atlantic Pattern. Modulated by this mode of climate variability, eruptions force significant, widespread, and heterogeneous hydroclimate responses across Europe and the Mediterranean.

3.1 Introduction

Large volcanic eruptions can inject sulfur dioxide into the stratosphere where it is converted into aerosolized sulfuric acid. These aerosols can persist in the stratosphere for several years, where they reflect and absorb incoming solar radiation, cooling global surface

temperatures but warming the stratosphere [*Robock*, 2000]. Volcanic eruptions are therefore useful events to study the response of Earth's climate system to short-term changes in radiative forcing. However, the temperature effects of volcanic forcing have received considerable attention [e.g. *Anchukaitis et al.*, 2012; *Anchukaitis et al.*, 2017; *D'Arrigo et al.*, 2009; *Luterbacher and Pfister*, 2015; *Meehl et al.*, 2004; *Stoffel et al.*, 2015a], and are relatively better constrained than the hydroclimate response [*Anchukaitis et al.*, 2010; *Broccoli et al.*, 2003; *Iles and Hegerl*, 2014].

Modeling and observational studies find a global decrease in precipitation in the immediate years following volcanic events [e.g. *Iles et al.*, 2013; *Joseph and Zeng*, 2011], although the regional and seasonal scale responses are more nuanced [*Anchukaitis et al.*, 2010; *Fischer et al.*, 2007b]. The decrease in global precipitation is likely caused by the reduction of incident shortwave radiation at the surface due to stratospheric volcanic aerosols, suppressing evaporation and leading to a cooler and more stable troposphere [*Iles and Hegerl*, 2014]. However, many of these studies focus on the past century when instrumental climate data are available, or are based on climate model outputs. In terms of global radiative forcing, there have only been two major volcanic eruptions during the past half-century, El Chichón in 1982, and Mt. Pinatubo in 1991, both of which coincided with El Niño events. Consequently, our understanding of the climate system's response to multiple eruptions over the past millennium is extremely limited.

Over Europe, the winter hydroclimate response to volcanic forcing resembles a positive phase of the North Atlantic Oscillation (NAO) [e.g. *Driscoll et al.*, 2012; *Shindell et al.*, 2004; *Zanchettin et al.*, 2013]. Less is known, however, about the effect of volcanic eruptions on spring and summer hydroclimate. The response may be further complicated by the influence of various

modes of climate variability on interannual and decadal timescales over Europe and the Mediterranean. These include the winter and spring NAO, the East Atlantic Pattern (EAP), the East-Atlantic-Scandinavian Pattern, the East-Atlantic West-Russia Pattern (EAWR) [*Barnston and Livezey*, 1987; *Schrier et al.*, 2006], and the summertime parallel of the winter NAO known as the summer NAO (SNAO) [*Folland et al.*, 2009].

Here, we investigate the spatiotemporal hydroclimate response to volcanic eruptions over Europe and the Mediterranean using a modified version of superposed epoch analysis (SEA), and test whether volcanism modulates spring and summer hydroclimate through variability in the aforementioned climatic modes. Our modified SEA generates multiple unique draws of key years and determines the volcanic response in a probabilistic framework, allowing us to present uncertainty estimates in this response. We expand on previous analyses [*Fischer et al.*, 2007b] using updated volcanic forcing data, and investigate the hydroclimate response in a new, longer (1100-2012 C.E.) hydroclimate reconstruction: the tree-ring based 'Old World Drought Atlas' or OWDA [*Cook et al.*, 2015b] that allows assessment of the response over a greatly expanded list of event years. Further, we extensively evaluate the seasonality of climatic anomalies and teleconnection forcings that may modulate this observed response [cf. *Büntgen et al.*, 2017; *Gao and Gao*, 2017]. We compare the OWDA response to a largely independent multi-proxy seasonal precipitation reconstruction (1500-2000 C.E.) [*Pauling et al.*, 2006] and a recent temperature reconstruction (755-2003 C.E.) [*Luterbacher et al.*, 2016].

3.2 Data and Methods

3.2.1 Data

Estimates of past hydroclimate variability over Europe and the Mediterranean are from the OWDA [*Cook et al.*, 2015b], a gridded tree-ring based reconstruction of mean June through August (JJA) self-calibrating Palmer Drought Severity Index [PDSI - *Palmer*, 1965; *Schrier et al.*, 2013]. Along with the OWDA we use a gridded multiproxy seasonal precipitation reconstruction for Europe [*Pauling et al.*, 2006], and a summer (JJA) European temperature reconstruction [*Luterbacher et al.*, 2016]. See Text C.1 [*Cook et al.*, 1999a; *Dai et al.*, 2004; *Fritts*, 1976; *George et al.*, 2010] for more details on the OWDA and *Pauling et al.* [2006] reconstructions. Other datasets used include, National Center for Atmospheric Research - National Center for Environmental Prediction (NCAR-NCEP) mean monthly sea level pressure (MSLP) [*Kalnay et al.*, 1996], gridded Climate Research Unit (CRU) TS 3.21 precipitation and temperature [*Harris et al.*, 2014b], and National Oceanic and Atmospheric Administration – Climate Prediction Centre (NOAA-CPC) NAO, EAP, and EAWR indices. To develop a 'key year list' of volcanic eruptions we compile data from five volcanic event lists (Table C.1), generated by analyzing sulfate loading in bipolar ice cores [*Crowley and Unterman*, 2013; *Gao et al.*, 2008; *Plummer et al.*, 2012; *Sigl et al.*, 2013; *Sigl et al.*, 2015].

3.2.2 Analysis

To facilitate the interpretation of volcanically forced hydroclimate anomalies, we first examine the seasonality of climate signals integrated by the OWDA, along with the relationship between regional precipitation and temperature. We do this by calculating the spatial field correlation between the OWDA and gridded climate data (CRU precipitation and temperature),

and the spatial field correlation between the two gridded climate datasets themselves (see Text C.1). Next, we use SEA to determine the statistical significance of volcanically forced climatic anomalies [e.g. *Adams et al.*, 2003; *Anchukaitis et al.*, 2010; *Fischer et al.*, 2007b]. The SEA is a statistical method to identify consistent responses to events, by testing for the possibility of random occurrence [*Haurwitz and Brier*, 1981]. One assumption of the SEA however is that the 'key year list' (volcanic event years in our case) is accurate [*Zanchettin et al.*, 2013], when in fact there are uncertainties associated with estimates of volcanic event years from ice-core evidence [*Baillie*, 2008; *Plummer et al.*, 2012; *Sigl et al.*, 2015]. Additionally, conventional SEA does not provide response uncertainty estimates based on the choice of key years.

We estimate the volcanic response using (n_1=1000) unique subsets of eruption years from the 'key year list' in Table C.1. Each subset is the mean response of n_2=10 key years. Next, we determine the median, 10th and 90th percentile of these (n_1=1000) mean responses on a grid cell basis, providing an estimate of the sensitivity of the observed response to the choice of key event years, and the widest possible uncertainty estimate based on this choice. For each of the 10 years in the 1000 draws of non-repeating subsets, we study the fifteen-year delayed post-eruption anomalies with respect to pre-eruption climatology, defined as the mean state over the five-year period preceding the eruption. The short reference period minimizes the effect of mean background low-frequency climate variability. Since it is likely that some of the 'key years' in Table C.1 correspond to the same event (e.g. 1168-69; 1229-30; 1257-58; 1344-45; 1458-59; 1600-01; 1694-95; 1815-16), only key years separated by more than five years were included in each draw.

We determine the statistical significance of the PDSI, precipitation, and temperature response using SEA by bootstrapped resampling [*Haurwitz and Brier*, 1981].This is done by

comparing the post-eruption response to the likelihood of random occurrence, by generating (n_3=10000) sequences of (n_2=10) 'pseudo-key year' samples treated in the same fashion as the actual volcanic key years, including checking that key years chosen in sequences are separated by more than five years. We consider epochal anomalies to be significant if the 'actual response' either falls below the 5th percentile or is greater than the 95th percentile (i.e. one-sided epochal anomaly at $p<0.05$).

To evaluate whether volcanically forced hydroclimate observed in the SEA analysis could be modulated though teleconnection patterns (e.g. NAO, EAP, SNAO, EAWR etc.), we calculate spatial field correlations between these teleconnection patterns and both CRU instrumental precipitation and OWDA PDSI. All temporal correlations are calculated on linearly detrended data and significance is calculated after adjusting the sample size for temporal first order auto-correlation [*Bretherton et al.*, 1999].

Based on the results of these preliminary analyses (not shown), we present the spatial field correlation between mean April through July (AMJJ) EAP and MSLP over Europe between 1950 and 2012. We then compute the pattern correlation between the SEA response to volcanic forcing and PDSI anomalies forced by the EAP. We adjust the sample size (n=5414 grid cells) used to estimate significance using a 5x5 Gaussian kernel weighting matrix (σ=1) to account for spatial autocorrelation in the PDSI and precipitation fields [*Cliff and Ord*, 1981]. Finally, we develop an estimate of EAP variability for the period 1766-1949, prior to the availability of the reanalysis data, using rotated principal components analysis (RPCA) [*Barnston and Livezey*, 1987] on a reconstruction of 500hPa geopotential heights (GPH) developed by *Casty et al.* [2007] [see Text C2 for details; *Raible et al.*, 2014]. We use this estimated EAP series to

examine the post-eruptive EAP response following the large nineteenth century volcanic eruptions.

3.3 Results

Over the 1901-1978 period, JJA PDSI correlates significantly ($p<0.05$, two-sided Student's t-test) with both concurrent and antecedent precipitation and temperature (Figure 3.1; C.1). Precipitation is positively and significantly correlated with JJA PDSI in all seasons over much of the domain, with JJA precipitation showing the strongest signal. Correlations over the Mediterranean are most significant during spring (March through May - MAM), the main season of moisture supply relevant to tree growth in this region (Figure C.2). Over the Mediterranean, this relationship is leveraged primarily by May precipitation; while over northwestern Europe the JJA signal is predominantly a reflection of June and July precipitation (not shown). Temperature is negatively correlated with PDSI, especially during JJA (Figure 3.1 – center panels), reflecting either the direct impact of temperature on PDSI (i.e., higher temperatures translate to increased evapotranspiration and lower soil moisture), or the strong inverse correlation during JJA between temperature and precipitation (or soil moisture) over much of the region [Figure 3.1 & C.1 - right panels; *Casty et al.*, 2007; *Fischer et al.*, 2007a; *Seneviratne et al.*, 2006].

In the immediate years following an eruption, the median bootstrap hydroclimate response in the OWDA is widespread and significant ($p<0.05$, one-tailed epochal anomaly) (Figure 3.2). In the western Mediterranean, pluvial anomalies peak during the event year (year t+0) and one year after (year t+1), but persist up to three years post eruption (year t+3) (Figure 3.3a). Conversely, a large and somewhat delayed drying signal emerges over northwestern Europe and the British Isles, peaking two to three years post-eruption (years t+2 and t+3) (Figure

3.3b). These results are further supported by analysis of the 10th percentile response over the western Mediterranean, and the 90th percentile response over northwestern Europe (Figure 3.3; Figure C.3). Thus, even the driest years post-eruption over the western Mediterranean are relatively wet, and the wettest years post-eruption over northwestern Europe are relatively dry, compared to pre-eruption values. While persistent positive PDSI anomalies are observed over northern Fennoscandia in years t+1 through t+3 (Figure 3.2), this response may be a combination of wetting and post-eruption cooling, as the OWDA also shows strong summer temperature sensitivity over Fennoscandia (Figure 3.1).

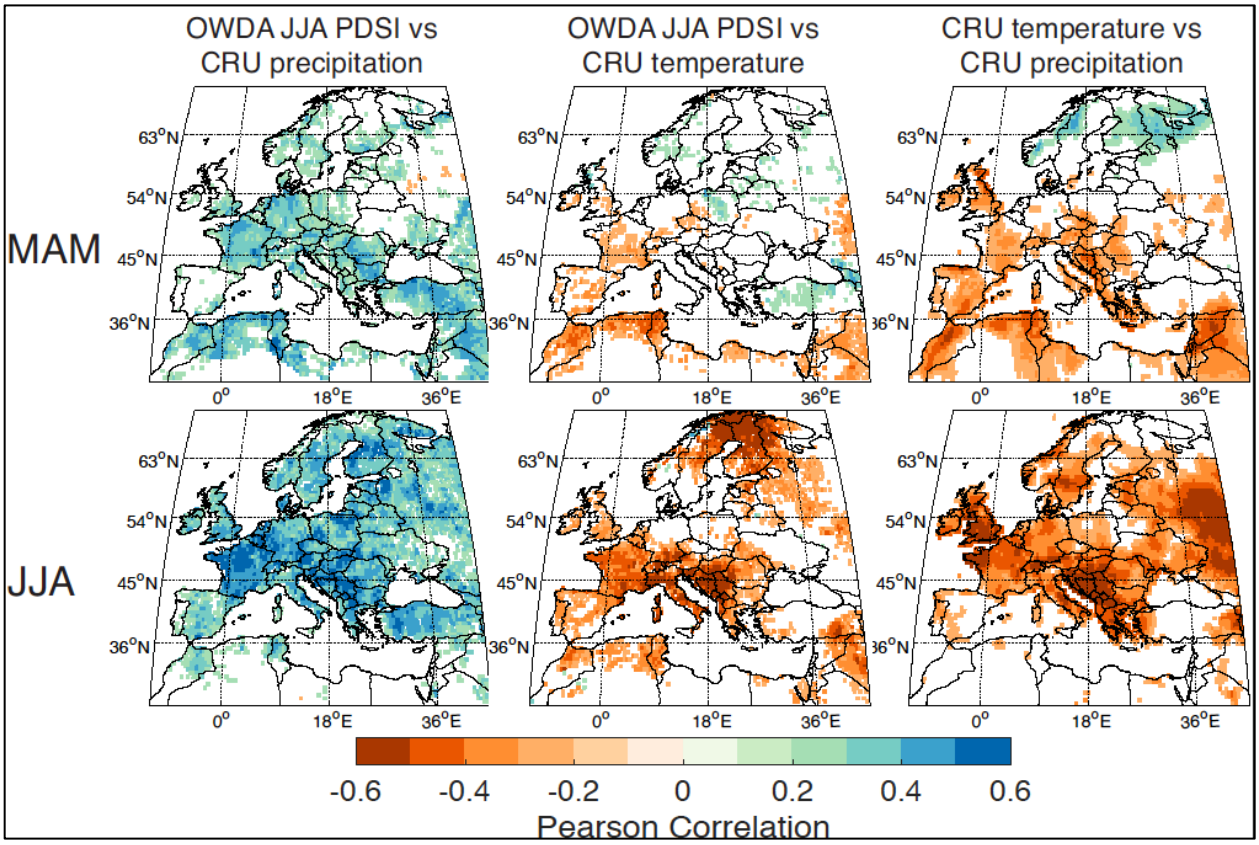

Figure 3.1 Pearson correlation between (left panel) JJA OWDA PDSI and CRU precipitation, (center panel) JJA OWDA PDSI and CRU temperature, and (right panel) CRU precipitation and CRU temperature between 1901-1978. Only correlations significant at p<0.05 (two-sided Student's t-test) shown. Top panel March-May (MAM), lower panel June-August (JJA).

The median response to volcanic forcing in MAM precipitation [*Pauling et al.*, 2006] shows significant wetting ($p<0.05$, one-tailed epochal anomaly) over the western Mediterranean two years (year t+2) following an eruption (Figure C.4). Over northwestern Europe and the British Isles a significant ($p<0.05$, one-tailed epochal anomaly) reduction in summer JJA precipitation is observed three and four years (years t+3 and t+4) after an eruption [Figure C.5; *Fischer et al.*, 2007b]. Following an eruption, summer JJA temperatures show significant cooling across the entire region, as documented previously [Figure C.6; *Luterbacher et al.*, 2016].

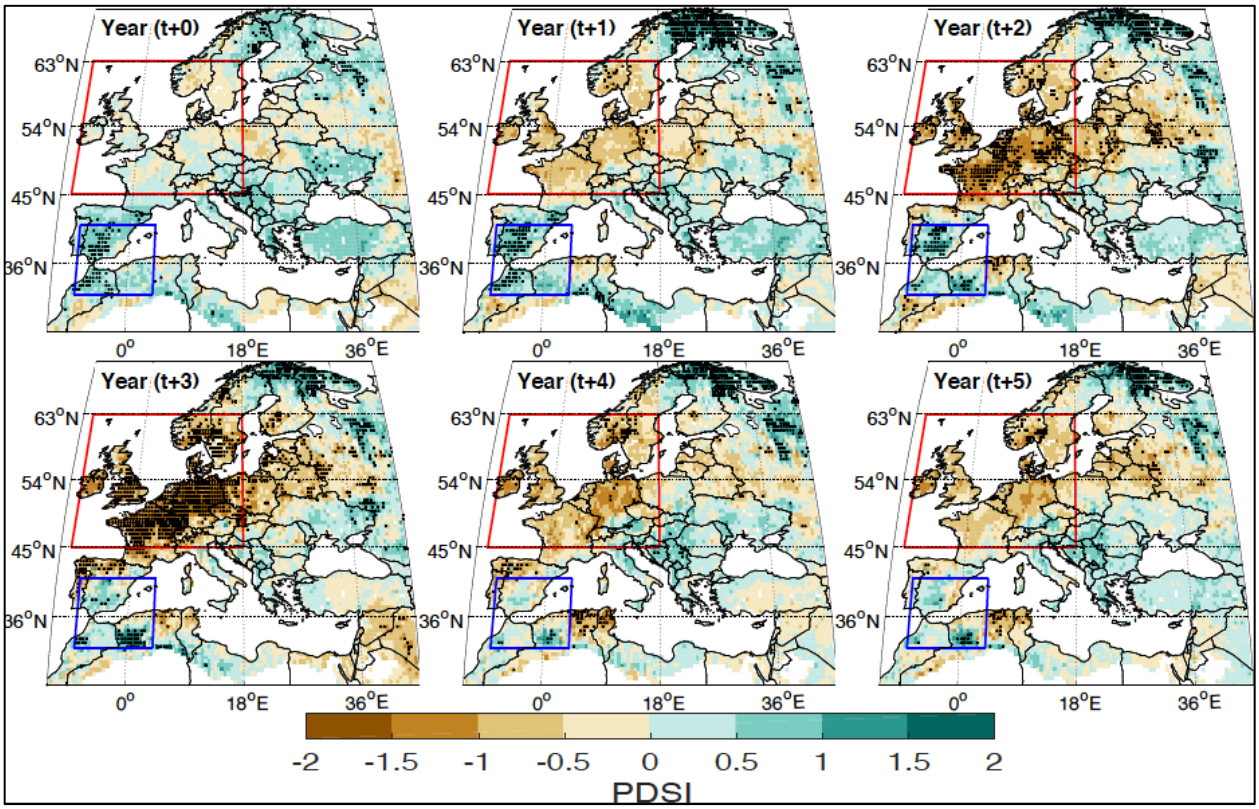

Figure 3.2 Superposed epoch analysis (SEA) showing OWDA JJA PDSI response to volcanic forcing for years t+0 through t+5 between 1100-2012 C.E. Response is the median value for each grid cell. Stipples indicate statistically significant ($p<0.05$, one-tailed) epochal anomalies.

The EAP is a prominent mode of climate variability over the North Atlantic second to the NAO. It appears as a leading mode through the year and is characterized by a northwest-

southeast dipole of pressure centers [*Barnston and Livezey*, 1987; *Schrier et al.*, 2006]. It is positively correlated with precipitation over northwestern Europe, the British Isles and southern Fennoscandia in MAM and JJA, and inversely correlated with MAM precipitation in the western Mediterranean and JJA precipitation over southern Iberia (Figure 3.4 – left panel). In MAM, a positive EAP is linked to lower than normal MSLP along the European Atlantic sector, and anomalously high MSLP around the Mediterranean basin, that suppresses precipitation in the region (Figure 3.4 – right panel). During a positive EAP the low pressure centered near Scotland intensifies during JJA.

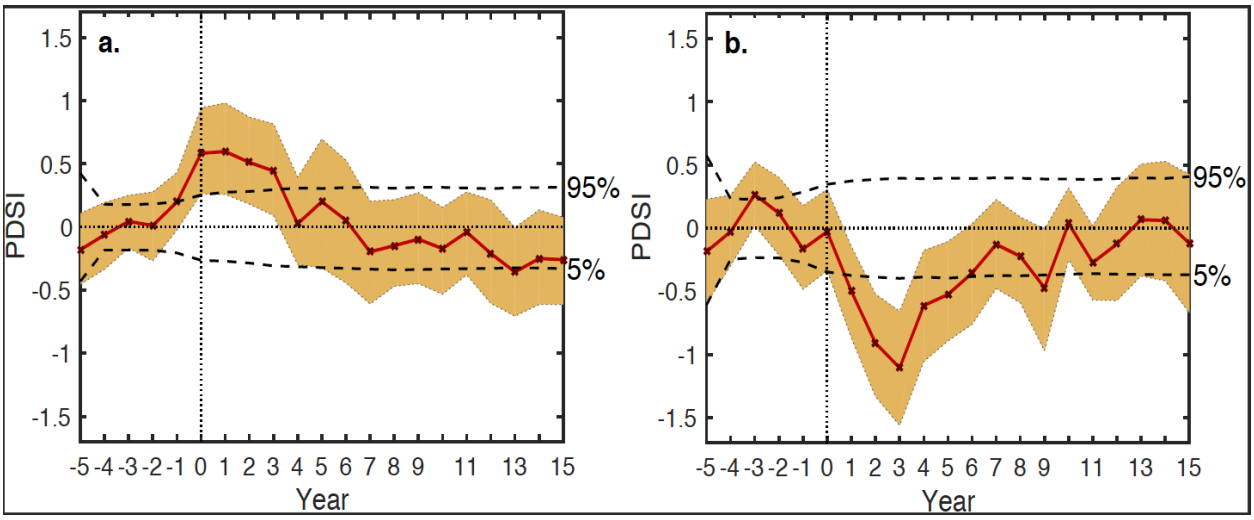

Figure 3.3 SEA showing area-weighted mean PDSI response over (a.) western Mediterranean (blue box - Figure 2) and (b.) northwestern Europe (red box - Figure 2). Uncertainty intervals are 10th and 90th percentile of the response. Dashed horizontal line indicates threshold required for statistically significant ($p<0.05$, one-tailed) epochal anomalies.

The spatial correlation between the mean AMJJ EAP index and JJA OWDA PDSI between 1950 and 1978 is shown in Figure 3.5a. A positive phase of the EAP corresponds to wet conditions over northwestern Europe and the British Isles, and dry conditions over the western Mediterranean basin. Drying is strongest over southern Iberia, northern Morocco, and northern Algeria. The spatial pattern of PDSI conditions following volcanic eruptions (Figure 3.2)

strongly resembles a negative phase of the EAP, especially in post-eruption years t+1, 2 and 3, suggesting that volcanic forcing may modulate spring and summer climate over Europe by stimulating a negative EAP-like atmospheric response. The Pearson correlations between the years t+1, 2 and 3 response (Figure 3.2) with the EAP-OWDA pattern are r=-0.47, -0.44, and -0.52 respectively (p=0, N'=686; p=0, N'=589; and p=0, N'=581 respectively, 2-sided Student's t-test, N' - sample size adjusted for spatial autocorrelation). Other teleconnection patterns such as the NAO, SNAO, and the EAWR were tested for their influence on hydroclimate over Europe and were not found to force hydroclimate responses spatially similar to that observed following volcanic eruptions.

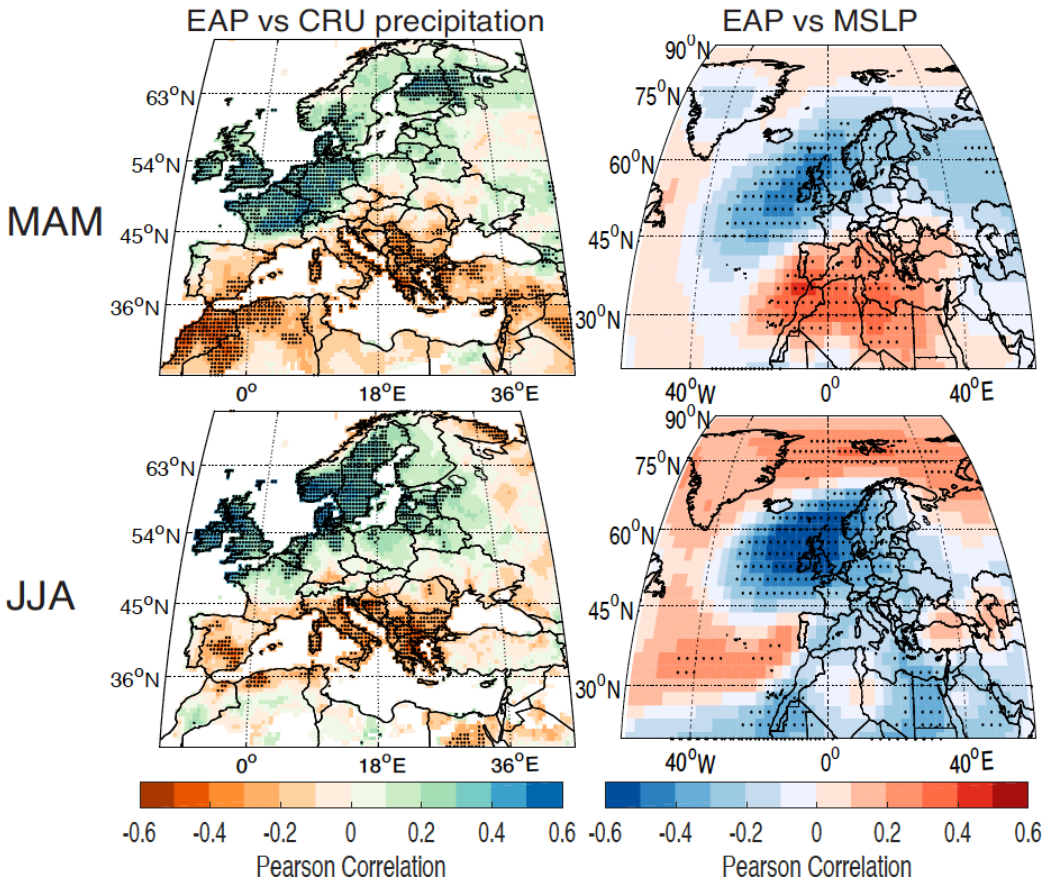

Figure 3.4 Correlation between East Atlantic Pattern (EAP) and (left) CRU precipitation (right) NCAR-NCEP mean sea level pressure (MSLP) for (upper panel) MAM, and (lower panel) JJA between 1950 and 2012. Stippling indicates significant correlation ($p<0.05$, 2-sided, Student's t-test). Note different colorbars.

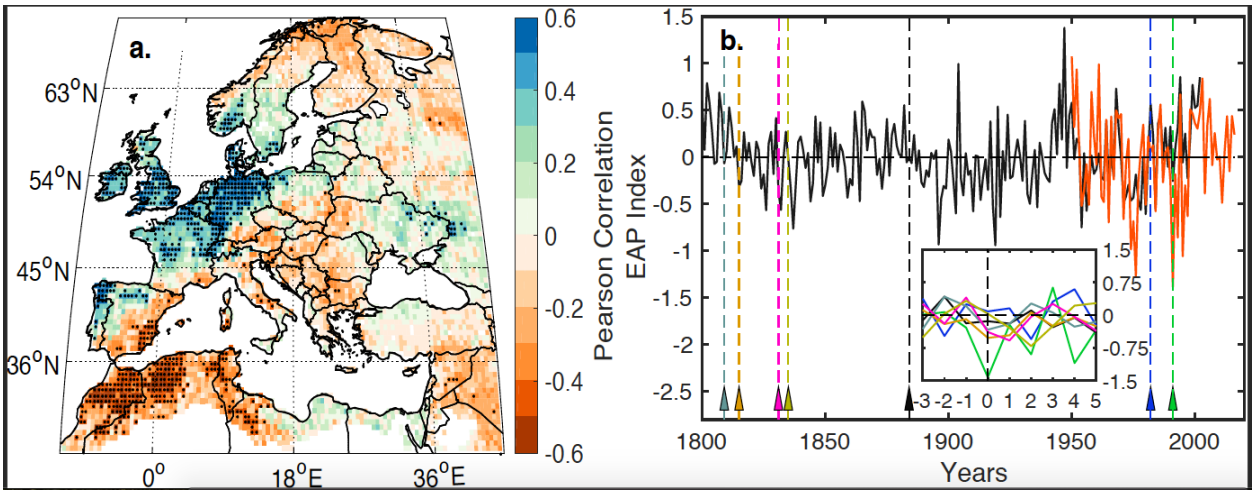

Figure 3.5 EAP and European hydroclimate. (a.) Correlation between April-July (AMJJ) NOAA-CPC EAP index and OWDA JJA PDSI between 1950-1978. Stippled blue (red) shading indicates significant positive (negative) correlation (p<0.05, 2-sided Student' t-test). (b.) AMJJ NOAA-CPC EAP index between 1950-2016 (red) and estimated from *Casty et al.* [2007] 500 hPa reconstruction (black - see Text S2). Inset shows five-year post-eruptive AMJJ EAP response after 1809 (grey), 1815 (yellow), 1831 (pink), 1835 (olive), 1884 (black), 1982 (blue), and 1991 (green) after subtracting five-year pre-event mean.

The NOAA-CPC AMJJ EAP timeseries between 1950-2016 (in red) and the estimated AMJJ EAP between 1800-2002 using the *Casty et al.* [2007] 500 hPa GPH reconstruction (in black) are shown in Figure 3.5b. The two series are significantly correlated during the period of overlap between 1950-2002 (r=0.71, p=0.0001, N=53, N'=50 (for temporal autocorrelation), 2-sided Student's t-test). The inset shows the post-eruption AMJJ EAP response after El Chichón in 1982 (blue line) and Mt. Pinatubo in 1991 (green line) after subtracting the five-year pre-event NOAA-CPC mean EAP index, and estimated EAP response following the unknown event in 1809 (grey line), Tambora in 1815 (yellow line), Babuyan – 1831 (pink), Cosiguina – 1835 (olive), and Krakatau in 1884 (based on radiative forcing - black line) after subtracting the five year pre-event estimated EAP index. While variability in post-eruption EAP and estimated EAP response is high, there is a clustering of negative values at year t+0, and in four out of five cases in year t+1 and t+2. It should be noted however, that the response after El Chichón is mostly positive.

3.4 Discussion

While post-volcanic spring and summer cooling is a consistent response both regionally [Figure C.5; *Esper et al.*, 2013a; *Luterbacher et al.*, 2016] and globally [*D'Arrigo et al.*, 2009; *Stoffel et al.*, 2015a], here we show that the hydroclimate response to volcanic forcing is much more spatially heterogeneous [e.g. *Anchukaitis et al.*, 2010]. Post-eruption hydroclimate anomalies (Figure 3.2) over Europe and the Mediterranean resemble those caused by a negative phase of the EAP (Figure 3.4 & 3.5a), with pluvial conditions over the western Mediterranean and drought conditions over northwestern Europe and the British Isles [Figure 3.2; Figure 3.3; also see *Büntgen et al.*, 2017; *Gao and Gao*, 2017]. A similar response is observed in a largely independent seasonal precipitation reconstruction [Figure C.4 & C.5; *Fischer et al.*, 2007b], and also simulated, albeit with slightly northward displaced anomalies, in volcanically forced mean May through September precipitation by the Community Earth System Model [Figure 4 in *Colose et al.*, 2016].

The hydroclimate system has a high degree of internal spatiotemporal variability. At the same time, there are also uncertainties in the volcanic eruption years themselves [*Baillie*, 2008; *Plummer et al.*, 2012; *Sigl et al.*, 2015]. To account for this uncertainty, we use a novel form of the SEA with non-repeating subsets of eruption years from a larger key year list (Table C.1). Thus, we are able to examine the degree of variability in the hydroclimate system based on different choices of key event years (Figure 3.3 & C.3), and incorporate this uncertainty into our results.

Our analyses suggest that volcanic impacts on spring-summer European hydroclimate are likely modulated by predisposing the EAP towards its negative phase [*Zanchettin et al.*, 2012]. While the mechanisms for this are still uncertain, one possibility examined in model simulations

suggests its causes may originate in the tropics. Following an eruption, a reduction in shortwave radiation at the surface causes faster cooling over land compared to oceans due to the former's lower heat capacity. This reduces the land-sea thermal contrast, weakening monsoon circulations including the west African monsoon [*Joseph and Zeng*, 2011]. In turn, the weakened monsoonal precipitation and equatorial convergence reduces latent heat fluxes in the free troposphere and leads to weakening of Hadley and Ferrel cell circulations [*Rind et al.*, 1992]. Using the ECHAM 5.4 model Wegmann et al. [2014] found that weakening these circulations weakened the meridional pressure gradient in the North Atlantic, causing southward shifted storm tracks and anomalous uplift over the Mediterranean that increased convection and precipitation over the Mediterranean. Our findings (Figure 2-5) suggest that the hydroclimate response to volcanic forcing is consistent with this hypothesized weakening of the descending branch of the Hadley circulation and southward shift of storm tracks, causing springtime wetting over the western Mediterranean and spring and summer drying over northwestern Europe. Although this mechanism is largely consistent with that proposed by *Gao and Gao* [2017], we show that the OWDA primarily reflects spring through summer soil moisture (Figure 3.1 & C.1). Thus, it is unlikely that volcanically induced wintertime teleconnection anomalies, such as a positive winter NAO play a dominant role in influencing the observed response. Based on these dynamics and the resemblance between hydroclimate anomalies induced by volcanic eruptions (Figure 3.2) and those triggered by the EAP (Figure 3.4 and 3.5), this theory offers at least a plausible physical

mechanism for volcanic forcing of spring-summer hydroclimate over Europe and the Mediterranean by inducing a negative phase of the EAP.

5 Conclusions

We used a new millennium-length tree-ring based hydroclimate reconstruction with an expanded event year list and a novel modification to SEA, to demonstrate a robust but spatially complex response of European and Mediterranean hydroclimate to volcanic eruptions. The forced hydroclimate response appears to be triggered by a negative phase of the EAP which causes anomalous spring uplift over the western Mediterranean, southward shifted storm tracks, and a weakened spring-summer meridional pressure gradient over the North Atlantic. Consequently, we observe wetting over the western Mediterranean and drying over northwestern Europe following volcanic eruptions. However, the exact dynamical mechanisms by which volcanic eruptions trigger this response (e.g., possibly by weakening equatorial convergence and the west African monsoon) still need to be better understood. These results highlight the complexity of hydroclimate response to eruptions, and suggest the need to consider carefully how aerosol forcing (e.g. from volcanoes, pollution, or geoengineering) may modulate hydroclimate in the future.

Acknowledgments and Data

We thank Doug Martinson (LDEO), participants at the Volcanoes Impact on Climate and Society workshop, and one anonymous reviewer for feedback that improved our study. We declare no conflicts of interest. Support for BIC - NASA Modeling, Analysis, and Prediction program; ERC - NOAA Climate Change Data and Detection Program NA10OAR4310123; ERC and RDD -

NSF AGS 15-02224; BMB - AGS 12-03818, AGS 13-03976, and LDEO Climate Center and Climate and Life initiatives. Lamont contribution #8099.

Datasets: *Cook et al.* [2015] https://www.ncdc.noaa.gov/cdo/f?p=519:1:0:::P1_study_id:19419; *Pauling et al. [2006]* ftp://ftp.ncdc.noaa.gov/pub/data/paleo/historical/europe/pauling2006precip/; *Luterbacher et al.* [2016] https://www.ncdc.noaa.gov/cdo/f?p=519:1:0::::P1_STUDY_ID:19600; NCAR-NCEP MSLP http://iridl.ldeo.columbia.edu/SOURCES/.NOAA/.NCEP-NCAR/.CDAS-1/.MONTHLY/.Intrinsic/.MSL/.pressure/%28mb%29unitconvert/index.html; *Harris et al.* [2014] CRU TS 3.21 http://catalogue.ceda.ac.uk/uuid/3f8944800cc48e1cbc29a5ee12d8542d; teleconnection data including EAP index http://www.cpc.ncep.noaa.gov/data/teledoc/telecontents.shtml; and *Casty et al.* [2007] 500 hPa GPH reconstruction ftp://ftp.ncdc.noaa.gov/pub/data/paleo/historical/europe/casty2007/

Chapter 4: A double bootstrap approach to Superposed Epoch Analysis to evaluate response uncertainty

This chapter is published as *Rao et al.* [2019], A double bootstrap approach to Superposed Epoch Analysis to evaluate response uncertainty, *Dendrochronologia*, *55*, 119-124.

Abstract

The association between climate variability and episodic events, such as the antecedent moisture conditions prior to wildfire or the cooling following volcanic eruptions, is commonly assessed using Superposed Epoch Analysis (SEA). In SEA the epochal response is typically calculated as the average climate conditions prior to and following all event years or their deviation from climatology. However, the magnitude and significance of the inferred climate association may be sensitive to the selection or omission of individual key years, potentially resulting in a biased assessment of the relationship between these events and climate. Here we describe and test a modified double-bootstrap SEA that generates multiple unique draws of the key years and evaluates the sign, magnitude, and significance of event-climate relationships within a probabilistic framework. This multiple resampling helps quantify multiple uncertainties inherent in conventional applications of SEA within dendrochronology and paleoclimatology. We demonstrate our modified SEA by evaluating the volcanic cooling signal in a Northern Hemisphere tree-ring temperature reconstruction and the link between drought and wildfire events in the western United States. Finally, we make our Matlab and R code available to be adapted for future SEA applications.

4.1 Introduction

Superposed Epoch Analysis (SEA) is a statistical method used to identify the link between discrete events and continuous time or spatiotemporal processes and test the probability of such an association occurring by chance [*Haurwitz and Brier*, 1981]. SEA has been widely applied in climatology and dendroclimatology to test for the impact of volcanic eruptions on climate [e.g. *Esper et al.*, 2013b; *Kelly and Sear*, 1984; *Kelly et al.*, 1996; *Lough and Fritts*, 1987; *Taylor et al.*, 1980; *Trouet et al.*, 2018], the significance of soil moisture and climate conditions (e.g. ENSO, PDO) on the occurrence of forest fires [e.g. *Baisan and Swetnam*, 1990; *Gedalof et al.*, 2005; *Hessl et al.*, 2004; *Schoennagel et al.*, 2005; *Swetnam*, 1993; *Swetnam and Betancourt*, 1998; *Swetnam et al.*, 2016], and to evaluate tree growth response to drought events [e.g. *Lévesque et al.*, 2014; *Martín-Benito et al.*, 2008; *Orwig and Abrams*, 1997; *Woodhouse*, 1993] and insect defoliation [*Flower et al.*, 2014; *Nola et al.*, 2006; *Pohl et al.*, 2006].

SEA requires two independent datasets. The first is an 'event list'. These 'events' are usually discrete in time, such as years of volcanic eruptions or the precisely dated years of fire-scars in the annual rings of trees. The second variable is usually a long, continuous, and evenly sampled timeseries (e.g. climate observations or paleoclimate reconstructions). The underlying hypothesis of SEA is that the 'events' either cause or are themselves a response to the characteristics of the continuous timeseries, and that the identification of the sign, magnitude, and timing of that response may be optimised by averaging across all events. To evaluate this, first, a 'composite matrix' is made by drawing fixed windows of consecutive observations from the continuous timeseries that span years before, during, and after the event. The mean of this composite matrix, or its deviation from climatology is then calculated as the epochal response. Finally, the statistical significance of this response is determined using randomisation schemes to

evaluate the result against a null hypothesis to determine how likely the observed response would have occurred by chance [*Haurwitz and Brier*, 1981]. The compositing and averaging process serves as a filter that enhances the high-frequency response signal of interest while minimising noise [*D'Arrigo et al.*, 1993]. This technique also accounts for long-term drift, or low frequency variability that may be present. For example, using SEA one can infer that volcanic eruptions cause widespread northern hemisphere cooling [e.g. *Anchukaitis et al.*, 2017; *Briffa et al.*, 1998; *Sear et al.*, 1987; *Stoffel et al.*, 2015b], or that fire-events are associated with anomalously dry soil moisture conditions [e.g. *Hessl et al.*, 2016; *Kipfmueller et al.*, 2017].

Within the SEA literature the two commonly used randomisation schemes to determine response significance are 'random bootstrapping' [*Haurwitz and Brier*, 1981] and 'block reshuffling' [*Adams et al.*, 2003]. While both rely on Monte Carlo type bootstrapping approaches to determine confidence interval thresholds, they test for different hypotheses [*Anchukaitis et al.*, 2010]. The random bootstrap takes multiple random draws from the entire 'event' timeseries by generating 'pseudo key years', and then computes statistics of random variability within the 'response' dataset to determine significance thresholds. The block reshuffling method on the other hand creates random surrogate composite matrices by first permuting the original 'event' composite matrix, and then computing distributions based on this random shuffling of the 'response' anomalies for each event series [*Wanliss et al.*, 2018]. Prior to the reshuffling, the serial autocorrelation of the 'response' timeseries is used to determine the block length sampled, helping preserve the data's autocorrelation structure. By resampling in blocks, exclusively within the composite matrix, the statistics and autocorrelation of the composite matrix are preserved while destroying preferred pre and post-event temporal ordering, ensuring that the resulting

confidence intervals take into account the confounding influence of temporal structure in the time series [*Adams et al.*, 2003].

While the compositing and averaging process in SEA serves as a high-frequency filter to increase the signal-to-noise ratio of the mean epochal response, it has multiple drawbacks. The first is that one or more events might have an outsized leverage on the mean response value across epochs [*Adams et al.*, 2003]. The second relates to noise added to the SEA results due to dating uncertainty in the events [*Sigl et al.*, 2015; *Toohey and Sigl*, 2017] or the timeseries, along with the potential lack of temporal resolution in the proxy to resolve the seasonality of the event or the response. The dating uncertainty means that there might be an offset between the event response (e.g. as post-volcanic winter warming [*Zambri et al.*, 2017]) and what is recorded in the seasonal climate proxies like as tree-rings and corals. Another source of uncertainty in SEA is the a priori subjective definition of what constitutes an event and the effect this choice has on the SEA response. For example, the threshold to use to define a volcanic event (e.g. radiative forcing larger than Pinatubo, Tambora, etc.), or the percentage cut-off used to define fire events (e.g. 10% scarred trees, 20% scarred trees etc.) tend to be subjective choices. Finally, the simple averaging of the response matrix in conventional SEA relies on the implicit hypothesis that all event signals are equal when in reality each event (e.g. volcanic eruption, fire year) is unique. Additionally, even the response to the same kind of event might differ due to natural variability within the climate system modulated by pre-event background states [*Esper et al.*, 2013b; *Zanchettin et al.*, 2019].

Here in this study we describe a modified double-bootstrap SEA framework that first generates multiple unique draws of the key year list itself. We first used this method in *Rao et al.* [2017] to evaluate the impact of volcanic eruptions on post-volcanic hydroclimate over Europe

and North Africa. This double-bootstrap SEA methodology describes the event response in a probabilistic framework and therefore explicitly and quantitatively addresses the uncertainties in SEA mentioned above.

4.2 Data

We test our modified SEA method using two datasets. The first is a recent tree ring reconstruction of Northern Hemisphere May-though-August mean temperature spanning 750-2011 C.E. [N-TREND -*Wilson et al.*, 2016]. The second is a compilation of annually resolved tree ring based fire scar records from the western United States [*Trouet et al.*, 2010]. The original authors of both papers and datasets also conducted SEA analysis, demonstrating that Northern Hemisphere temperatures cool in the years immediately following large tropical volcanic eruptions [*Wilson et al.*, 2016], and wildfire years in the western US coincide with drought years [*Trouet et al.*, 2010]. Hence, we focus on the implementation of our SEA method and do not seek to reinterpret the physical mechanisms behind the event signals.

The tropical eruption key years used to evaluate the N-TREND temperature reconstruction response to volcanism come from the eVolv2k database [*Toohey and Sigl*, 2017]. We chose a total of 20 tropical eruptions, between 30°S-30°N and 1100-2011 C.E. that have a peak northern hemisphere aerosol optical depth (AOD) greater than 0.08 as eruption key years (Table 4.1). Figure 4.1 shows the N-TREND temperature reconstruction between 1100-2011 C.E. along with markers for these volcanic eruptions. For reference, we also include markers for 9 northern hemisphere extratropical volcanic eruptions between 30°N-90°N (Table 4.1) with northern hemisphere AOD > 0.08 from *Toohey and Sigl* [2017]. Following *Trouet et al.* [2010], we categorised a year as a fire-year when at least 10 percent of samples are scarred in a minimum of two trees, resulting in a total of 98 candidate fire key years between 1342-1952 C.E.

Table 4.1 Tropical volcanic eruptions key years used for Superposed Epoch Analysis (SEA) and Northern Hemisphere marker years highlighted in Figure 1. Dates are derived from *Toohey and Sigl* [2017]. Names are mentioned only for identified eruptions.

Tropical volcanic eruptions	Northern Hemisphere Extratropical eruptions
1107	1182
1170	1200
1229	1210
1257 Rinjani, Samalas, Indonesia	1329
1285	1477 Bárðarbunga, Veiðivötn, Veidivatnahraun, Iceland
1344	1667 Shikotsu, Tarumai, Japan
1452	1729
1457	1783 Grimsvötn, Lakagígar, Laki, Iceland
1585 Colima, Mexico	1912 Novarupta, Katmai, Alaska, USA
1600 Huaynaputina, Peru	
1694	
1640 Parker, Philippines	
1808	
1815 Tambora, Indonesia	
1831 Babuyan Claro, Philippines	
1835 Cosigüina, Nicaragua	
1883 Krakatau, Indonesia	
1902 Santa Maria, Guatemala	
1982 El Chichón, Mexico	
1991 Pinatubo, Philippines	

The record for the western US used to evaluate drought conditions during fire-event epochs comes from an area-weighted spatial average of the Living Blended Drought Atlas (LBDA) [*Cook et al.*, 2004; *Cook et al.*, 2010b] between 124°W to 109°W and 35°N to 50°N, covering all four regional composite fire scar series used in *Trouet et al.* [2010]. The LBDA is a gridded spatial reconstruction of mean June through August (JJA) Palmer Drought Severity Index (PDSI - [*Palmer*, 1965]. Figure 4.2a shows the percentage of all the western US sites within the *Trouet et al.* [2010] dataset that records a fire for each year between 1300-2000 C.E. along with the total number of sites. The lower panel Figure 4.2b is a timeseries of the area-

weighted PDSI for the western US, with negative and positive values indicating dry and wet conditions respectively.

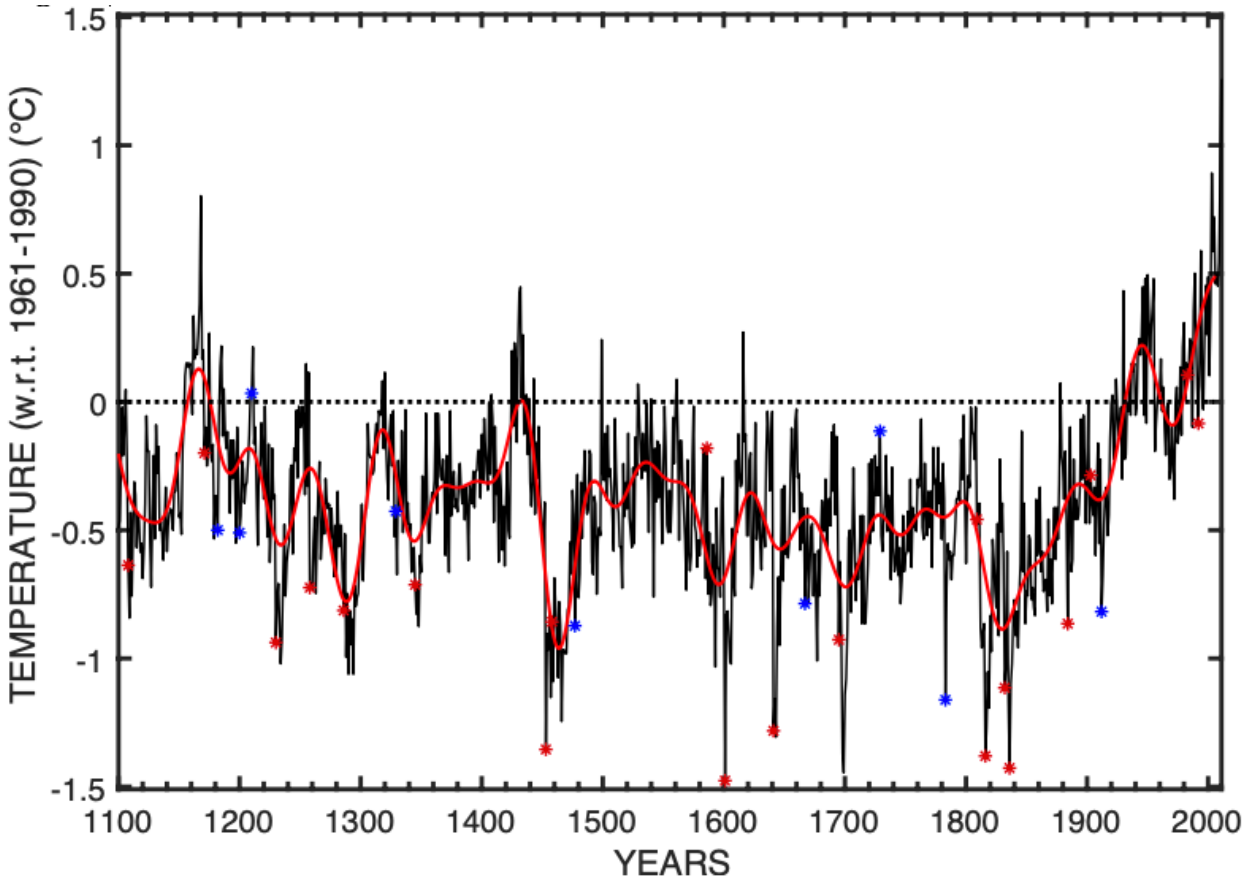

Figure 4.1 A temporal subset of the Northern Hemisphere May-August summer temperature reconstruction between 1100-2011 C.E. from *Wilson et al.* [2016]. Red * symbols indicate tropical volcanic eruption key years (see Data) used in our Superposed Epoch Analysis (SEA) to evaluate the Northern Hemisphere summer temperature response to volcanism. Blue * symbols indicate large extratropical Northern Hemisphere eruptions. Tropical volcanic key years are shifted by +1 years to better align with the cooling response (see Results). Y-axis is the anomaly in °C with respect to temperatures between 1961-1990.

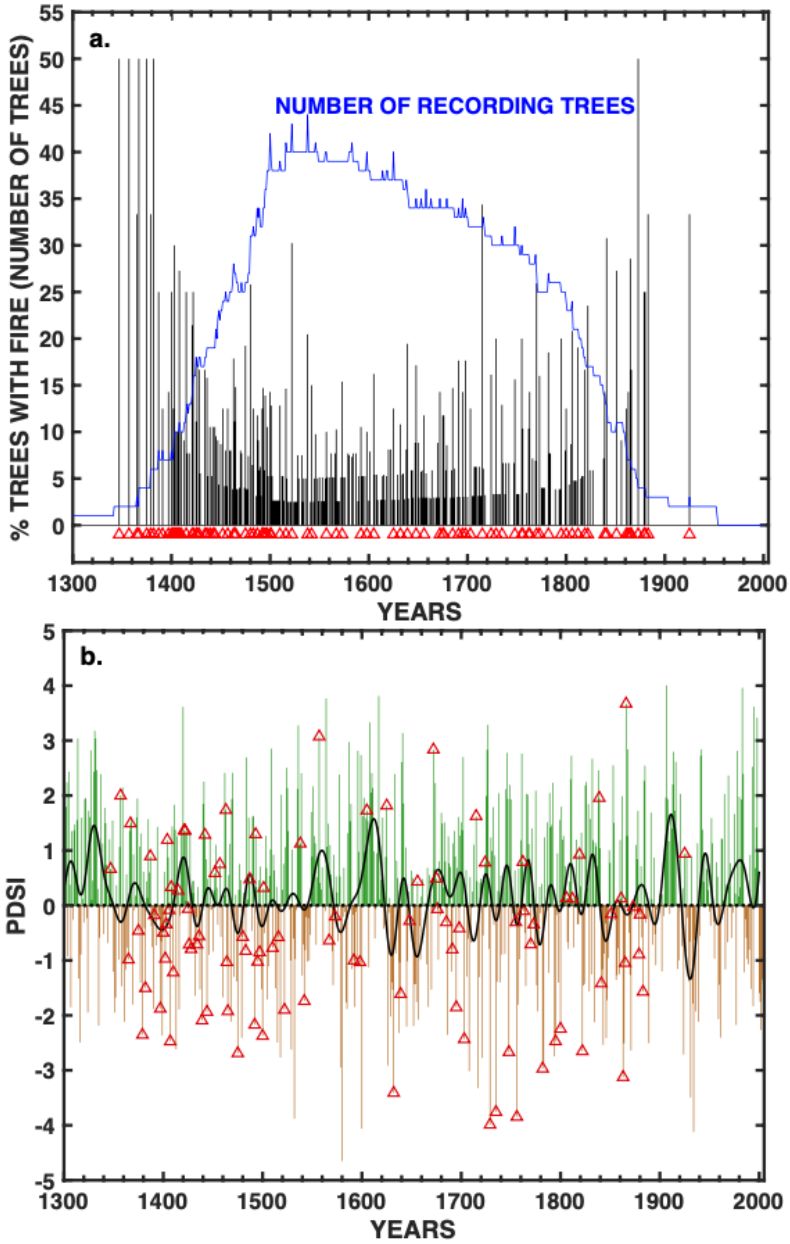

Figure 4.2 Fire event and drought history for the western US between 1300-2005 C.E. (a) Percentage of trees from the *Trouet et al.* [2010] western US compilation that record a fire in a given year (vertical black bars) along with the total number of recording trees (in blue). Red triangles are the final set of 98 candidate fire event key years chosen using a cut-off of at least 10% of scarred samples with a minimum of 2 recording trees. (b) Area-weighted spatial average of mean June-August Palmer Drought Severity Index (JJA PDSI) for the western US (124°W-109°W an 35°N-50°N) from the Living Blended Drought Atlas [*Cook et al.*, 2010b]. The 98 red triangle symbols are the same fire event key years from part (a).

4.3 Methods

The first step of SEA analysis is to develop a composite matrix of event responses. In traditional SEA, rows of the composite matrix each correspond to a key or event year, while columns contain are the data from the time series prior to, during, and following each event [*Haurwitz and Brier*, 1981]. The number of columns depends on the window length of interest. In both examples we chose a window length of 21 years, spanning from 5 years pre-event to 15 years post-event. Year 0, the sixth column in the matrix, therefore corresponds to either a volcanic event year or a fire year. However, unlike conventional SEA, where only one composite matrix is developed for all key year responses, we developed 1,000 unique versions of composite matrices by drawing unique subsets of key years at random without replacement from the key year list.

We draw unique subsets without replacement for two reasons. The first is to avoid biasing each iteration of the composite matrix by drawing the same year multiple times within one draw, and the second is to avoid biasing the final epochal mean probability distribution by making multiple draws with the same combination of key years. The total number of volcanic key years is 20, and the total number of fire key years is 98. For the volcanic forcing SEA experiment, we made 1,000 composite matrices using unique random combinations of 10 volcanic key years without replacement, while for the fire-event drought SEA we made 1,000 unique composite matrices drawing of 50 random fire key years without replacement. While the choice of 10 volcanic and 50 fire year years is relatively arbitrary, these numbers represent approximately half the total number of key events in the dataset, thus giving us reasonable estimates of spread in the response.

We normalised the rows of each composite matrix by subtracting the five-year pre-event mean. This subtraction reduces the impact low-frequency climate variability has on the final epochal mean, and the likelihood that one large event leverages and biases the overall epochal mean of the composite matrix [*Adams et al.*, 2003]. Other approaches to normalization include, i. calculating the epochal response as z-scores reflecting scaled deviations as done within the R [*R Core Team*, 2017] package 'dplR' [*Bunn*, 2008], and ii. calculating the departures of the climate series from average climate conditions as done in the R package 'burnr' [*Malevich et al.*, 2018]. Finally, for each for the 1,000 unique composite matrices we calculated the epochal mean by averaging across each lag, and calculated the final response as the 5^{th} percentile, median, and 95^{th} percentile of the 1,000 epochal mean responses.

We determined the statistical response of the 5^{th} percentile, median, and 95^{th} percentile epochal mean responses using both random bootstrapping and block reshuffling [*Adams et al.*, 2003; *Davi et al.*, 2015]. In both methods, we generated 10,000 iterations of pseudo-composite matrices. For the random bootstrap this was done by drawing sets of pseudo key-years sampled over the entire timeseries. To be consistent with how the final epochal response was calculated, the pseudo- composite matrices were generated by drawing 10 and 50 pseudo key years at random from the *Wilson et al.* [2016] temperature and *Cook et al.* [2010b] PDSI reconstructions respectively. Each set of block reshuffling surrogate matrices was generated by first drawing one of the 1,000 composite matrices at random and then randomly reshuffling blocks of the chosen matrix. The length of each block was determined as twice the e-folding distance of the first-order auto-correlation (AR1) of the temperature and PDSI reconstructions, calculated as $-2/\ln(\rho)$; where ρ is the value of the AR1 coefficient [*Adams et al.*, 2003].

These pseudo composite matrices were normalised in the same fashion as the actual composite matrices by subtracting the five-year pre-event mean. Finally, the 1st, 5th, 10th, 90th, 95th, and 99th percentiles of the epochal means of the pseudo composite matrix were calculated as the significance thresholds needed to be exceeded for the SEA response to be deemed statistically significant.

4.4 Results and Discussion

Our SEA on the northern hemisphere May-August temperature reconstruction shows strong and significant ($p<0.01$) cooling in the years following a volcanic eruption and lasting up to 6 years post-eruption [Figure 4.3 and *Wilson et al.*, 2016]. This result is consistent regardless of whether we use the random bootstrap or block reshuffling methods to test for significance. The strongest cooling response of ~0.47°C, relative to the five-year pre-event mean, occurs one-year post-eruption (i.e. year t+1). The bootstrapped 5th and 95th percentile confidence intervals of the response also show significant cooling ($p<0.01$). The 5th and 95th percentile response represents the degree of variability in the volcanic response based on choices of 1,000 unique sets of 10 key years from a total of 20 potential key years. That the 95th percentile response in year t+1 also shows significant cooling ($p<0.01$) indicates that even the warmest responses in the post-volcanic period are cooler than what would be expected by random variability.

SEA on the *Trouet et al.* [2010] western US fire event dataset shows that fire-events are coincident with anomalously dry years [Figure 4.4 and *Trouet et al.*, 2010]. Median JJA PDSI in fire years is ~ -0.7 units lower than the five-year pre-event mean PDSI. The 95th percentile of PDSI conditions in fire years, which represents a choice of 'wetter' fire-event responses, calculated by drawing 1,000 sets of 50 unique fire key years at random without replacement from

the total list of 98 possible fire years is significant at $p<0.05$ while the median and 5th percentile response are significant at $p<0.001$. In both examples the block bootstrapping and block reshuffling methods produces similarly wide confidence intervals (Figure 4.3 & 4.4). This suggests that, at least in these two cases scrambling the composite matrix to destroy temporal ordering generates similar variability as sampling from the entire timeseries.

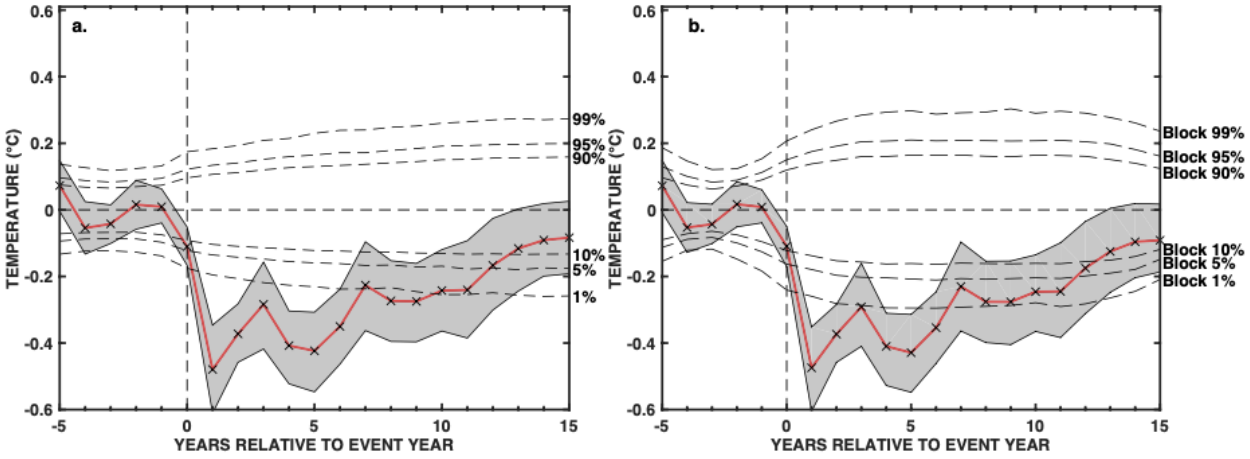

Figure 4.3 Superposed Epoch Analysis (SEA) showing May-August northern hemisphere temperature cooling response to tropical volcanism between 1100-2011 C.E. Uncertainty intervals are 5th and 95th percentiles of the temperature response, while the horizontal lines indicate the threshold required for epochal anomalies to be statistically significant using random bootstrapping (a) and block bootstrapping (b).

Our choice of drawing the 1,000 unique composite matrices from 10 unique volcanic key years at random out of a possible 20 years, and 50 fire key years at random from a total of 98 was based on a choice to keep the number of event years in each unique draw small enough to be able to sample the variability in the response, but at the same time large enough that the epochal mean of each composite matrix can still serve as a high-frequency filter to separate common signal from noise. However, we do note that this choice of the number of key years in each draw (10 eruptions out of 20; 50 fire years out of 98), does impart an additional source of uncertainty the SEA procedure, as the width of the shaded uncertainty intervals in Figure 4.3 and errorbars in Figure 4.4 are functions of the sample size chosen in the bootstrap. While we use the median

response to evaluate statistical significance, the presented shaded uncertainty intervals and errorbars provide a better estimate of variability in the response as is inherent in the data than is provided in conventional SEA. For example, by calculating the variability in the post-volcanic climate response (Figure 4.3), and evaluating the variability in drought conditions coincident with fire years (Figure 4.4), we more effectively account for the fact that not all volcanic events produce the same climate response, and that the magnitude of drought conditions coincident with fire events can be quite variable. Conventional SEA omits this variability by presenting the final response as the simple average of the normalised composite matrix or as symmetric error bars around the mean, which might not be representative of the actual variability, or skewness in the event response distribution.

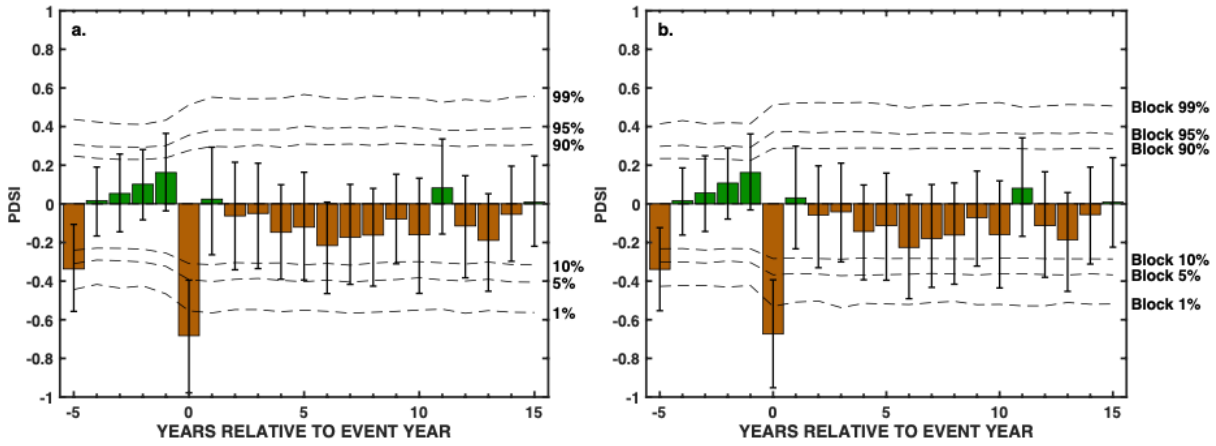

Figure 4.4 SEA showing that western US fire-events are coincident with dry June-August PDSI conditions as reconstructed by the Cook et al. (2010) Living Blended Drought Atlas in year t+0. Similar to Figure 4.3, uncertainty intervals are 5th and 95th percentiles of the drought conditions during fire events, while the horizontal lines indicate the threshold required for epochal anomalies to be statistically significant using random bootstrapping (a) and block bootstrapping (b).

This variability in response is also evident when evaluating the temperature reconstruction in Figure 4.41 and the JJA PDSI reconstruction in Figure 4.2. For example, warm temperatures are reconstructed by Wilson et al. (2016) in 1586 following the eruption of Colima

in 1585. The reasons for the variability in the volcanic response likely include the location of the volcano, stratospheric ejection height, the physical characteristics and spatial distribution of sulphate aerosols, the background climate state, the seasonality of the eruption, and the possibility that the timing of peak forcing might not coincide with the climate-sensitivity of the climate-proxy used [*Guillet et al.*, 2017; *Pausata et al.*, 2016; *Zanchettin et al.*, 2019]. The variability in drought conditions during fire event years is even more evident. The error bars around PDSI conditions coincident with fire-events in year t+0 is negatively skewed. This can be explained by the number of fire events that take place during dry versus wet years (Figure 4.2). Of the 98 fire events, 65 occur when PDSI is less than 0 while 33 events occurred when PDSI is greater than 0. Evaluating fire events during more extreme PDSI values, 17 fire events occur when PDSI is less than -2, while only 3 fire events occur when PDSI is greater than 2. Reasons for variability in drought conditions during fire-event years include the influence of fuel availability and ignition sources on wildfire occurrence [*Abatzoglou and Williams*, 2016; *Bessie and Johnson*, 1995; *Gedalof et al.*, 2005; *Littell et al.*, 2009; *Littell et al.*, 2016a; *Trouet et al.*, 2010; *Westerling et al.*, 2003] uncertainties in the underlying drought reconstruction [Cook et al. 2010], and any uncertainties in defining wildfire event years based on the existing fire scar network [*Falk et al.*, 2011]. All of these observations highlight the contingent and variable nature of event-climate associations.

Our double-bootstrap SEA makes multiple draws of subsets from the key year list and thus presents SEA results in a way that attempts to explicitly account for the influence of these processes during key years. Additionally, by treating key years as random variables we more formally acknowledge that the key year dates for volcanic eruptions might be uncertain [*Toohey and Sigl*, 2017], and that the definition of event years as used here (eruptions with a peak

northern hemisphere AOD > 0.08; at least 10% scarred trees with a minimum of 2 samples) is somewhat arbitrary. While in this study we conducted SEA on two selected timeseries, it is possible to expand this to evaluate SEA responses within a spatial context as well. For example, in *Rao et al.* [2017] we applied this double-bootstrap approach to evaluate the post-volcanic drought response and associated variability over Europe and northern Africa. An additional benefit is that our SEA approach allows us to place additional constraints on the calculation of the epochal mean to avoid the selection of closely spaced volcanic eruptions such as, 1452/1457 and 1808/1815, and fire-years in each unique draw. This reduces bias in the final estimated epochal response by minimising the number of overlapping windows. In the end, even though SEA is only a statistical test of association between the event list and the variable of interest [*Haurwitz and Brier*, 1981], our implementation of a bootstrapped resampling of the key year list provides a statistical framework to explicitly quantify the variability in this association while explicitly acknowledging the uniqueness of each event.

Acknowledgements

The authors thank the Past Global Changes – Volcanic Impacts on Climate and Society (PAGES–VICS) working group members for helpful feedback at the 3rd VICS meeting held at Tucson, AZ, USA in January 2018 and Matt Toohey for providing the volcanic eruption key year list. Lamont Contribution # 8313. KJA is supported by NOAA grant NA18OAR4310420 and NSF grant AGS-1501834.

The full N-TREND *Wilson et al.* [2016] data can be downloaded at https://ntrenddendro.wordpress.com/. The *Trouet et al.* [2010] fire data are available at the

International Multiproxy Paleofire Database at http://www.ncdc.noaa.gov/paleo/impd/paleofire.html. The Cook et al. 2010 Living Blended Drought Atlas is available at https://www.ncdc.noaa.gov/paleo-search/.

The datasets and R and Matlab code used to this study are available at http://dx.doi.org/10.17632/8p7y29hz5h.1

Conclusions

Summary of findings

The overall goal of this dissertation is to reconstruct and better describe hydroclimate variability in several regions of Eurasia including South Asia, Europe, and the Mediterranean. In the first half of the dissertation in Chapters 1 and 2 we developed two streamflow reconstructions in South Asia for the Indus and Brahmaputra rivers respectively. In the second half of the dissertation in Chapter 3 and 4 we evaluated the response of European and Mediterranean hydroclimate to tropical volcanism and described a modified version of Superposed Epoch Analysis to test the statistical significance of the volcanic response.

More specifically, in Chapter 1 we reconstructed past discharge in the UIB at four streamflow gauges (Partab-Bridge, Doyian, Gilgit, and Kachora) between 1394-2008 C.E. We found that streamflow in the UIB is primarily controlled by JFM winter precipitation (as snowfall) and MJJAS summer temperature that influence the rate of snow and glacial melt. We also found that two different statistical methods of reconstructing past streamflow using tree rings (PCR and HBR) produced similar results. Thus, past reconstructions of streamflow are not dependent on the type of methodology used. The sensitivity of streamflow to summer temperature, and projections of continued regional warming, suggest that future streamflow in the UIB may increase in the short-term as long as there remains sufficient snow and glacial mass balance to support increased flow. However, streamflow will likely decrease in the UIB after this point.

In Chapter 2 we reconstructed mean JAS streamflow of the Brahmaputra River at the Bahadurabad gauging station in Bangladesh between 1309-2004 C.E. We found that JAS discharge is most sensitive to upper basin precipitation that falls in the JAS monsoon season. We

found that the instrumental observations are on average much drier than the past seven centuries of streamflow discharge. High discharge years in the Brahmaputra are often associated with flooding. We found that despite major floods in the observed record of discharge, instrumental observations of discharge rank among the driest of the past six centuries. Additionally, CMIP5 projections of runoff suggest large increases relative to instrumental observations by the end of the twenty-first century due to an intensification of the South Asian Summer Monsoon. Based on these, we found that instrumental observations likely underestimate the occurrence of high discharge that is associated with flood hazard both in the context of natural variability and climate change.

In Chapter 3 we used the Old World Drought Atlas (OWDA) and ice core records of volcanism for the past millennium to show that volcanic eruptions can cause dry conditions over Western Europe and the British Isles and wet conditions over the Western Mediterranean. This pattern of wet-dry anomalies following volcanic eruptions resembles a negative phase of the East Atlantic Patter (EAP). We evaluated the post-volcanic hydroclimate response using a modified double bootstrapped SEA. In Chapter 4 we described our modified SEA procedure in more detail. Our modified SEA generates multiple unique draws of the key years, and therefore unlike traditional SEA it evaluates the sign, magnitude, and significance of the relationship between the event (e.g. volcanic eruptions) and response variable (e.g. cooling) within a probabilistic framework.

Large scale controls on the Brahmaputra River discharge

A remarkable finding of the reconstruction of Brahmaputra River discharge presented in Figure 2.3b is the exceptionally dry period in the mid 20th century and the much wetter mean

state conditions prior to that. In this section we briefly discuss potential mechanisms for this apparent shift in the regional hydroclimate regime.

A dominant feature of the tropical climate system that controls the intensity and magnitude of monsoon precipitation is the location and strength of the Intertropical Convergence Zone (ITCZ). The ITCZ is typically defined as a region of intense deep convective clouds that is closely linked to the region of the tropics that receives the highest precipitation rates [*Schneider et al.*, 2014]. During the monsoon season in June-September the mean position of the ITCZ in Northeastern South Asia is located over the Brahmaputra watershed [figure S2b in *Griffiths et al.*, 2016] resulting the high precipitation rates observed in this region (Figure 0.1). A recent study by *Tan et al.* [2019] reconstructs an ITCZ shift index for the past two millennia using speleothem records from the Klang Cave, Thailand and the Liang Luar Cave in eastern Indonesia. The Klang Cave receives a majority of its precipitation from the eastern branch of the South Asian Summer Monsoon similar to the Brahmaputra River watershed [*Tan et al.*, 2019]. The Liang Luar cave on the other hand receives most of its rainfall from the Australian-Indonesian Summer Monsoon [*Griffiths et al.*, 2016].

Tan et al. [2019] find an overall southward shift in the ITCZ in the central Indo-Pacific region in the 20th century and during the Medieval Warm Period (MWP, 950-1300 C.E.) and a northward shift during the Little Ice Age (LIA, 1400-1850 C.E.). They associate this southward shift to enhanced El Niño conditions during the early MWP and in the 20th century. A northward shift in the location of the ITCZ in the central Indo-Pacific region during the LIA and a southward shift during the 20th century would suggest increased precipitation in the Brahmaputra River watershed during the LIA and decreased flows during the 20th century, consistent with the findings of our discharge reconstruction.

Correlations between the *Tan et al.* [2019] ITCZ Shift Index and our discharge reconstruction are however relatively low (r~=0.1, 1309-2004, our discharge reconstruction was smoothed with a 20-year running average to match the temporal resolution of the ITCZ reconstruction). However, the two reconstruction broadly agree regarding the current dry period, and overall wetter conditions prior to ~1900 C.E. (Figure 5.1).

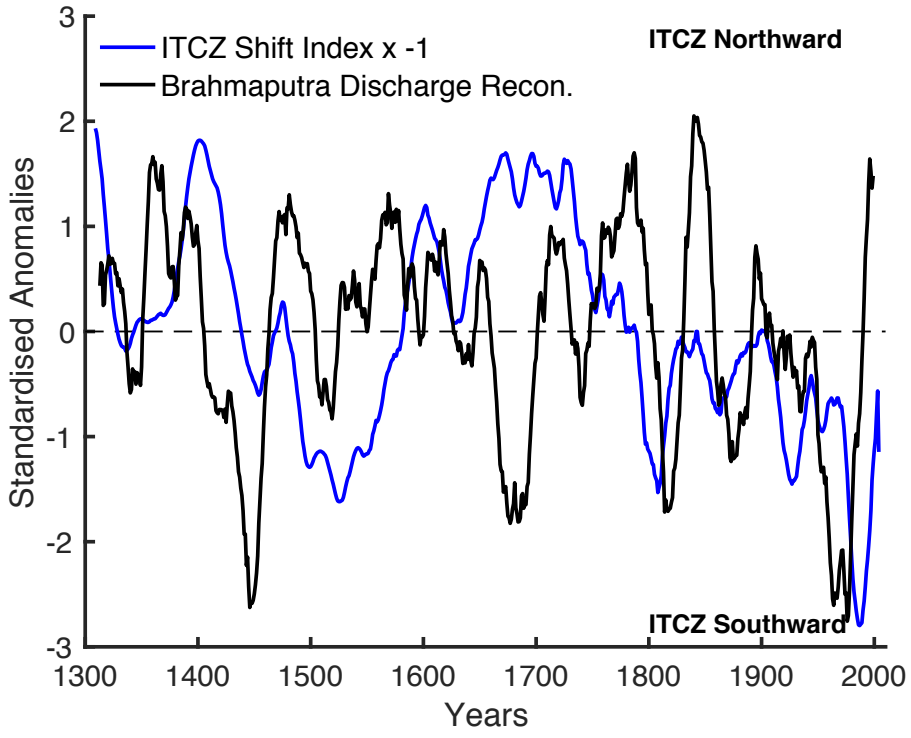

Figure 5.1 Comparison between our Brahmaputra River discharge reconstruction presented in Figure 2.3 and a reconstruction of relative location of the Intertropical Convergence Zone (ITCZ) in the Central Indo-Pacific Ocean region by *Tan et al.* [2019]. The Brahmaputra discharge reconstruction is presented as a 20-year moving average to match the temporal resolution of the ITCZ index reconstruction. Also note that the *Tan et al.* [2019] reconstruction is a composite of multiple speleothem records that have different dating uncertainties. The ITCZ index is multiplied by -1, with positive (negative) values in this figure representing a northward (southward) displaced Central Indo-Pacific ITCZ, corresponding to a stronger (weaker) South Asian Summer Monsoon [*Tan et al.*, 2019]. These modulations of rainfall due to changes in the position of the ITCZ over the central Indo-Pacific ocean can likely influence discharge variability in the Brahmaputra River watershed.

This finding of the a dry 20th century and wet LIA in the Brahmaputra River watershed are also supported by lake level changes inferred from beach evidence at Lake Chenghai, Yunnan Province, China [*Xu et al.*, 2019; *Xu et al.*, 2016] located ~200 km east of the watershed boundary. In their two studies, Xu et al. also conclude that the LIA in this region of South Asia was wet, in contrast to dry hydroclimate conditions in Eastern Asia during the same period.

Recommendations

Most of the available tree ring data in South Asia region are from collections that date back to the late 1990s. Most collections end around or before 2010. Advancing the tree-ring network in Bangladesh, Bhutan, China, India, Myanmar, Nepal, and Pakistan, updating older collections, and sampling non-traditional species will aid in developing more skillful reconstructions of past streamflow and climate in the region. New collections and updates of older collections will also aid in better evaluating ecological and environmental change in the past few decades in light of ongoing regional climate change.

Another limitation to developing hydroclimate reconstructions in South Asia is the lack of long term instrumental observations of river discharge [*Dettinger and Diaz*, 2000]. Due to the long history of human modification to streamflow regimes in the region [*Grill et al.*, 2019], streamflow (and climate) reconstructions are also precluded by the lack of availability of 'natural discharge'. However, the limitation placed by the absence of 'natural' discharge data may partially be resolved in the near future by the advances in river runoff reanalysis products such as ERA-5 (see Figure B.4), river discharge reanalysis such as the Global Flood Awareness System [*Harrigan et al.*, 2020], and satellite altimetry products [*Huang et al.*, 2020]. Thus, future studies could likely use similar datasets to better understand variability in streamflow in South Asia.

Additionally, more work on cross-proxy synthesis across different paleo-proxies such as speleothems [*Myers et al.*, 2015; *Ronay et al.*, 2019; *Sinha et al.*, 2015], slackwater flood deposits and field stratigraphy [*Ely et al.*, 1996; *Kale et al.*, 1994; 1996; *Thomas et al.*, 2007], and the inclusion of historical documentary evidence [*Shi et al.*, 2018b] can help develop longer and more refined reconstructions of hydroclimate and extreme events for South Asia [*Pages Hydro2k Consortium*, 2017].

Improved constraints on the timing, identity, and magnitude of past volcanic eruptions are critical to better understand both the short-term (seasonal to annual) and long-term (decadal to centennial) timescale response of earth's climate system volcanic eruptions. Advances have been made in this regard with improved ice-core dating using multiple ice-cores, better integration of multi-proxy evidence (e.g. tephra geochemistry and cosmogenic radiocarbon spikes in the tree-ring record) and earth system modelling [*McConnell et al.*, 2020; *Oppenheimer et al.*, 2017; *Sigl et al.*, 2015; *Toohey and Sigl*, 2017]. These efforts along with further progress in global and regional paleo-proxy networks and improved statistical methods such as those described in Chapter 3 and 4 can help better resolve or at least better quantify the underlying uncertainties in the hydroclimate response to volcanism. Finally, one additional easily implementable modification to the SEA method presented in Chapter 3 and 4 in cases where the sample size (i.e. number of key years) is low could be to modify the bootstrap method to allow for resampling with replacement of key years.

References

Abatzoglou, J. T., and A. P. Williams (2016), Impact of anthropogenic climate change on wildfire across western US forests, *Proceedings of the National Academy of Sciences*, *113*(42), 11770-11775.

Adams, J. B., M. E. Mann, and C. M. Ammann (2003), Proxy evidence for an El Niño-like response to volcanic forcing, *Nature*, *426*, 274.

Ahmed, M., M. U. Zafar, A. Hussain, M. Akbar, M. Wahab, and N. Khan (2013), Dendroclimatic and dendrohydrological response of two tree species from Gilgit valleys, *Pak J Botany*, *45*, 987-992.

Ahmed, M., J. Palmer, N. Khan, M. Wahab, P. Fenwick, J. Esper, and E. Cook (2011), The dendroclimatic potential of conifers from northern Pakistan, *Dendrochronologia*, *29*(2), 77-88.

Ali, S., D. Li, F. Congbin, and F. Khan (2015), Twenty first century climatic and hydrological changes over Upper Indus Basin of Himalayan region of Pakistan, *Environmental Research Letters*, *10*(1), 014007.

Allen, E. B., T. M. Rittenour, R. J. DeRose, M. F. Bekker, R. Kjelgren, and B. M. Buckley (2013), A tree-ring based reconstruction of Logan River streamflow, northern Utah, *Water Resour. Res.*, *49*(12), 8579-8588.

Allen, K., E. R. Cook, R. Evans, R. J. Francey, B. M. Buckley, J. Palmer, M. J. Peterson, and P. J. Baker (2018), Lack of cool, not warm extremes, distinguishes late 20th Century climate in 979-year Tasmanian summer temperature reconstruction, *Environmental Research Letters*.

Allen, K. J., P. Hope, D. Lam, J. R. Brown, and R. J. Wasson (2020), Improving Australia's flood record for planning purposes – can we do better?, *Australasian Journal of Water Resources*, 1-10.

Amrith, S. (2018), *Unruly Waters: How Mountain Rivers and Monsoons Have Shaped South Asia's History*, Penguin UK.

Anchukaitis, K. J., B. Buckley, E. Cook, B. Cook, R. D'Arrigo, and C. Ammann (2010), Influence of volcanic eruptions on the climate of the Asian monsoon region, *Geophys. Res. Lett.*, *37*(22).

Anchukaitis, K. J., et al. (2012), Tree rings and volcanic cooling, *Nat. Geosci.*, *5*(12), 836-837.

Anchukaitis, K. J., et al. (2017), Last millennium Northern Hemisphere summer temperatures from tree rings: Part II, spatially resolved reconstructions, *Quat. Sci. Rev.*, *163*, 1-22.

Archer, D. R. (2003), Contrasting hydrological regimes in the upper Indus Basin, *J. Hydrol.*, *274*(1), 198-210.

Archer, D. R., N. Forsythe, H. J. Fowler, and S. M. Shah (2010), Sustainability of water resources management in the Indus Basin under changing climatic and socio economic conditions, *Hydrol. Earth Syst. Sci.*, *14*(8), 1669-1680.

Baillie, M. G. (2008), Proposed re-dating of the European ice core chronology by seven years prior to the 7th century AD, *Geophys. Res. Lett.*, *35*(15).

Baisan, C. H., and T. W. Swetnam (1990), Fire history on a desert mountain range: Rincon Mountain Wilderness, Arizona, U.S.A, *Canadian Journal of Forest Research*, *20*(10), 1559-1569.

Ballesteros-Cánovas, J. A., M. Stoffel, S. St George, and K. Hirschboeck (2015), A review of flood records from tree rings, *Progress in Physical Geography: Earth and Environment*, *39*(6), 794-816.

Barnston, A. G., and R. E. Livezey (1987), Classification, seasonality and persistence of low-frequency atmospheric circulation patterns, *Monthly weather review*, *115*(6), 1083-1126.

Bashir, F., X. Zeng, H. Gupta, and P. Hazenberg (2017), A Hydrometeorological Perspective on the Karakoram Anomaly Using Unique Valley-Based Synoptic Weather Observations, *Geophys. Res. Lett.*, *44*(20), 10,470-410,478.

Becker, M., et al. (2020), Water level changes, subsidence, and sea level rise in the Ganges–Brahmaputra–Meghna delta, *Proceedings of the National Academy of Sciences*, 201912921.

Benn, D., and L. Owen (1998), The role of the Indian summer monsoon and the mid-latitude westerlies in Himalayan glaciation: review and speculative discussion, *J. Geol. Soc.*, *155*(2), 353-363.

Bessie, W. C., and E. A. Johnson (1995), The Relative Importance of Fuels and Weather on Fire Behavior in Subalpine Forests, *Ecology*, *76*(3), 747-762.

Best, J. (2019), Anthropogenic stresses on the world's big rivers, *Nat. Geosci.*, *12*(1), 7-21.

Blöschl, G., et al. (2017), Changing climate shifts timing of European floods, *Science*, *357*(6351), 588-590.

Bolch, T., A. Kulkarni, A. Kääb, C. Huggel, F. Paul, J. Cogley, H. Frey, J. S. Kargel, K. Fujita, and M. Scheel (2012), The state and fate of Himalayan glaciers, *Science*, *336*(6079), 310-314.

Bollasina, M. A., Y. Ming, and V. Ramaswamy (2011), Anthropogenic Aerosols and the Weakening of the South Asian Summer Monsoon, *Science*, *334*(6055), 502-505.

Bollasina, M. A., Y. Ming, V. Ramaswamy, M. D. Schwarzkopf, and V. Naik (2014), Contribution of local and remote anthropogenic aerosols to the twentieth century weakening of the South Asian Monsoon, *Geophys. Res. Lett.*, *41*(2), 680-687.

Bookhagen, B., and D. W. Burbank (2010), Toward a complete Himalayan hydrological budget: Spatiotemporal distribution of snowmelt and rainfall and their impact on river discharge, *Journal of Geophysical Research: Earth Surface*, *115*(F3).

Bracken, C., B. Rajagopalan, and C. A. Woodhouse (2016), A Bayesian hierarchical nonhomogeneous hidden Markov model for multisite streamflow reconstructions, *Water Resour. Res.*, *52*(10), 7837-7850.

Bradshaw, C. J. A., N. S. Sodhi, K. S. H. Pem, and B. W. Brook (2007), Global evidence that deforestation amplifies flood risk and severity in the developing world, *Global Change Biol.*, *13*(11), 2379-2395.

Brammer, H. (1990), Floods in Bangladesh: Geographical Background to the 1987 and 1988 Floods, *The Geographical Journal*, *156*(1), 12-22.

Bretherton, C. S., M. Widmann, V. P. Dymnikov, J. M. Wallace, and I. Bladé (1999), The effective number of spatial degrees of freedom of a time-varying field, *J. Clim.*, *12*(7), 1990-2009.

Briffa, K. R., P. D. Jones, F. H. Schweingruber, and T. J. Osborn (1998), Influence of volcanic eruptions on Northern Hemisphere summer temperature over the past 600 years, *Nature*, *393*, 450.

Broccoli, A. J., K. W. Dixon, T. L. Delworth, T. R. Knutson, R. J. Stouffer, and F. Zeng (2003), Twentieth-century temperature and precipitation trends in ensemble climate simulations including natural and anthropogenic forcing, *Journal of Geophysical Research: Atmospheres (1984–2012)*, *108*(D24).

Brun, F., E. Berthier, P. Wagnon, A. Kääb, and D. Treichler (2017), A spatially resolved estimate of High Mountain Asia glacier mass balances from 2000 to 2016, *Nat. Geosci.*, *10*, 668.

Buckley, B. M., E. R. Cook, M. J. Peterson, and M. Barbetti (1997), A changing temperature response with elevation for Lagarostrobos franklinii in Tasmani, Australia, *Clim. Change*, *36*(3), 477-498.

Buckley, B. M., K. J. Anchukaitis, D. Penny, R. Fletcher, E. R. Cook, M. Sano, L. C. Nam, A. Wichienkeeo, T. T. Minh, and T. M. Hong (2010), Climate as a contributing factor in the demise of Angkor, Cambodia, *Proceedings of the National Academy of Sciences*, *107*(15), 6748-6752.

Bunn, A. G. (2008), A dendrochronology program library in R (dplR), *Dendrochronologia*, *26*(2), 115-124.

Bunn, A. G. (2010), Statistical and visual crossdating in R using the dplR library, *Dendrochronologia*, *28*(4), 251-258.

Bunn, A. G., M. W. Salzer, K. J. Anchukaitis, J. M. Bruening, and M. K. Hughes (2018), Spatiotemporal Variability in the Climate Growth Response of High Elevation Bristlecone Pine in the White Mountains of California, *Geophys. Res. Lett.*, *45*(24), 13,312-313,321.

Büntgen, U., et al. (2017), New tree-ring evidence from the Pyrenees reveals Western Mediterranean climate variability since medieval times, *J. Clim.*(2017).

Casty, C., C. C. Raible, T. F. Stocker, H. Wanner, and J. Luterbacher (2007), A European pattern climatology 1766–2000, *Clim. Dyn.*, *29*(7-8), 791-805.

Chen, F., H. Shang, I. Panyushkina, D. Meko, J. Li, Y. Yuan, S. Yu, F. Chen, D. He, and X. Luo (2019), 500-year tree-ring reconstruction of Salween River streamflow related to the history of water supply in Southeast Asia, *Clim. Dyn.*, *53*(11), 6595-6607.

Chen, Y., M. H. Gagen, F. Chen, H. Zhang, H. Shang, and H. Xu (2020), Precipitation variations recorded in tree rings from the upper Salween and Brahmaputra River valleys, China, *Ecol. Indicators*, *113*, 106189.

Chowdhury, M. Q., M. De Ridder, and H. Beeckman (2016), Climatic Signals in Tree Rings of Heritiera fomes Buch.-Ham. in the Sundarbans, Bangladesh, *PLOS ONE*, *11*(2), e0149788.

Chowdhury, M. R. (2000), An Assessment of Flood Forecasting in Bangladesh: The Experience of the 1998 Flood, *Nat. Hazards*, *22*(2), 139-163.

Cliff, A. D., and J. K. Ord (1981), Spatial and temporal analysis: autocorrelation in space and time, *Quantitative geography: a British view*, 104-110.

Coleman, J. M. (1969), Brahmaputra river: Channel processes and sedimentation, *Sediment. Geol.*, *3*(2), 129-239.

Colose, C. M., A. N. LeGrande, and M. Vuille (2016), Hemispherically asymmetric volcanic forcing of tropical hydroclimate during the last millennium, *Earth Syst. Dynam.*, *7*(3), 681-696.

Cook, B. I., T. R. Ault, and J. E. Smerdon (2015a), Unprecedented 21st century drought risk in the American Southwest and Central Plains, *Science Advances*, *1*(1), e1400082.

Cook, E. R., and G. C. Jacoby (1983), Potomac River Streamflow Since 1730 as Reconstructed by Tree Rings, *J. Clim. Appl. Meteorol.*, *22*(10), 1659-1672.

Cook, E. R., and L. Kairiukstis (1990), *Methods of Dendrochronology: Applications in the Environmental Sciences*, Springer Science & Business Media.

Cook, E. R., P. J. Krusic, and P. D. Jones (2003), Dendroclimatic signals in long tree-ring chronologies from the Himalayas of Nepal, *Int. J. Climatol.*, *23*(7), 707-732.

Cook, E. R., P. J. Krusic, and D. Dukpa (2011a), NOAA/WDS Paleoclimatology - Cook - Chele La - LAGR - ITRDB BT017, *NOAA National Centers for Environmental Information*.

Cook, E. R., P. J. Krusic, and D. Dukpa (2011b), NOAA/WDS Paleoclimatology - Cook - Laya-1 - LAGR - ITRDB BT016, *NOAA National Centers for Environmental Information*.

Cook, E. R., P. J. Krusic, and D. Dukpa (2011c), NOAA/WDS Paleoclimatology - Cook - Gasa-1 - JURE - ITRDB BT019, *NOAA National Centers for Environmental Information*.

Cook, E. R., D. M. Meko, D. W. Stahle, and M. K. Cleaveland (1999a), Drought reconstructions for the continental United States*, *J. Clim.*, *12*(4), 1145-1162.

Cook, E. R., D. M. Meko, D. W. Stahle, and M. K. Cleaveland (1999b), Drought Reconstructions for the Continental United States, *J. Clim.*, *12*(4), 1145-1162.

Cook, E. R., C. A. Woodhouse, C. M. Eakin, D. M. Meko, and D. W. Stahle (2004), Long-Term Aridity Changes in the Western United States, *Science*, *306*(5698), 1015-1018.

Cook, E. R., K. J. Anchukaitis, B. M. Buckley, R. D. D'Arrigo, G. C. Jacoby, and W. E. Wright (2010a), Asian Monsoon Failure and Megadrought During the Last Millennium, *Science*, *328*(5977), 486-489.

Cook, E. R., R. Seager, R. R. Heim Jr, R. S. Vose, C. Herweijer, and C. Woodhouse (2010b), Megadroughts in North America: placing IPCC projections of hydroclimatic change in a long-term palaeoclimate context, *J. Quat. Sci.*, *25*(1), 48-61.

Cook, E. R., P. J. Krusic, K. J. Anchukaitis, B. M. Buckley, T. Nakatsuka, and M. Sano (2013a), Tree-ring reconstructed summer temperature anomalies for temperate East Asia since 800 CE, *Clim. Dyn.*, *41*(11-12), 2957-2972.

Cook, E. R., Y. Kushnir, J. E. Smerdon, A. P. Williams, K. J. Anchukaitis, and E. R. Wahl (2019), A Euro-Mediterranean tree-ring reconstruction of the winter NAO index since 910 C.E, *Clim. Dyn.*

Cook, E. R., J. G. Palmer, M. Ahmed, C. A. Woodhouse, P. Fenwick, M. U. Zafar, M. Wahab, and N. Khan (2013b), Five centuries of Upper Indus River flow from tree rings, *J. Hydrol.*, *486*, 365-375.

Cook, E. R., et al. (2015b), Old World megadroughts and pluvials during the Common Era, *Science Advances*, *1*(10), e1500561.

Cooley, W. W., and P. R. Lohnes (1971), *Multivariate data analysis*, J. Wiley.

Copernicus Climate Change Service (C3S) (2019), C3S ERA5-Land reanalysis . Copernicus Climate Change Service https://cds.climate.copernicus.eu/cdsapp#!/home.

Cox, D., J. Hunt, P. Mason, H. Wheater, P. Wolf, and D. W. Reed (2002), Reinforcing flood-risk estimation, *Philosophical Transactions of the Royal Society of London. Series A: Mathematical, Physical and Engineering Sciences*, *360*(1796), 1373-1387.

Crowley, T., and M. Unterman (2013), Technical details concerning development of a 1200 yr proxy index for global volcanism, *Earth System Science Data*, *5*(1), 187-197.

D'Arrigo, R. D., E. R. Cook, G. C. Jacoby, and K. R. Briffa (1993), Nao and sea surface temperature signatures in tree-ring records from the North Atlantic sector, *Quat. Sci. Rev.*, *12*(6), 431-440.

D'Arrigo, R., R. Wilson, and A. Tudhope (2009), The impact of volcanic forcing on tropical temperatures during the past four centuries, *Nat. Geosci.*, *2*(1), 51-56.

D'Arrigo, R., N. Abram, C. Ummenhofer, J. Palmer, and M. Mudelsee (2011), Reconstructed streamflow for Citarum River, Java, Indonesia: linkages to tropical climate dynamics, *Clim. Dyn.*, *36*(3-4), 451-462.

Dai, A. (2011), Characteristics and trends in various forms of the Palmer Drought Severity Index during 1900–2008, *Journal of Geophysical Research: Atmospheres*, *116*(D12).

Dai, A., K. E. Trenberth, and T. Qian (2004), A global dataset of Palmer Drought Severity Index for 1870-2002: Relationship with soil moisture and effects of surface warming, *J. Hydrometeorol.*, *5*(6), 1117-1130.

Davi, N. K., R. D'Arrigo, G. C. Jacoby, E. R. Cook, K. J. Anchukaitis, B. Nachin, M. P. Rao, and C. Leland (2015), A long-term context (931–2005 C.E.) for rapid warming over Central Asia, *Quat. Sci. Rev.*, *121*, 89-97.

de Kok, R. J., O. A. Tuinenburg, P. N. J. Bonekamp, and W. W. Immerzeel (2018), Irrigation as a potential driver for anomalous glacier behaviour in High Mountain Asia, *Geophys. Res. Lett.*

Dettinger, M. D., and H. F. Diaz (2000), Global Characteristics of Stream Flow Seasonality and Variability, *J. Hydrometeorol.*, *1*(4), 289-310.

Deutsch, M., and F. H. Ruggles (1978), Hydrological applications of Landsat Imagerty used in the study of the 1973 Indus River flood, Pakistan, *JAWRA Journal of the American Water Resources Association*, *14*(2), 261-274.

Devineni, N., U. Lall, N. Pederson, and E. Cook (2013), A Tree-Ring-Based Reconstruction of Delaware River Basin Streamflow Using Hierarchical Bayesian Regression, *J. Clim.*, *26*(12), 4357-4374.

Driscoll, S., A. Bozzo, L. J. Gray, A. Robock, and G. Stenchikov (2012), Coupled Model Intercomparison Project 5 (CMIP5) simulations of climate following volcanic eruptions, *Journal of Geophysical Research: Atmospheres*, *117*(D17).

Ely, L. L., Y. Enzel, V. R. Baker, V. S. Kale, and S. Mishra (1996), Changes in the magnitude and frequency of late Holocene monsoon floods on the Narmada River, central India, *GSA Bulletin*, *108*(9), 1134-1148.

Esper, J., L. Schneider, P. J. Krusic, J. Luterbacher, U. Büntgen, M. Timonen, F. Sirocko, and E. Zorita (2013a), European summer temperature response to annually dated volcanic eruptions over the past nine centuries, *Bull. Volcanol.*, *75*(7), 1-14.

Esper, J., L. Schneider, P. J. Krusic, J. Luterbacher, U. Büntgen, M. Timonen, F. Sirocko, and E. Zorita (2013b), European summer temperature response to annually dated volcanic eruptions over the past nine centuries, *Bull. Volcanol.*, *75*(7), 736.

Falk, D. A., E. K. Heyerdahl, P. M. Brown, C. Farris, P. Z. Fulé, D. McKenzie, T. W. Swetnam, A. H. Taylor, and M. L. Van Horne (2011), Multi-scale controls of historical forest-fire regimes: new insights from fire-scar networks, *Front. Ecol. Environ.*, *9*(8), 446-454.

Farhan, S. B., Y. Zhang, Y. Ma, Y. Guo, and N. Ma (2014), Hydrological regimes under the conjunction of westerly and monsoon climates: a case investigation in the Astore Basin, Northwestern Himalaya, *Clim. Dyn.*, 1-18.

Fischer, E., S. Seneviratne, P. Vidale, D. Lüthi, and C. Schär (2007a), Soil moisture-atmosphere interactions during the 2003 European summer heat wave, *J. Clim.*, *20*(20), 5081-5099.

Fischer, E., J. Luterbacher, E. Zorita, S. Tett, C. Casty, and H. Wanner (2007b), European climate response to tropical volcanic eruptions over the last half millennium, *Geophys. Res. Lett.*, *34*(5).

Flower, A., D. G. Gavin, E. K. Heyerdahl, R. A. Parsons, and G. M. Cohn (2014), Drought-triggered western spruce budworm outbreaks in the interior Pacific Northwest: A multi-century dendrochronological record, *For. Ecol. Manage.*, *324*, 16-27.

Folland, C. K., J. Knight, H. W. Linderholm, D. Fereday, S. Ineson, and J. W. Hurrell (2009), The summer North Atlantic Oscillation: past, present, and future, *J. Clim.*, *22*(5), 1082-1103.

Forsythe, N., H. J. Fowler, X.-F. Li, S. Blenkinsop, and D. Pritchard (2017), Karakoram temperature and glacial melt driven by regional atmospheric circulation variability, *Nature Climate Change*, *7*, 664.

Fowler, H., and D. Archer (2006), Conflicting signals of climatic change in the Upper Indus Basin, *J. Clim.*, *19*(17), 4276-4293.

Fritts, H. (1976), Tree rings and climate, 567 pp, *Academic, San Diego, Calif*.

Gagen, M., D. McCarroll, and J.-L. Edouard (2006), Combining Ring Width, Density and Stable Carbon Isotope Proxies to Enhance the Climate Signal in Tree-Rings: An Example from the Southern French Alps, *Clim. Change*, *78*(2), 363-379.

Gain, A. K., W. W. Immerzeel, F. C. Sperna Weiland, and M. F. P. Bierkens (2011), Impact of climate change on the stream flow of the lower Brahmaputra: trends in high and low flows based on discharge-weighted ensemble modelling, *Hydrol. Earth Syst. Sci.*, *15*(5), 1537-1545.

Gangopadhyay, S., B. L. Harding, B. Rajagopalan, J. J. Lukas, and T. J. Fulp (2009), A nonparametric approach for paleohydrologic reconstruction of annual streamflow ensembles, *Water Resour. Res.*, *45*(6).

Gao, C., A. Robock, and C. Ammann (2008), Volcanic forcing of climate over the past 1500 years: An improved ice core-based index for climate models, *Journal of Geophysical Research: Atmospheres*, *113*(D23).

Gao, Y., and C. Gao (2017), European hydroclimate response to volcanic eruptions over the past nine centuries, *Int. J. Climatol.*

Gardelle, J., E. Berthier, and Y. Arnaud (2012), Slight mass gain of Karakoram glaciers in the early twenty-first century, *Nat. Geosci.*, *5*(5), 322-325.

Gedalof, Z. e., D. L. Peterson, and N. J. Mantua (2005), Atmospheric, climatic, and ecological controls on extreme wildfire years in the Northwestern United States, *Ecol. Appl.*, *15*(1), 154-174.

Gelman, A., and D. B. Rubin (1992), Inference from iterative simulation using multiple sequences, *Statistical science*, 457-472.

Gelman, A., and J. Hill (2006), *Data analysis using regression and multilevel/hierarchical models*, Cambridge University Press.

George, S. S., D. M. Meko, and E. R. Cook (2010), The seasonality of precipitation signals embedded within the North American Drought Atlas, *The Holocene*, *20*(6), 983-988.

Gou, X., F. Chen, E. Cook, G. Jacoby, M. Yang, and J. Li (2007), Streamflow variations of the Yellow River over the past 593 years in western China reconstructed from tree rings, *Water Resour. Res.*, *43*(6).

Greene, A. M., and A. W. Robertson (2017), Interannual and low-frequency variability of Upper Indus Basin winter/spring precipitation in observations and CMIP5 models, *Clim. Dyn.*, *49*(11), 4171-4188.

Griffiths, M. L., A. K. Kimbrough, M. K. Gagan, R. N. Drysdale, J. E. Cole, K. R. Johnson, J.-X. Zhao, B. I. Cook, J. C. Hellstrom, and W. S. Hantoro (2016), Western Pacific hydroclimate linked to global climate variability over the past two millennia, *Nature Communications*, *7*(1), 11719.

Grill, G., et al. (2019), Mapping the world's free-flowing rivers, *Nature*, *569*(7755), 215-221.

Guillet, S., et al. (2017), Climate response to the Samalas volcanic eruption in 1257 revealed by proxy records, *Nat. Geosci.*, *10*, 123.

Guttman, L. (1954), Some necessary conditions for common-factor analysis, *Psychometrika*, *19*(2), 149-161.

Harley, G. L., and J. T. Maxwell (2017), Current declines of Pecos River (New Mexico, USA) streamflow in a 700-year context, *The Holocene*, *0*(0), 0959683617744263.

Harley, G. L., J. T. Maxwell, E. Larson, H. D. Grissino-Mayer, J. Henderson, and J. Huffman (2017), Suwannee River flow variability 1550–2005 CE reconstructed from a multispecies tree-ring network, *J. Hydrol.*, *544*, 438-451.

Harpold, A. A., and P. D. Brooks (2018), Humidity determines snowpack ablation under a warming climate, *Proceedings of the National Academy of Sciences*.

Harrigan, S., E. Zsoter, L. Alfieri, C. Prudhomme, P. Salamon, F. Wetterhall, C. Barnard, H. Cloke, and F. Pappenberger (2020), GloFAS-ERA5 operational global river discharge reanalysis 1979-present, *Earth Syst. Sci. Data Discuss.*, *2020*, 1-23.

Harris, I., P. D. Jones, T. J. Osborn, and D. H. Lister (2014a), Updated high-resolution grids of monthly climatic observations – the CRU TS3.10 Dataset, *Int. J. Climatol.*, *34*(3), 623-642.

Harris, I., P. Jones, T. Osborn, and D. Lister (2014b), Updated high-resolution grids of monthly climatic observations–the CRU TS3. 10 Dataset, *Int. J. Climatol.*, *34*(3), 623-642.

Hasson, S., J. Böhner, and V. Lucarini (2017), Prevailing climatic trends and runoff response from Hindukush–Karakoram–Himalaya, upper Indus Basin, *Earth Syst. Dynam.*, *8*(2), 337-355.

Haurwitz, M. W., and G. W. Brier (1981), A critique of the superposed epoch analysis method: its application to solar-weather relations, *Monthly Weather Review*, *109*(10), 2074-2079.

He, M., A. Bräuning, J. Grießinger, P. Hochreuther, and J. Wernicke (2018), May–June drought reconstruction over the past 821 years on the south-central Tibetan Plateau derived from tree-ring width series, *Dendrochronologia*, *47*, 48-57.

Hessl, A. E., D. McKenzie, and R. Schellhaas (2004), Drought and Pacific Decadal Oscillation linked to fire occurance in the inland Pacific Northwest, *Ecol. Appl.*, *14*(2), 425-442.

Hessl, A. E., P. Brown, O. Byambasuren, S. Cockrell, C. Leland, E. Cook, B. Nachin, N. Pederson, T. Saladyga, and B. Suran (2016), Fire and climate in Mongolia (1532–2010 Common Era), *Geophys. Res. Lett.*, *43*(12), 6519-6527.

Hessl, A. E., K. J. Anchukaitis, C. Jelsema, B. Cook, O. Byambasuren, C. Leland, B. Nachin, N. Pederson, H. Tian, and L. A. Hayles (2018), Past and future drought in Mongolia, *Science Advances*, *4*(3), e1701832.

Hewitt, K. (2005), The Karakoram anomaly? Glacier expansion and the'elevation effect,'Karakoram Himalaya, *Mountain Research and Development*, *25*(4), 332-340.

Hirabayashi, Y., R. Mahendran, S. Koirala, L. Konoshima, D. Yamazaki, S. Watanabe, H. Kim, and S. Kanae (2013), Global flood risk under climate change, *Nature Climate Change*, *3*(9), 816-821.

Ho, M., U. Lall, X. Sun, and E. R. Cook (2017), Multiscale temporal variability and regional patterns in 555 years of conterminous U.S. streamflow, *Water Resour. Res.*, *53*(4), 3047-3066.

Hopson, T. M., and P. J. Webster (2010), A 1–10-Day Ensemble Forecasting Scheme for the Major River Basins of Bangladesh: Forecasting Severe Floods of 2003–07, *J. Hydrometeorol.*, *11*(3), 618-641.

Huang, Q., D. Long, M. Du, Z. Han, and P. Han (2020), Daily continuous river discharge estimation for ungauged basins using a hydrologic model calibrated by satellite altimetry: Implications for the SWOT mission, *Water Resour. Res.*, *in press*, e2020WR027309.

Huffman, G. J., D. T. Bolvin, E. J. Nelkin, D. B. Wolff, R. F. Adler, G. Gu, Y. Hong, K. P. Bowman, and E. F. Stocker (2007), The TRMM Multisatellite Precipitation Analysis (TMPA): Quasi-Global, Multiyear, Combined-Sensor Precipitation Estimates at Fine Scales, *J. Hydrometeorol.*, *8*(1), 38-55.

Huss, M., and R. Hock (2018), Global-scale hydrological response to future glacier mass loss, *Nature Climate Change*.

Iles, C. E., and G. C. Hegerl (2014), The global precipitation response to volcanic eruptions in the CMIP5 models, *Environmental Research Letters*, *9*(10), 104012.

Iles, C. E., G. C. Hegerl, A. P. Schurer, and X. Zhang (2013), The effect of volcanic eruptions on global precipitation, *Journal of Geophysical Research: Atmospheres*, *118*(16), 8770-8786.

Immerzeel, W. (2008), Historical trends and future predictions of climate variability in the Brahmaputra basin, *Int. J. Climatol.*, *28*(2), 243-254.

Immerzeel, W. W., L. P. H. van Beek, and M. F. P. Bierkens (2010), Climate Change Will Affect the Asian Water Towers, *Science*, *328*(5984), 1382-1385.

Immerzeel, W. W., F. Pellicciotti, and M. F. P. Bierkens (2013), Rising river flows throughout the twenty-first century in two Himalayan glacierized watersheds, *Nat. Geosci.*, *6*, 742.

Immerzeel, W. W., P. Droogers, S. M. de Jong, and M. F. P. Bierkens (2009), Large-scale monitoring of snow cover and runoff simulation in Himalayan river basins using remote sensing, *Remote Sens. Environ.*, *113*(1), 40-49.

Islam, M., M. Rahman, and A. Bräuning (2018), Growth-Ring Boundary Anatomy and Dendrochronological Potential in a Moist Tropical Forest in Northeastern Bangladesh, *Tree-Ring Research*, *74*(1), 76-93.

Janssen, P. H. M., and P. S. C. Heuberger (1995), Calibration of process-oriented models, *Ecol. Model.*, *83*(1), 55-66.

Jian, J., P. J. Webster, and C. D. Hoyos (2009), Large-scale controls on Ganges and Brahmaputra river discharge on intraseasonal and seasonal time-scales, *Q. J. Roy. Meteorol. Soc.*, *135*(639), 353-370.

Joseph, R., and N. Zeng (2011), Seasonally modulated tropical drought induced by volcanic aerosol, *J. Clim.*, *24*(8), 2045-2060.

Kaiser, H. F. (1960), The Application of Electronic Computers to Factor Analysis, *Educational and Psychological Measurement*, *20*(1), 141-151.

Kale, V. S., L. L. Ely, Y. Enzel, and V. R. Baker (1994), Geomorphic and hydrologic aspects of monsoon floods on the Narmada and Tapi Rivers in central India, in *Geomorphology and Natural Hazards*, edited by M. Morisawa, pp. 157-168, Elsevier, Amsterdam.

Kale, V. S., L. L. Ely, Y. Enzel, and V. R. Baker (1996), Palaeo and historical flood hydrology, Indian Peninsula, *Geological Society, London, Special Publications*, *115*(1), 155-163.

Kalnay, E., M. Kanamitsu, R. Kistler, W. Collins, D. Deaven, L. Gandin, M. Iredell, S. Saha, G. White, and J. Woollen (1996), The NCEP/NCAR 40-year reanalysis project, *Bull. Am. Meteorol. Soc.*, *77*(3), 437-471.

Kapnick, S. B., T. L. Delworth, M. Ashfaq, S. Malyshev, and P. Milly (2014), Snowfall less sensitive to warming in Karakoram than in Himalayas due to a unique seasonal cycle, *Nat. Geosci.*, *7*(11), 834-840.

Kelly, P. M., and C. B. Sear (1984), Climatic impact of explosive volcanic eruptions, *Nature*, *311*(5988), 740-743.

Kelly, P. M., P. D. Jones, and J. Pengqun (1996), The spatial response of the climate system to explosive volcanic eruptions, *Int. J. Climatol.*, *16*(5), 537-550.

Kipfmueller, K. F., E. A. Schneider, S. A. Weyenberg, and L. B. Johnson (2017), Historical drivers of a frequent fire regime in the red pine forests of Voyageurs National Park, MN, USA, *For. Ecol. Manage.*, *405*, 31-43.

Knutti, R., and J. Sedláček (2013), Robustness and uncertainties in the new CMIP5 climate model projections, *Nature Climate Change*, *3*(4), 369-373.

Kraaijenbrink, P. D. A., M. F. P. Bierkens, A. F. Lutz, and W. W. Immerzeel (2017), Impact of a global temperature rise of 1.5 degrees Celsius on Asia's glaciers, *Nature*, *549*, 257.

Krusic, P. J. (2005a), NOAA/WDS Paleoclimatology - Krusic - Yalung Khola - TSDU - ITRDB NEPA042, *NOAA National Centers for Environmental Information*.

Krusic, P. J. (2005b), NOAA/WDS Paleoclimatology - Krusic - Rachel's Death - ABSB - ITRDB NEPA036, *NOAA National Centers for Environmental Information*.

Krusic, P. J. (2005c), NOAA/WDS Paleoclimatology - Krusic - Lamite Bhajyung - ABSB - ITRDB NEPA027, *NOAA National Centers for Environmental Information*.

Krusic, P. J., and E. R. Cook (2002), NOAA/WDS Paleoclimatology - Krusic - Bhule Pokari - JURE - ITRDB NEPA010, *NOAA National Centers for Environmental Information*.

Krusic, P. J., E. R. Cook, D. Dukpa, A. E. Putnam, S. Rupper, and J. Schaefer (2015), Six hundred thirty-eight years of summer temperature variability over the Bhutanese Himalaya, *Geophys. Res. Lett.*, *42*(8), 2988-2994.

Kundzewicz, Z. W., D. L. T. Hegger, P. Matczak, and P. P. J. Driessen (2018), Opinion: Flood-risk reduction: Structural measures and diverse strategies, *Proceedings of the National Academy of Sciences*, *115*(49), 12321-12325.

Lévesque, M., A. Rigling, H. Bugmann, P. Weber, and P. Brang (2014), Growth response of five co-occurring conifers to drought across a wide climatic gradient in Central Europe, *Agr. Forest Meteorol.*, *197*, 1-12.

Li, J., J. Shi, D. D. Zhang, B. Yang, K. Fang, and P. H. Yue (2017), Moisture increase in response to high-altitude warming evidenced by tree-rings on the southeastern Tibetan Plateau, *Clim. Dyn.*, *48*(1), 649-660.

Li, J., et al. (2019), Deciphering Human Contributions to Yellow River Flow Reductions and Downstream Drying Using Centuries-Long Tree Ring Records, *Geophys. Res. Lett.*, *46*(2), 898-905.

Liebig, J. F. v. (1841), *Die organische Chemie in ihrer Anwendung auf Agricultur und Physiologie*, 3. unveränderter Abdruck. ed., F. Vieweg, Braunschweig :.

Littell, J. S., D. McKenzie, D. L. Peterson, and A. L. Westerling (2009), Climate and wildfire area burned in western U.S. ecoprovinces, 1916–2003, *Ecol. Appl.*, *19*(4), 1003-1021.

Littell, J. S., D. L. Peterson, K. L. Riley, Y. Liu, and C. H. Luce (2016a), A review of the relationships between drought and forest fire in the United States, *Global Change Biol.*, *22*(7), 2353-2369.

Littell, J. S., G. T. Pederson, S. T. Gray, M. Tjoelker, A. F. Hamlet, and C. A. Woodhouse (2016b), Reconstructions of Columbia River Streamflow from Tree-Ring Chronologies in the Pacific Northwest, USA, *JAWRA Journal of the American Water Resources Association*, *52*(5), 1121-1141.

Liu, J., B. Yang, K. Huang, and D. M. Sonechkin (2012), Annual regional precipitation variations from a 700 year tree-ring record in south Tibet, western China, *Clim. Res.*, *53*(1), 25-41.

Liu, Y., et al. (2019), Anthropogenic Aerosols Cause Recent Pronounced Weakening of Asian Summer Monsoon Relative to Last Four Centuries, *Geophys. Res. Lett.*, *0*(0).

Ljungqvist, F. C., P. J. Krusic, H. S. Sundqvist, E. Zorita, G. Brattström, and D. Frank (2016), Northern Hemisphere hydroclimate variability over the past twelve centuries, *Nature*, *532*(7597), 94-98.

Lough, J. M., and H. C. Fritts (1987), An assessment of the possible effects of volcanic eruptions on North American climate using tree-ring data, 1602 to 1900 A.D, *Clim. Change*, *10*(3), 219-239.

Luterbacher, J., and C. Pfister (2015), The year without a summer, Nat. Geosci., 8, 246–248, edited.

Luterbacher, J., et al. (2016), European summer temperatures since Roman times, *Environmental Research Letters*, *11*(2), 024001.

Lutz, A. F., W. W. Immerzeel, A. B. Shrestha, and M. F. P. Bierkens (2014), Consistent increase in High Asia's runoff due to increasing glacier melt and precipitation, *Nature Climate Change*, *4*, 587.

Lutz, A. F., W. Immerzeel, P. Kraaijenbrink, A. B. Shrestha, and M. F. Bierkens (2016), Climate change impacts on the upper indus hydrology: sources, shifts and extremes, *PloS one*, *11*(11), e0165630.

Mahalanobis, P. C. (1927), *Report on rainfall and floods in North Bengal, 1870-1922*, Bengal Secretariat Book Depot.

Mahanta, C., and L. Saikia (2015), The Brahmaputra and other rivers of the North-east, *Living rivers, Dying Rivers*, 155.

Malevich, S. B., C. H. Guiterman, and E. Q. Margolis (2018), burnr: Fire history analysis and graphics in R, *Dendrochronologia*, *49*, 9-15.

Martin, J. T., et al. (2019), 1200 years of Upper Missouri River streamflow reconstructed from tree rings, *Quat. Sci. Rev.*, *224*, 105971.

Martín-Benito, D., P. Cherubini, M. del Río, and I. Cañellas (2008), Growth response to climate and drought in Pinus nigra Arn. trees of different crown classes, *Trees*, *22*(3), 363-373.

Maurer, J. M., J. M. Schaefer, S. Rupper, and A. Corley (2019), Acceleration of ice loss across the Himalayas over the past 40 years, *Science Advances*, *5*(6), eaav7266.

Maxwell, J. T., G. L. Harley, and A. F. Rahman (2018), Annual Growth Rings in Two Mangrove Species from the Sundarbans, Bangladesh Demonstrate Linkages to Sea-Level Rise and Broad-Scale Ocean-Atmosphere Variability, *Wetlands*, *38*(6), 1159-1170.

McConnell, J. R., et al. (2020), Extreme climate after massive eruption of Alaska's Okmok volcano in 43 BCE and effects on the late Roman Republic and Ptolemaic Kingdom, *Proceedings of the National Academy of Sciences*, *117*(27), 15443-15449.

McGlade, J., G. Bankoff, J. Abrahams, S. Cooper-Knock, F. Cotecchia, P. Desanker, W. Erian, E. Gencer, L. Gibson, and S. Girgin (2019), Global Assessment Report on Disaster Risk Reduction 2019, edited, UN Office for Disaster Risk Reduction.

Meehl, G. A., W. M. Washington, C. M. Ammann, J. M. Arblaster, T. Wigley, and C. Tebaldi (2004), Combinations of natural and anthropogenic forcings in twentieth-century climate, *J. Clim.*, *17*(19), 3721-3727.

Meko, D. M. (1997), Dendroclimatic Reconstruction with Time Varying Predictor Subsets of Tree Indices, *J. Clim.*, *10*(4), 687-696.

Meko, D. M. (2006), Tree-Ring Inferences on Water-Level Fluctuations of Lake Athabasca, *Canadian Water Resources Journal / Revue canadienne des ressources hydriques*, *31*(4), 229-248.

Meko, D. M., and C. A. Woodhouse (2011), Application of Streamflow Reconstruction to Water Resources Management, in *Dendroclimatology: Progress and Prospects*, edited by M. K. Hughes, T. W. Swetnam and H. F. Diaz, pp. 231-261, Springer Netherlands, Dordrecht.

Meko, D. M., C. W. Stockton, and W. R. Boggess (1995), The Tree-Rring Record of Severe Sustained Drought, *JAWRA Journal of the American Water Resources Association*, *31*(5), 789-801.

Mekonnen, M. M., and A. Y. Hoekstra (2016), Four billion people facing severe water scarcity, *Science Advances*, *2*(2), e1500323.

Melvin, T. M., and K. R. Briffa (2008), A “signal-free” approach to dendroclimatic standardisation, *Dendrochronologia*, *26*(2), 71-86.

Milly, P. C. D., and K. A. Dunne (2020), Colorado River flow dwindles as warming-driven loss of reflective snow energizes evaporation, *Science*, *367*(6483), 1252-1255.

Milly, P. C. D., R. T. Wetherald, K. A. Dunne, and T. L. Delworth (2002), Increasing risk of great floods in a changing climate, *Nature*, *415*(6871), 514-517.

Minora, U., D. Bocchiola, C. D'Agata, D. Maragno, C. Mayer, A. Lambrecht, B. Mosconi, E. Vuillermoz, A. Senese, and C. Compostella (2013), 2001–2010 glacier changes in the Central Karakoram National Park: a contribution to evaluate the magnitude and rate of the" Karakoram anomaly", *The Cryosphere Discussions*, *7*(3), 2891-2941.

Mirza, M. Q. M. (2003), Three Recent Extreme Floods in Bangladesh: A Hydro-Meteorological Analysis, *Nat. Hazards*, *28*(1), 35-64.

Mondal, M. S., M. A. Rahman, N. Mukherjee, H. Huq, and R. Rahman (2015), Hydro-climatic hazards for crops and cropping system in the chars of the Jamuna River and potential adaptation options, *Nat. Hazards*, *76*(3), 1431-1455.

Mukhopadhyay, B., and A. Khan (2014), A quantitative assessment of the genetic sources of the hydrologic flow regimes in Upper Indus Basin and its significance in a changing climate, *J. Hydrol.*, *509*, 549-572.

Myers, C. G., J. L. Oster, W. D. Sharp, R. Bennartz, N. P. Kelley, A. K. Covey, and S. F. M. Breitenbach (2015), Northeast Indian stalagmite records Pacific decadal climate change: Implications for moisture transport and drought in India, *Geophys. Res. Lett.*, *42*(10), 4124-4132.

Nash, J. E., and J. V. Sutcliffe (1970), River flow forecasting through conceptual models part I — A discussion of principles, *J. Hydrol.*, *10*(3), 282-290.

Nepal, S., and A. B. Shrestha (2015), Impact of climate change on the hydrological regime of the Indus, Ganges and Brahmaputra river basins: a review of the literature, *International Journal of Water Resources Development*, *31*(2), 201-218.

Nola, P., M. Morales, R. Motta, and R. Villalba (2006), The role of larch budmoth (Zeiraphera diniana Gn.) on forest succession in a larch (Larix decidua Mill.) and Swiss stone pine (Pinus cembra L.) stand in the Susa Valley (Piedmont, Italy), *Trees*, *20*(3), 371-382.

Oppenheimer, C., et al. (2017), Multi-proxy dating the 'Millennium Eruption' of Changbaishan to late 946 CE, *Quat. Sci. Rev.*, *158*, 164-171.

Orwig, D. A., and M. D. Abrams (1997), Variation in radial growth responses to drought among species, site, and canopy strata, *Trees*, *11*(8), 474-484.

Owen, D. (2017), *Where the Water Goes: Life and Death Along the Colorado River*, Penguin.

Pages Hydro2k Consortium (2017), Comparing proxy and model estimates of hydroclimate variability and change over the Common Era, *Clim. Past*, *13*(12), 1851-1900.

Palazzi, E., J. von Hardenberg, S. Terzago, and A. Provenzale (2014), Precipitation in the Karakoram-Himalaya: a CMIP5 view, *Clim. Dyn.*, 1-25.

Palmer, J. G., E. R. Cook, C. S. Turney, K. Allen, P. Fenwick, B. I. Cook, A. O'Donnell, L. Janice, P. Grierson, and P. Baker (2015), Drought variability in the eastern Australia and New Zealand summer drought atlas (ANZDA, CE 1500–2012) modulated by the Interdecadal Pacific Oscillation, *Environmental Research Letters*, *10*(12), 124002.

Palmer, W. C. (1965), *Meteorological drought*, US Department of Commerce, Weather Bureau Washington, DC, USA.

Pauling, A., J. Luterbacher, C. Casty, and H. Wanner (2006), Five hundred years of gridded high-resolution precipitation reconstructions over Europe and the connection to large-scale circulation, *Clim. Dyn.*, *26*(4), 387-405.

Pausata, F. S. R., C. Karamperidou, R. Caballero, and D. S. Battisti (2016), ENSO response to high-latitude volcanic eruptions in the Northern Hemisphere: The role of the initial conditions, *Geophys. Res. Lett.*, *43*(16), 8694-8702.

Pederson, N., E. R. Cook, G. C. Jacoby, D. M. Peteet, and K. L. Griffin (2004), The influence of winter temperatures on the annual radial growth of six northern range margin tree species, *Dendrochronologia*, *22*(1), 7-29.

Pederson, N., A. E. Hessl, N. Baatarbileg, K. J. Anchukaitis, and N. Di Cosmo (2014), Pluvials, droughts, the Mongol Empire, and modern Mongolia, *Proceedings of the National Academy of Sciences*, *111*(12), 4375-4379.

Plummer, C., M. Curran, T. D. v. Ommen, S. O. Rasmussen, A. Moy, T. Vance, H. B. Clausen, B. M. Vinther, and P. Mayewski (2012), An independently dated 2000-yr volcanic record from Law Dome, East Antarctica, including a new perspective on the dating of the 1450s CE eruption of Kuwae, Vanuatu, *Climate of the Past*, *8*(6), 1929-1940.

Plummer, M. (2003), JAGS: A program for analysis of Bayesian graphical models using Gibbs sampling, paper presented at Proceedings of the 3rd international workshop on distributed statistical computing, Vienna.

Pohl, K. A., K. S. Hadley, and K. B. Arabas (2006), *Decoupling Tree-Ring Signatures of Climate Variation, Fire, and Insect Outbreaks in Central Oregon*, 14 pp., SPIE.

Pranavananda, S. (1939), The Sources of the Brahmaputra, Indus, Sutlej, and Karnali: With Notes on Manasarowar and Rakas Tal, *The Geographical Journal*, *93*(2), 126-135.

Pritchard, H. D. (2019), Asia's shrinking glaciers protect large populations from drought stress, *Nature*, *569*(7758), 649-654.

R Core Team (2017), R: A language and environment for statistical computing. R Foundation for Statistical Computing , Vienna, Austria. URL https://www.R-project.org/.

Raible, C., F. Lehner, J. F. González Rouco, and L. Fernández Donado (2014), Changing correlation structures of the Northern Hemisphere atmospheric circulation from 1000 to 2100 AD, *Climate of the Past*, *10*(2), 537-550.

Rao, M. P., E. R. Cook, B. I. Cook, K. J. Anchukaitis, R. D. D'Arrigo, P. J. Krusic, and A. N. LeGrande (2019), A double bootstrap approach to Superposed Epoch Analysis to evaluate response uncertainty, *Dendrochronologia*, *55*, 119-124.

Rao, M. P., N. K. Davi, R. D D'Arrigo, J. Skees, B. Nachin, C. Leland, B. Lyon, S.-Y. Wang, and O. Byambasuren (2015), Dzuds, droughts, and livestock mortality in Mongolia, *Environmental Research Letters*, *10*(7), 074012.

Rao, M. P., et al. (2017), European and Mediterranean hydroclimate responses to tropical volcanic forcing over the last millennium, *Geophys. Res. Lett.*, *44*(10), 5104-5112.

Rao, M. P., et al. (2018), Six Centuries of Upper Indus Basin Streamflow Variability and Its Climatic Drivers, *Water Resour. Res.*, *54*(8), 5687-5701.

Rashid, M. U., A. Latif, and M. Azmat (2018), Optimizing Irrigation Deficit of Multipurpose Cascade Reservoirs, *Water Resour. Manage.*

Ravindranath, A., N. Devineni, U. Lall, E. R. Cook, G. Pederson, J. Martin, and C. Woodhouse (2019), Streamflow Reconstruction in the Upper Missouri River Basin Using a Novel Bayesian Network Model, *Water Resour. Res.*, *55*(9), 7694-7716.

Riahi, K., S. Rao, V. Krey, C. Cho, V. Chirkov, G. Fischer, G. Kindermann, N. Nakicenovic, and P. Rafaj (2011), RCP 8.5—A scenario of comparatively high greenhouse gas emissions, *Clim. Change*, *109*(1), 33.

Ridley, J., A. Wiltshire, and C. Mathison (2013), More frequent occurrence of westerly disturbances in Karakoram up to 2100, *Sci. Tot. Environ.*, *468*, S31-S35.

Rind, D., N. Balachandran, and R. Suozzo (1992), Climate change and the middle atmosphere. Part II: The impact of volcanic aerosols, *J. Clim.*, *5*(3), 189-208.

Robock, A. (2000), Volcanic eruptions and climate, *Rev. Geophys.*, *38*(2), 191-219.

Ronay, E. R., S. F. M. Breitenbach, and J. L. Oster (2019), Sensitivity of speleothem records in the Indian Summer Monsoon region to dry season infiltration, *Scientific reports*, *9*(1), 5091.

Schneider, T., T. Bischoff, and G. H. Haug (2014), Migrations and dynamics of the intertropical convergence zone, *Nature*, *513*(7516), 45-53.

Schneider, U., P. Finger, A. Meyer-Christoffer, E. Rustemeier, M. Ziese, and A. Becker (2017), Evaluating the Hydrological Cycle over Land Using the Newly-Corrected Precipitation Climatology from the Global Precipitation Climatology Centre (GPCC), *Atmosphere*, *8*(3), 52.

Schoennagel, T., T. T. Veblen, W. H. Romme, J. S. Sibold, and E. R. Cook (2005), ENSO and PDO variability affect drought-induced fire occurance in Rocky Mountain subalpine forests, *Ecol. Appl.*, *15*(6), 2000-2014.

Schrier, G., K. Briffa, P. Jones, and T. Osborn (2006), Summer moisture variability across Europe, *J. Clim.*, *19*(12), 2818-2834.

Schrier, G., J. Barichivich, K. Briffa, and P. Jones (2013), A scPDSI-based global data set of dry and wet spells for 1901–2009, *Journal of Geophysical Research: Atmospheres*, *118*(10), 4025-4048.

Schulman, E. (1942), A Tree-Ring History of Runoff of the Colorado River, 1366-1941, *Report, Bureau of Power and Light, Los Angeles, California*.

Sear, C. B., P. M. Kelly, P. D. Jones, and C. M. Goodess (1987), Global surface-temperature responses to major volcanic eruptions, *Nature*, *330*, 365.

Seneviratne, S. I., D. Lüthi, M. Litschi, and C. Schär (2006), Land–atmosphere coupling and climate change in Europe, *Nature*, *443*(7108), 205-209.

Shah, S. K., A. Bhattacharyya, and V. Chaudhary (2014), Streamflow reconstruction of Eastern Himalaya River, Lachen 'Chhu', North Sikkim, based on tree-ring data of Larix griffithiana from Zemu Glacier basin, *Dendrochronologia*, *32*(2), 97-106.

Shaman, J., M. Cane, and A. Kaplan (2005), The relationship between tibetan snow depth, ENSO, river discharge and the monsoons of Bangladesh, *Int. J. Remote Sens.*, *26*(17), 3735-3748.

Shapiro, S. S., and M. B. Wilk (1965), An analysis of variance test for normality (complete samples)†, *Biometrika*, *52*(3-4), 591-611.

Shawki, D., A. Voulgarakis, A. Chakraborty, M. Kasoar, and J. Srinivasan (2018), The South Asian Monsoon Response to Remote Aerosols: Global and Regional Mechanisms, *Journal of Geophysical Research: Atmospheres*, *123*(20), 11,585-511,601.

Shi, C., et al. (2018a), The response of relative humidity to centennial-scale warming over the southeastern Tibetan Plateau inferred from tree-ring width chronologies, *Clim. Dyn.*, *51*(9), 3735-3746.

Shi, H., B. Wang, E. R. Cook, J. Liu, and F. Liu (2018b), Asian Summer Precipitation over the Past 544 Years Reconstructed by Merging Tree Rings and Historical Documentary Records, *J. Clim.*, *31*(19), 7845-7861.

Shindell, D. T., G. A. Schmidt, M. E. Mann, and G. Faluvegi (2004), Dynamic winter climate response to large tropical volcanic eruptions since 1600, *Journal of Geophysical Research: Atmospheres*, *109*(D5).

Sigl, M., et al. (2013), A new bipolar ice core record of volcanism from WAIS Divide and NEEM and implications for climate forcing of the last 2000 years, *Journal of Geophysical Research: Atmospheres*, *118*(3), 1151-1169.

Sigl, M., et al. (2015), Timing and climate forcing of volcanic eruptions for the past 2,500 years, *Nature*, *523*(7562), 543-549.

Sinha, A., G. Kathayat, H. Cheng, S. F. M. Breitenbach, M. Berkelhammer, M. Mudelsee, J. Biswas, and R. L. Edwards (2015), Trends and oscillations in the Indian summer monsoon rainfall over the last two millennia, *Nature Communications*, *6*(1), 6309.

Smith, T., and B. Bookhagen (2018), Changes in seasonal snow water equivalent distribution in High Mountain Asia (1987 to 2009), *Science Advances*, *4*(1), e1701550.

Sobkowiak, L., A. Perz, D. Wrzesiński, and M. A. Faiz (2020), Estimation of the River Flow Synchronicity in the Upper Indus River Basin Using Copula Functions., *Sustainability*, *12*(12), 5122.

Speer, J. H., S. K. Shah, C. Truettner, A. Pacheco, M. F. Bekker, D. Dukpa, E. R. Cook, and K. Tenzin (2019), Flood history and river flow variability recorded in tree rings on the Dhur River, Bhutan, *Dendrochronologia*, *56*, 125605.

St. George, S., and T. R. Ault (2014), The imprint of climate within Northern Hemisphere trees, *Quat. Sci. Rev.*, *89*, 1-4.

Stahle, D. W., et al. (2016), The Mexican Drought Atlas: Tree-ring reconstructions of the soil moisture balance during the late pre-Hispanic, colonial, and modern eras, *Quat. Sci. Rev.*, *149*, 34-60.

Steinschneider, S., E. R. Cook, K. R. Briffa, and U. Lall (2017), Hierarchical regression models for dendroclimatic standardization and climate reconstruction, *Dendrochronologia*, *44*, 174-186.

Stine, A. R. (2019), Global Demonstration of Local Liebig's Law Behavior for Tree-Ring Reconstructions of Climate, *Paleoceanography and Paleoclimatology*, *34*(2), 203-216.

Stockton, C., and G. C. Jacoby (1976), Long-term surface-water supply and streamflow trends in the Upper Colorado River Basin, Lake Powell Res. Proj, *Bull*, *18*.

Stockton, C. W. (1971), The feasibility of augmenting hydrologic records using tree-ring data, edited, The University of Arizona.

Stoffel, M., et al. (2015a), Estimates of volcanic-induced cooling in the Northern Hemisphere over the past 1,500 years, *Nature Geosci*, *8*(10), 784-788.

Stoffel, M., et al. (2015b), Estimates of volcanic-induced cooling in the Northern Hemisphere over the past 1,500 years, *Nat. Geosci.*, *8*, 784.

Swetnam, T. W. (1993), Fire History and Climate Change in Giant Sequoia Groves, *Science*, *262*(5135), 885-889.

Swetnam, T. W., and J. L. Betancourt (1998), Mesoscale Disturbance and Ecological Response to Decadal Climatic Variability in the American Southwest, *J. Clim.*, *11*(12), 3128-3147.

Swetnam, T. W., J. Farella, C. I. Roos, M. J. Liebmann, D. A. Falk, and C. D. Allen (2016), Multiscale perspectives of fire, climate and humans in western North America and the Jemez Mountains, USA, *Philosophical Transactions of the Royal Society B: Biological Sciences*, *371*(1696), 20150168.

Tahir, A. A., P. Chevallier, Y. Arnaud, L. Neppel, and B. Ahmad (2011), Modeling snowmelt-runoff under climate scenarios in the Hunza River basin, Karakoram Range, Northern Pakistan, *J. Hydrol.*, *409*(1), 104-117.

Tan, L., et al. (2019), Rainfall variations in central Indo-Pacific over the past 2,700 y, *Proceedings of the National Academy of Sciences*, *116*(35), 17201-17206.

Taylor, B. L., T. Gal-Chen, and S. H. Schneider (1980), Volcanic eruptions and long-term temperature records: An empirical search for cause and effect, *Q. J. Roy. Meteorol. Soc.*, *106*(447), 175-199.

Taylor, K. E., R. J. Stouffer, and G. A. Meehl (2012), An Overview of CMIP5 and the Experiment Design, *Bull. Am. Meteorol. Soc.*, *93*(4), 485-498.

Thapa, U., S. St. George, D. Kharal, and N. Gaire (2017), Tree growth across the Nepal Himalaya during the last four centuries, *Progress in Physical Geography: Earth and Environment*, *41*(4), 478-495.

Thomas, P. J., N. Juyal, V. S. Kale, and A. K. Singhvi (2007), Luminescence chronology of late Holocene extreme hydrological events in the upper Penner River basin, South India, *J. Quat. Sci.*, *22*(8), 747-753.

Tingley, M. P., and P. Huybers (2010), A Bayesian Algorithm for Reconstructing Climate Anomalies in Space and Time. Part II: Comparison with the Regularized Expectation–Maximization Algorithm, *J. Clim.*, *23*(10), 2782-2800.

Toohey, M., and M. Sigl (2017), Volcanic stratospheric sulfur injections and aerosol optical depth from 500 BCE to 1900 CE, *Earth Syst. Sci. Data*, *9*(2), 809-831.

Trouet, V., F. Babst, and M. Meko (2018), Recent enhanced high-summer North Atlantic Jet variability emerges from three-century context, *Nature Communications*, *9*(1), 180.

Trouet, V., A. H. Taylor, E. R. Wahl, C. N. Skinner, and S. L. Stephens (2010), Fire-climate interactions in the American West since 1400 CE, *Geophys. Res. Lett.*, *37*(4).

Turner, A. G., and H. Annamalai (2012), Climate change and the South Asian summer monsoon, *Nature Climate Change*, *2*, 587.

Uhe, P. F., D. M. Mitchell, P. D. Bates, C. C. Sampson, A. M. Smith, and A. S. Islam (2019), Enhanced flood risk with 1.5 °C global warming in the Ganges–Brahmaputra–Meghna basin, *Environmental Research Letters*, *14*(7), 074031.

van der Schrier, G., J. Barichivich, K. R. Briffa, and P. D. Jones (2013), A scPDSI-based global data set of dry and wet spells for 1901–2009, *Journal of Geophysical Research: Atmospheres*, *118*(10), 4025-4048.

Vinod, H. (2006), Maximum entropy ensembles for time series inference in economics, *Journal of Asian Economics*, *17*(6), 955-978.

Vinod, H., and J. López-de-Lacalle (2009), Maximum Entropy Bootstrap for Time Series: The meboot R Package, *Journal of Statistical Software*, *029*(i05).

Wang, J., B. Yang, and F. C. Ljungqvist (2020), Moisture and Temperature Covariability over the Southeastern Tibetan Plateau during the Past Nine Centuries, *J. Clim.*, *0*(0), null.

Wanliss, J., G. Cornélissen, F. Halberg, D. Brown, and B. Washington (2018), Superposed epoch analysis of physiological fluctuations: possible space weather connections, *International Journal of Biometeorology*, *62*(3), 449-457.

Webster, P. J., J. Jian, T. M. Hopson, C. D. Hoyos, P. A. Agudelo, H.-R. Chang, J. A. Curry, R. L. Grossman, T. N. Palmer, and A. R. Subbiah (2010), Extended-Range Probabilistic Forecasts of Ganges and Brahmaputra Floods in Bangladesh, *Bull. Am. Meteorol. Soc.*, *91*(11), 1493-1514.

Wegmann, M., S. Brönnimann, J. Bhend, J. Franke, D. Folini, M. Wild, and J. Luterbacher (2014), Volcanic Influence on European Summer Precipitation through Monsoons: Possible Cause for "Years without Summer"*, *J. Clim.*, *27*(10), 3683-3691.

Westerling, A. L., A. Gershunov, T. J. Brown, D. R. Cayan, and M. D. Dettinger (2003), Climate and Wildfire in the Western United States, *Bull. Am. Meteorol. Soc.*, *84*(5), 595-604.

Whitehead, P. G., et al. (2015), Impacts of climate change and socio-economic scenarios on flow and water quality of the Ganges, Brahmaputra and Meghna (GBM) river systems: low flow and flood statistics, *Environmental Science: Processes & Impacts*, *17*(6), 1057-1069.

Wigley, T. M., K. R. Briffa, and P. D. Jones (1984), On the average value of correlated time series, with applications in dendroclimatology and hydrometeorology, *J. Clim. Appl. Meteorol.*, *23*(2), 201-213.

Wijngaard, R. R., A. F. Lutz, S. Nepal, S. Khanal, S. Pradhananga, A. B. Shrestha, and W. W. Immerzeel (2017), Future changes in hydro-climatic extremes in the Upper Indus, Ganges, and Brahmaputra River basins, *PLOS ONE*, *12*(12), e0190224.

Wilhelm, B., et al. (2019), Interpreting historical, botanical, and geological evidence to aid preparations for future floods, *WIREs Water*, *6*(1), e1318.

Wilson, R., et al. (2016), Last millennium northern hemisphere summer temperatures from tree rings: Part I: The long term context, *Quat. Sci. Rev.*, *134*, 1-18.

Winsemius, H. C., L. P. H. Van Beek, B. Jongman, P. J. Ward, and A. Bouwman (2013), A framework for global river flood risk assessments, *Hydrol. Earth Syst. Sci.*, *17*(5), 1871-1892.

Winsemius, H. C., et al. (2016), Global drivers of future river flood risk, *Nature Climate Change*, *6*(4), 381-385.

Woodhouse, C. (1993), Tree-growth response to ENSO events in the Central Colorado Front Range, *Physical Geography*, *14*(5), 417-435.

Woodhouse, C. A., and J. J. Lukas (2006), Multi-century tree-ring reconstructions of Colorado streamflow for water resource planning, *Clim. Change*, *78*(2-4), 293-315.

Woodhouse, C. A., D. M. Meko, G. M. MacDonald, D. W. Stahle, and E. R. Cook (2010), A 1,200-year perspective of 21st century drought in southwestern North America, *Proceedings of the National Academy of Sciences*, *107*(50), 21283-21288.

Woodhouse, C. A., J. Lukas, K. Morino, D. Meko, and K. Hirschboeck (2016a), Using the past to plan for the future? The value of paleoclimate reconstructions for water resource planning, *Water Policy and Planning in a Variable and Changing Climate*, 161-182.

Woodhouse, C. A., G. T. Pederson, K. Morino, S. A. McAfee, and G. J. McCabe (2016b), Increasing influence of air temperature on upper Colorado River streamflow, *Geophys. Res. Lett.*, *43*(5), 2174-2181.

Wright, W., J. Li, K. Fang, Y. Tao, and E. R. Cook (2011), NOAA/WDS Paleoclimatology - Wright - Shangri La - ABFO - ITRDB CHIN026, *NOAA National Centers for Environmental Information*.

Xu, H., Y. Song, Y. Goldsmith, and Y. Lang (2019), Meridional ITCZ shifts modulate tropical/subtropical Asian monsoon rainfall, *Science Bulletin*, *64*(23), 1737-1739.

Xu, H., et al. (2016), Hydroclimatic contrasts over Asian monsoon areas and linkages to tropical Pacific SSTs, *Scientific reports*, *6*(1), 33177.

Yang, B., C. Qin, J. Wang, M. He, T. M. Melvin, T. J. Osborn, and K. R. Briffa (2014), A 3,500-year tree-ring record of annual precipitation on the northeastern Tibetan Plateau, *Proceedings of the National Academy of Sciences*, *111*(8), 2903-2908.

Yatagai, A., K. Kamiguchi, O. Arakawa, A. Hamada, N. Yasutomi, and A. Kitoh (2012), APHRODITE: Constructing a Long-Term Daily Gridded Precipitation Dataset for Asia Based on a Dense Network of Rain Gauges, *Bull. Am. Meteorol. Soc.*, *93*(9), 1401-1415.

Zafar, M. U., M. Ahmed, M. A. Farooq, M. Akbar, and A. Hussain (2010), Standardized tree ring chronologies of Picea smithiana from two new sites of Northern area Pakistan, *World Appl Sci J*, *11*(12), 1531-1536.

Zafar, M. U., M. Ahmed, M. P. Rao, B. M. Buckley, N. Khan, M. Wahab, and J. Palmer (2015), Karakorum temperature out of phase with hemispheric trends for the past five centuries, *Clim. Dyn.*, 1-10.

Zambri, B., A. N. LeGrande, A. Robock, and J. Slawinska (2017), Northern Hemisphere winter warming and summer monsoon reduction after volcanic eruptions over the last millennium, *Journal of Geophysical Research: Atmospheres*, *122*(15), 7971-7989.

Zanchettin, D., C. Timmreck, M. Toohey, J. H. Jungclaus, M. Bittner, S. J. Lorenz, and A. Rubino (2019), Clarifying the Relative Role of Forcing Uncertainties and Initial-Condition Unknowns in Spreading the Climate Response to Volcanic Eruptions, *Geophys. Res. Lett.*, *46*(3), 1602-1611.

Zanchettin, D., C. Timmreck, H.-F. Graf, A. Rubino, S. Lorenz, K. Lohmann, K. Krüger, and J. Jungclaus (2012), Bi-decadal variability excited in the coupled ocean–atmosphere system by strong tropical volcanic eruptions, *Clim. Dyn.*, *39*(1-2), 419-444.

Zanchettin, D., C. Timmreck, O. Bothe, S. J. Lorenz, G. Hegerl, H. F. Graf, J. Luterbacher, and J. H. Jungclaus (2013), Delayed winter warming: A robust decadal response to strong tropical volcanic eruptions?, *Geophys. Res. Lett.*, *40*(1), 204-209.

Zawahri, N. A. (2009), India, Pakistan and cooperation along the Indus River system, *Water Policy*, *11*(1), 1-20.

Appendix A

Table A.1 Details of tree-ring sites and series. ABPI - ***Abies pindrow*****, JUEX -** ***Juniperus excelsa*****, CDDE-** ***Cedrus deodara*****, PCSM-** ***Picea smithiana*****, PIGE-** ***Pinus gerardiana*****, PIWA-** ***Pinus wallichiana*****. Model I - series used are predictor for the Partab Bridge reconstruction (total – 15); Model II - series used as predictor for HBR reconstruction at Doyian, Kachora, and Gilgit (total 10).**

Site	Species	Start	Stop	Lat	Lon	Full Name	Lag	Model
ASTABP	ABPI	1505	2005	35.2	74.48	Astore-Rama	t 0	I&II
BUKCDD	CDDE	1411	2006	35.41	71.38	Kalash Valley Bumburet	t 0	I&II
BUKPIG	PIGE	1403	2006	35.41	71.38	Kalash Valley Bumburet	t 0	I&II
CGPCDD	CDDE	1537	2006	35.54	71.44	Chitral-Gol NP	t 0	I
CHEPCS	PCSM	1394	2005	35.02	74.35	Chera (Gilgit)	t 0	I&II
DskJUE	JUEX	1290	2007	35.27	74.47	Dashkin 3150M	t 0	I&II
ISBCDD	CDDE	1511	2006	35.50	74.30	Islam Baiky	t 0	II
JUTPCS	PCSM	1523	2008	35.50	74.20	Jutial (Gilgit) 3250M	t 0	I&II
KARPCS	PCSM	1574	2008	35.53	74.11	Kargah (Gilgit)	t 0	I
MSFCDD	CDDE	1296	2007	35.30	74.05	Mushfar Gilgit	t 0	I&II
MUAABP	ABPI	1678	2005	34.02	73.23	Muree-Ayube	t+1	I
MUSPIW	PIWA	1730	2007	35.30	74.45	Mushkin	t 0	I
MUSPIG	PIGE	1362	2007	35.30	74.45	Mushkin	t 0	II
NLTPCS	PCSM	1387	2005	36.09	74.11	Naltar Gilgit	t 0	I & II
NLTPCS	PCSM	1387	2005	36.09	74.11	Naltar Gilgit	t+1	I
TANCDD	CDDE	1661	2008	35.39	73.32	Tangir, Diamer, 2329m	t 0	I
SHEPCS	PCSM	1663	2006	35.02	71.32	Sheshan (Dangam District) 25	t 0	I

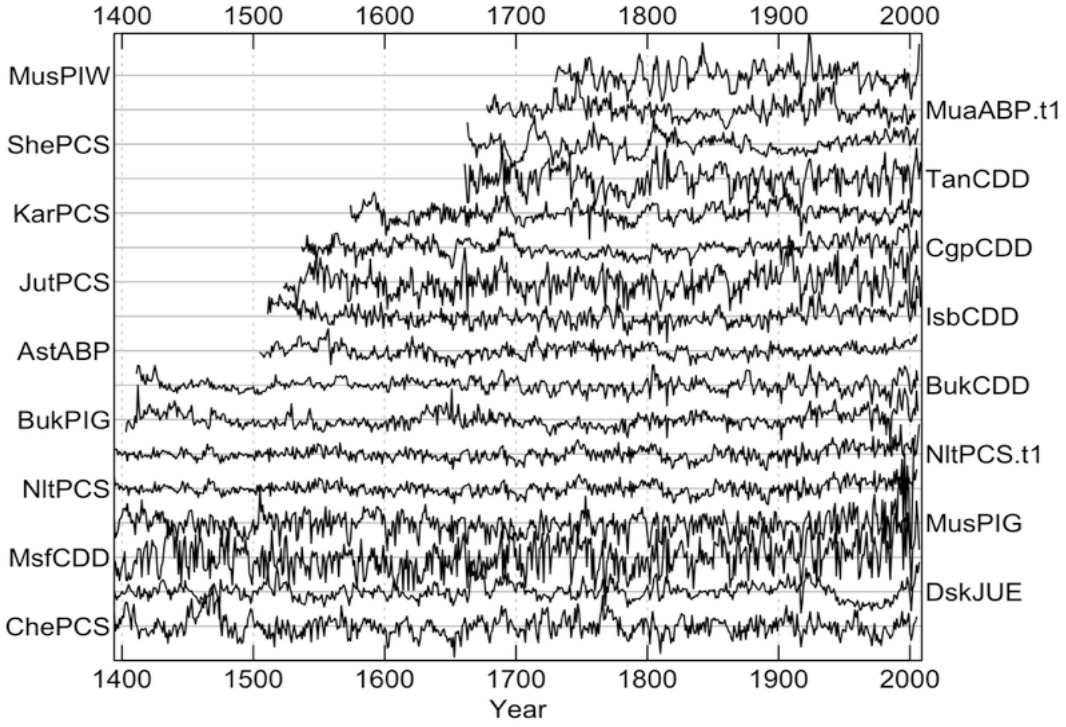

Figure A.1 Standardized tree-ring series used in final predictor suite for the reconstruction models. Of these, MusPIW, MuaABP.t1, ShePCS, TanCDD, KarPCS, CgpCDD, NltPCS.t1 were used only for the reconstruction of May-September (MJJAS) flow at Partab Bridge (Model I) and not in the HBR model (Model II) IsbCDD was only used in the HBR model and not used for the Partab Bridge reconstruction. '.t1' indicates a predictor used with a one-year lag. See Table 2 for more details; made using dplR (Bunn, 2010).

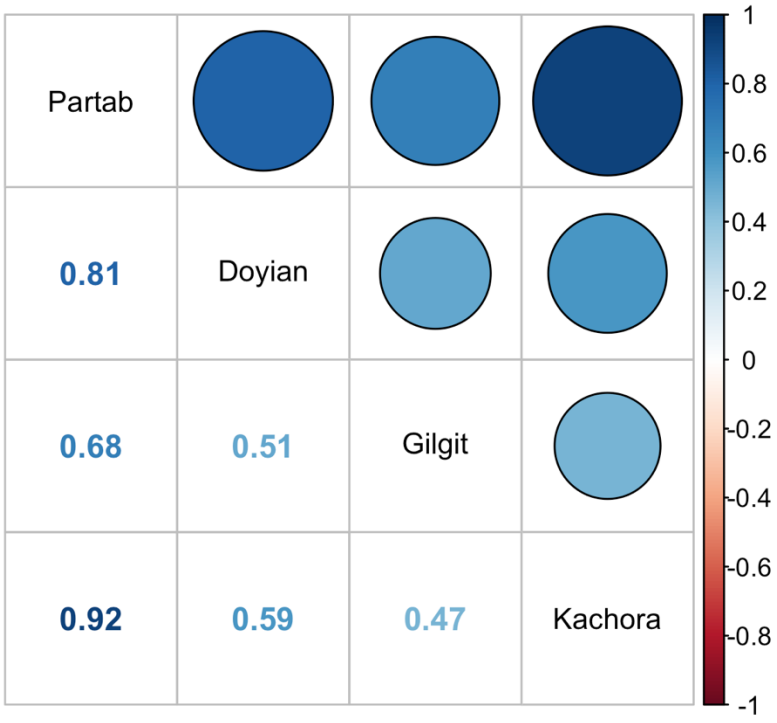

Figure A.2 Correlation matrix of mean annual discharge at the four streamflow gauges. Cross-correlations are calculated for the time period of longest pairwise overlap. Streamflow at Gilgit between 1960-1972 is excluded from the cross-correlations.

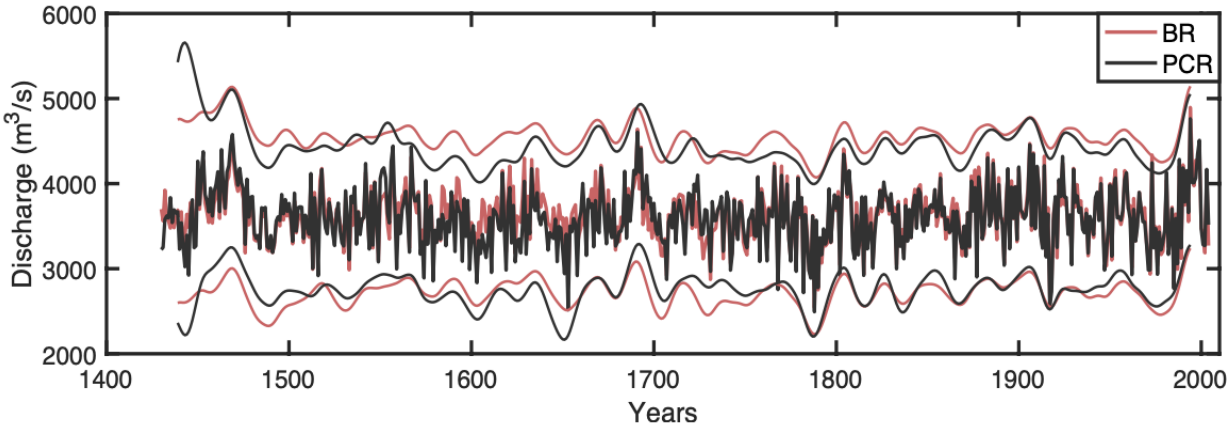

Figure A.3 Mean MJJAS reconstructed discharge (m^3/s) between 1430-2004 C.E. at Partab Bridge using PCR (black) and BR (red). For PCR the uncertainty intervals are 5th and 95th percentile from n=300 MEBoot pseudo-reconstructions, while for BR the 5th and 95th credible intervals are computed from the posterior probability density of the reconstructed flow for each year. Credible intervals are low-pass filtered at 20 years. The two reconstructions correlate at r=0.91 over the 575 years.

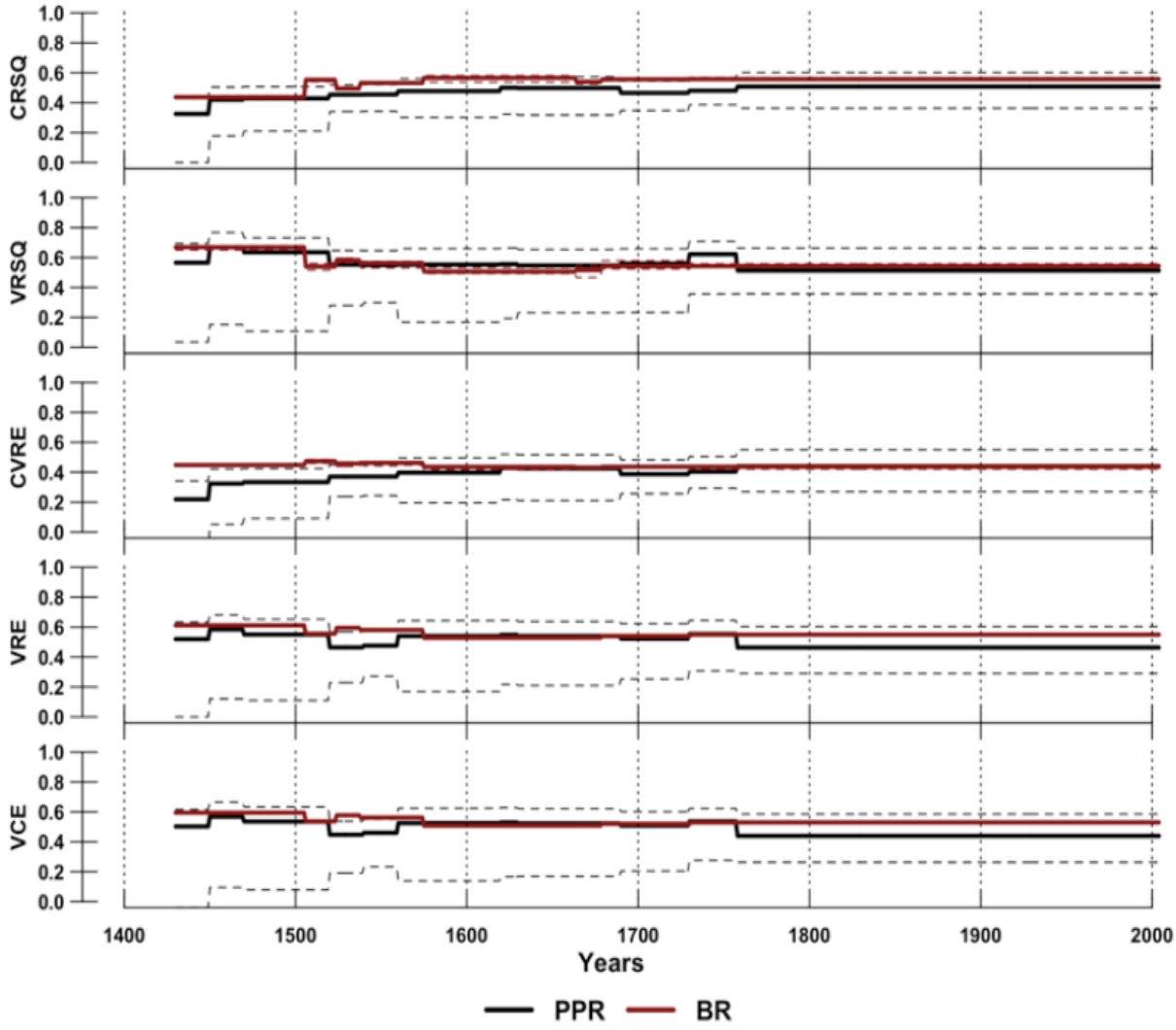

Figure A.4 Calibration and verification period statistics for PCR (black) and BR (red) reconstructions of MJJAS mean discharge at Partab Bridge.

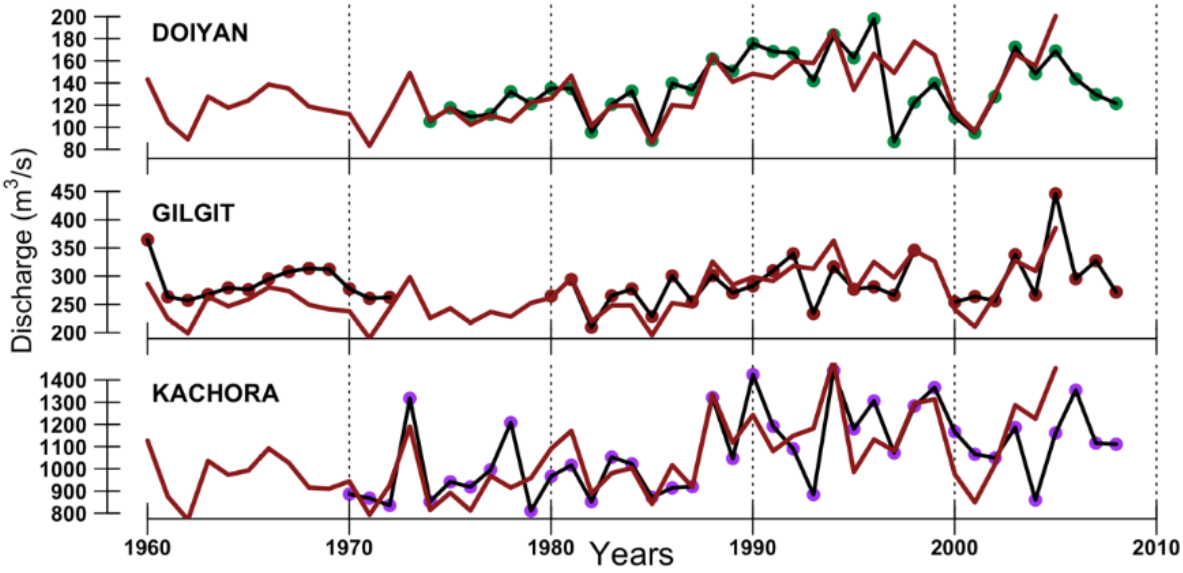

Figure A.5 Annual discharge (m^3/s) at Doyian, Kachora, and Gilgit (black) along with the HBR model predicted discharge at each gauge (red) between 1960-2008. Note that the early portion of the Gilgit data between 1960-1972 was not used in the model calibration.

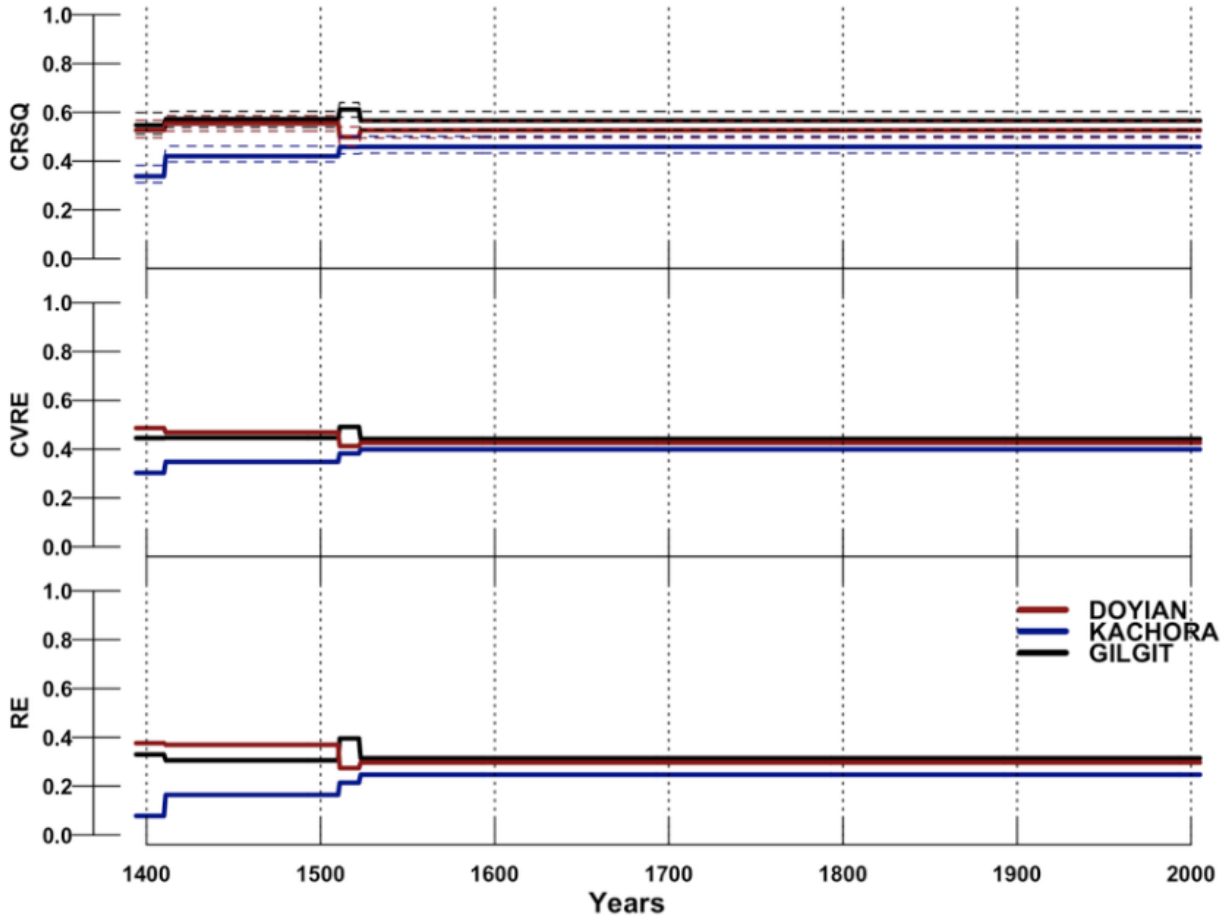

Figure A.6 Calibration and verification period statistics for HBR reconstruction of annual streamflow for each nest between 1394-2004 C.E. at Doyian, Kachora, and Gilgit.

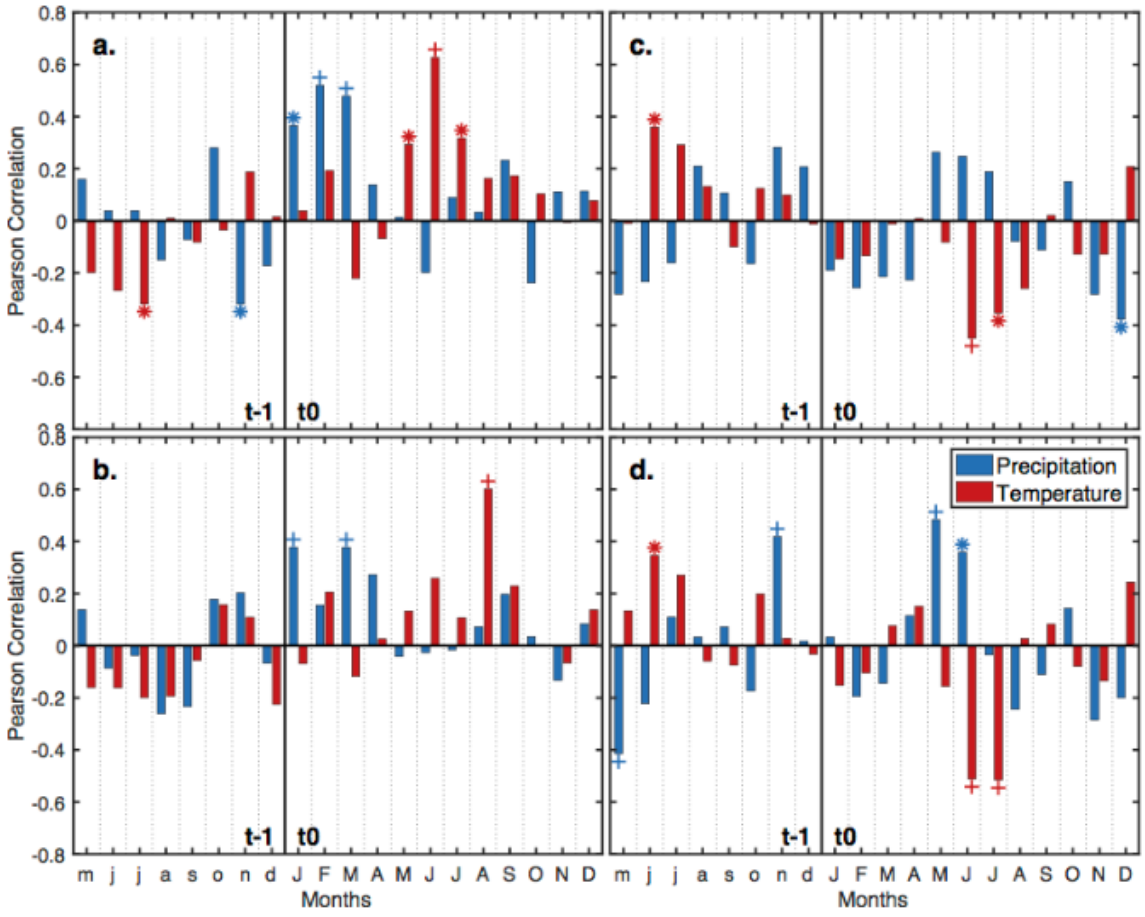

Figure A.7 Same as Figure 1.7, but for a.) May-July (MJJ) mean discharge at Partab-Bridge (1962-2008), b.) August-September (AS) discharge at Partab-Bridge (1962-2008), c.) PC3 time series of the predictor suite of the first nest (1962-2004), and d.) PC4 time series of the predictor nest (1962-2004).

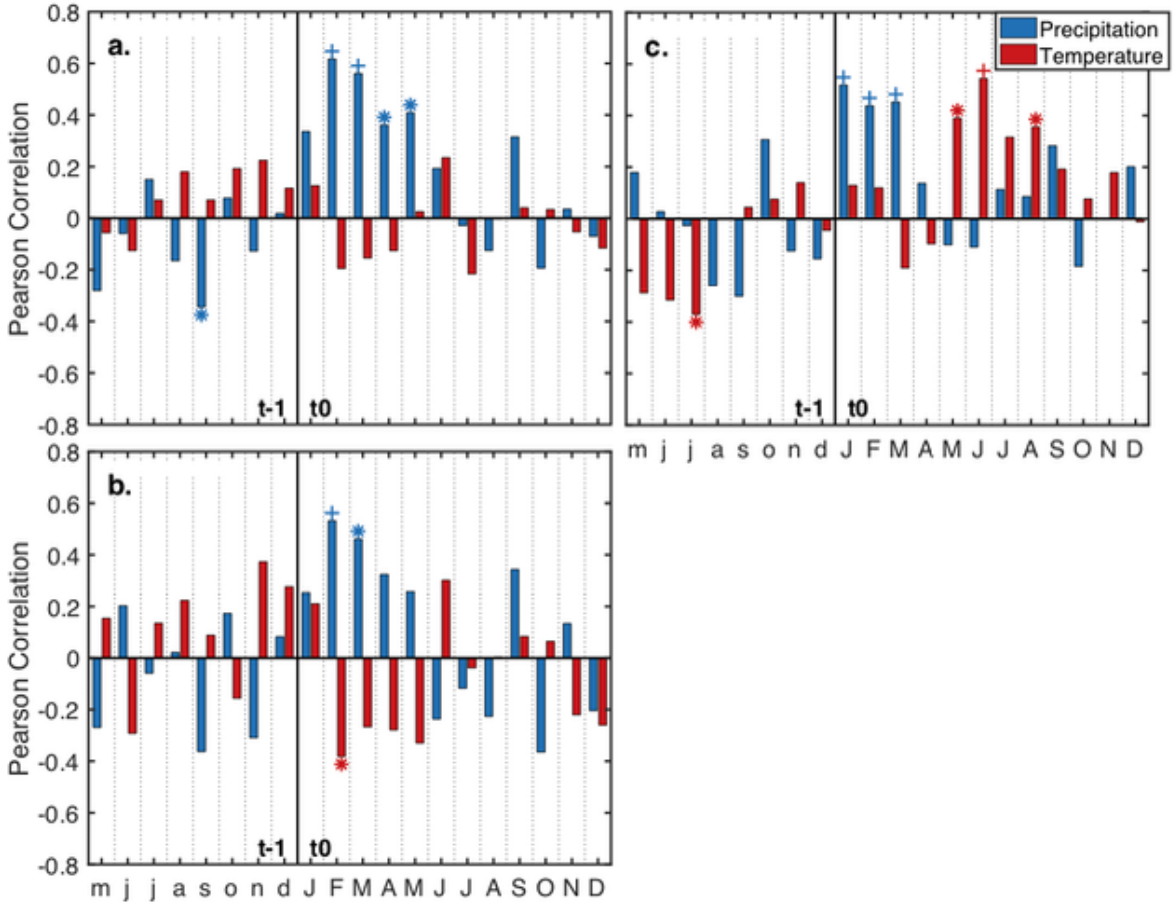

Figure A.8 Same as figure 1.7, but for mean MJJAS discharge at a.) Doyian (1974-2008, n=35), b.) Gilgit (1980-2004, n=27) and c.) Kachora (1970-2008, n=38).

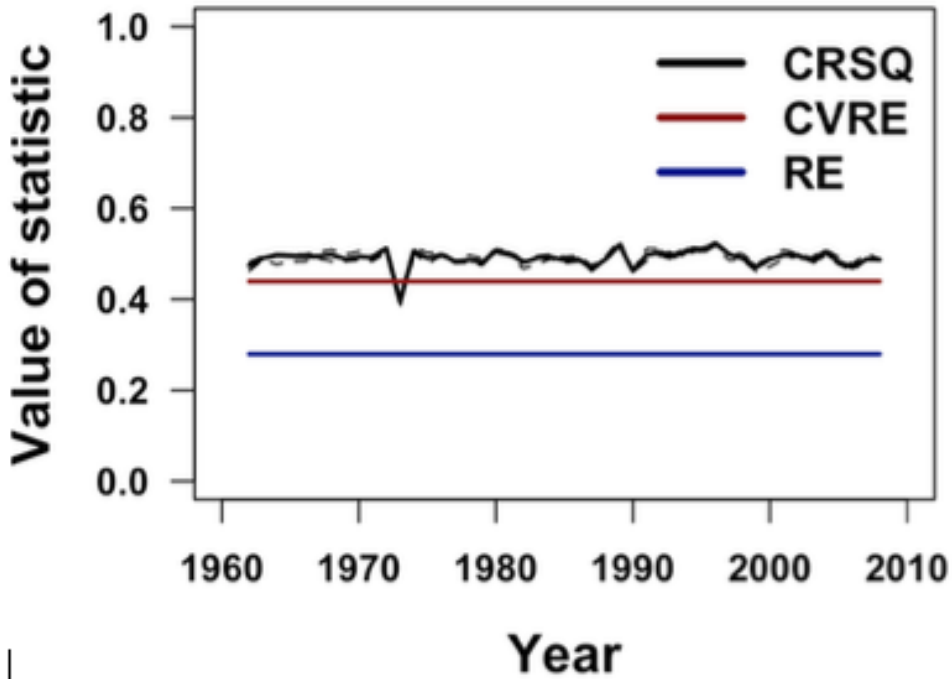

Figure A.9 Calibration and verification period statistics for climate variable informed multiple regression model to predict MJJAS mean discharge at Partab Bridge. Climate variable used as predictors are January through March (JFM) mean precipitation and MJJAS mean temperature.

Appendix B

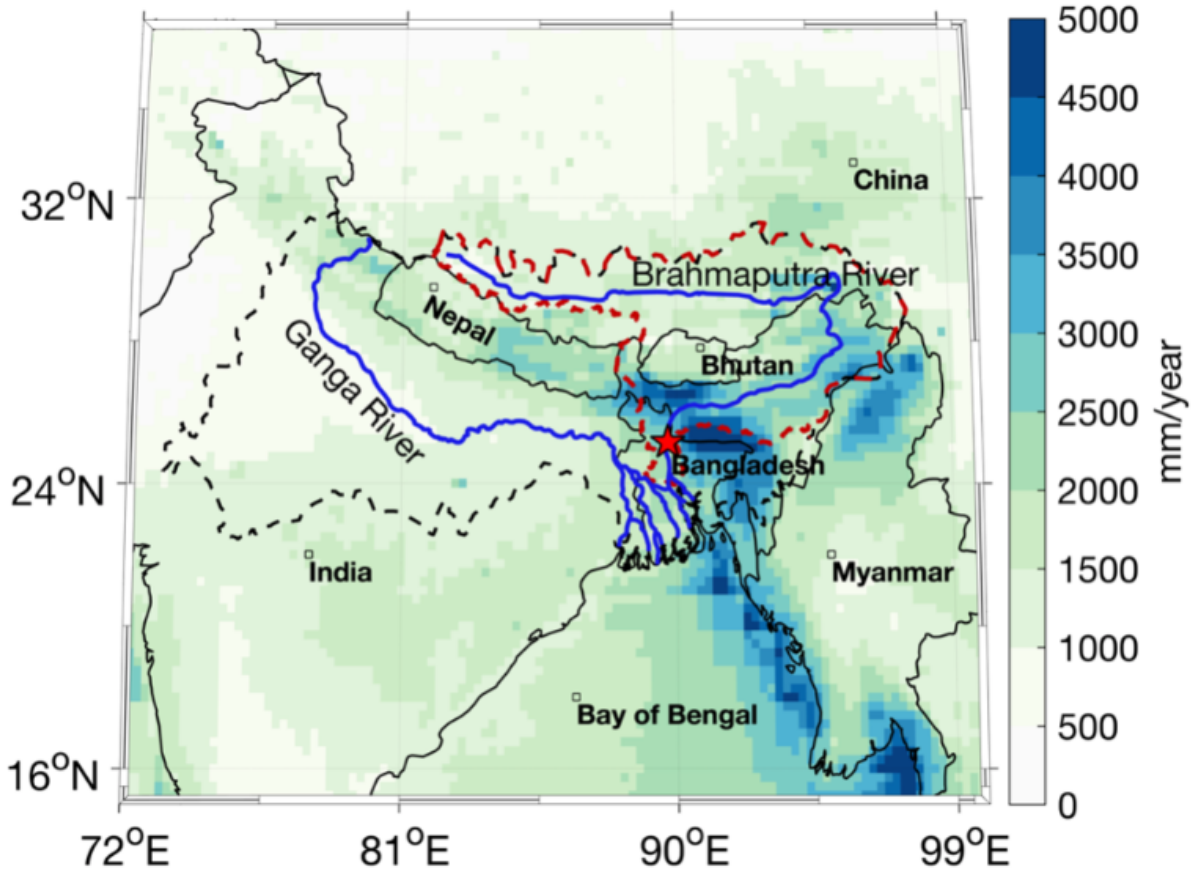

Figure B.1 Mean annual precipitation averaged between 2001 and 2015 as estimated by the TRMM dataset (mm/year) showing the high annual precipitation amounts in the Brahmaputra River watershed. The larger Ganga-Brahmaputra-Meghna watershed is demarcated as black dashed lines while the boundaries of the Brahmaputra watershed are demarcated using red dashed lines. The red star is the location of the Bahadurabad streamflow gauge in the Bangladesh. TRMM – Tropical Rainfall Monitoring Mission [*Huffman et al.*, 2007].

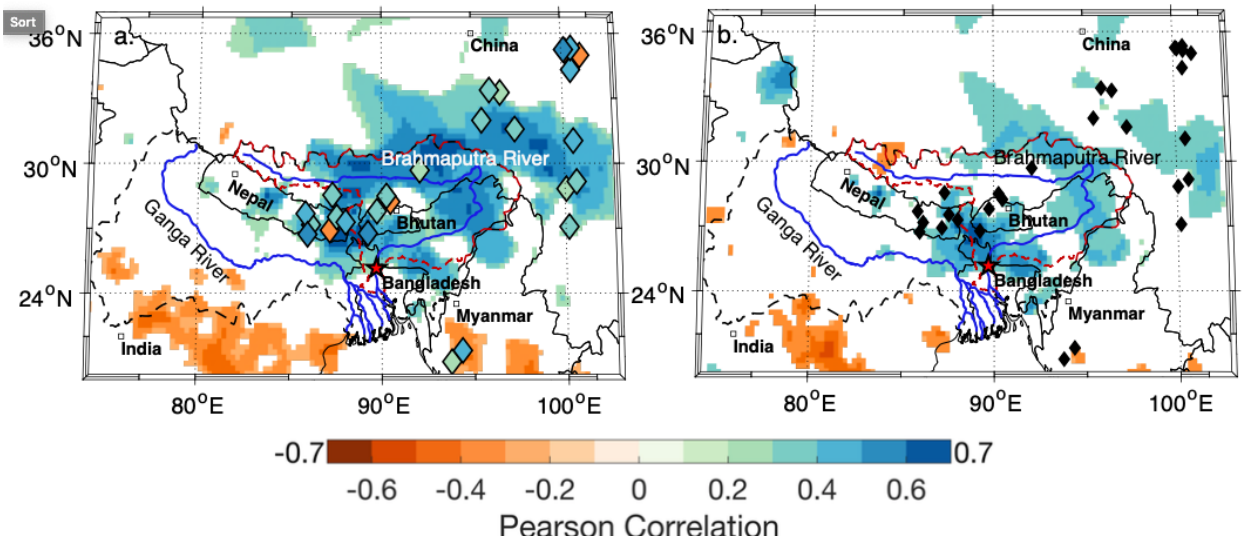

Figure B.2 Same as Figure 2.1 except that the shading on the map represents the spatial field correlation between (a) July-August-September (JAS) discharge at the Bahadurabad gauge and mean JAS precipitation from the GPCC v2018 dataset[*Schneider et al.*, 2017] between 1956-2011 C.E., and (b) the first principal component (PC1) of the 28 tree ring predictors (variance explained: 24.86%) and mean JAS GPCC precipitation (1956-1998 C.E.). These correlations are slightly weaker than those found in Figure 2.1 against CRU precipitation but are consistent with its both Brahmaputra JAS flow at Bahadurabad and our tree ring predictor network being sensitive to upper basin precipitation. The shading in the diamonds in a. represents the correlation of each tree-ring predictor series with mean JAS discharge at Bahadurabad between 1956-2011 C.E. These remain same as in Figure 2.1. Only correlations significant at $p<0.05$ using a 2-sided t-test are shown. Note that the locations of tree ring predictors are jittered for display.

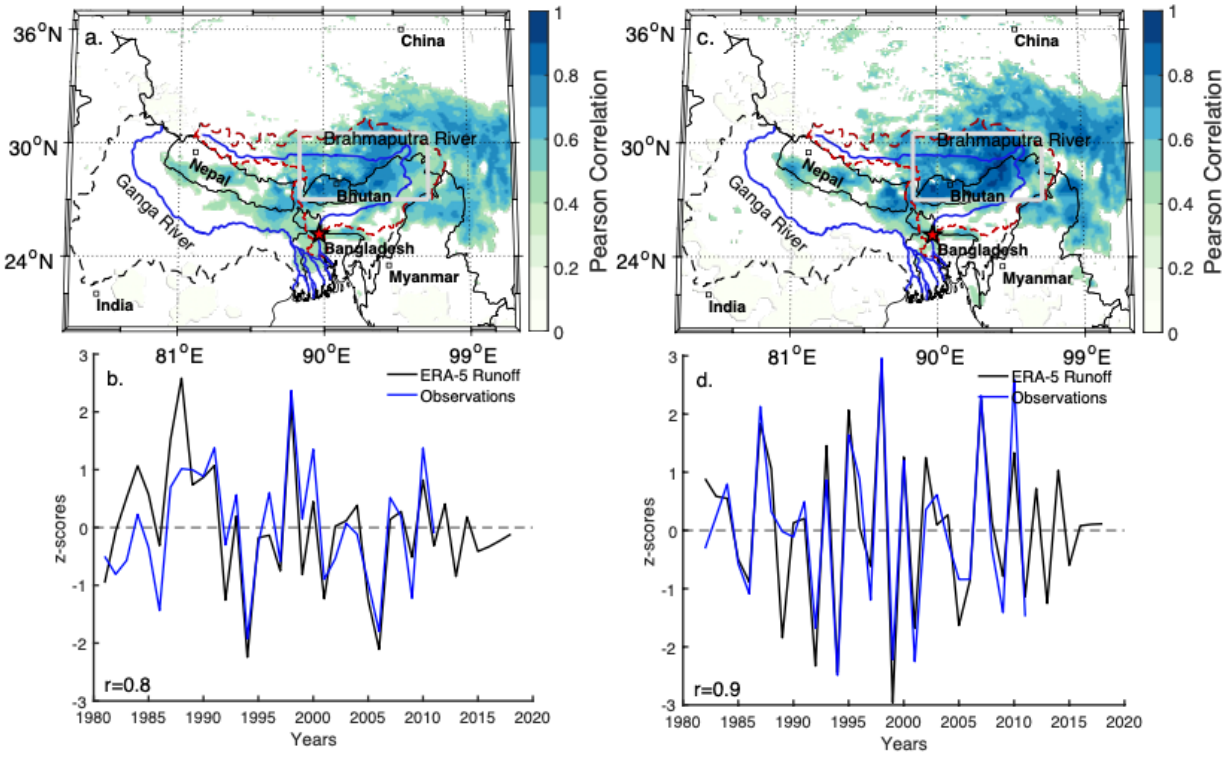

Figure B.3 Pearson correlation between mean JAS discharge at the Bahadurabad gauge, Bangladesh, and ERA-5 reanalysis modelled JAS runoff between 1981-2011 C.E. (31 years). Correlations are calculated using discharge and modelled runoff data (a & b), and using first-differenced discharge and runoff data (c & d). For the timeseries comparisons in c and d ERA-5 modelled runoff was averaged in the grey shaded box shown in a and b spanning the upper basin. ERA-5 runoff is modelled as the sum of surface and sub-ground runoff and is driven primarily by precipitation, melting snow, and soil storage in the model formulation. The high correlations between discharge at Bahadurabad and independent estimates of runoff from a hydrologic model driven using climate variables validates the robustness of the discharge data and that lower basin discharge at Bahadurabad is driven by upper basin runoff (that is in turn controlled by upper basin precipitation - see Figure 1.1 and Figure B. 2). Only correlations significant at $p<0.05$ using a 2-sided t-test are shown.

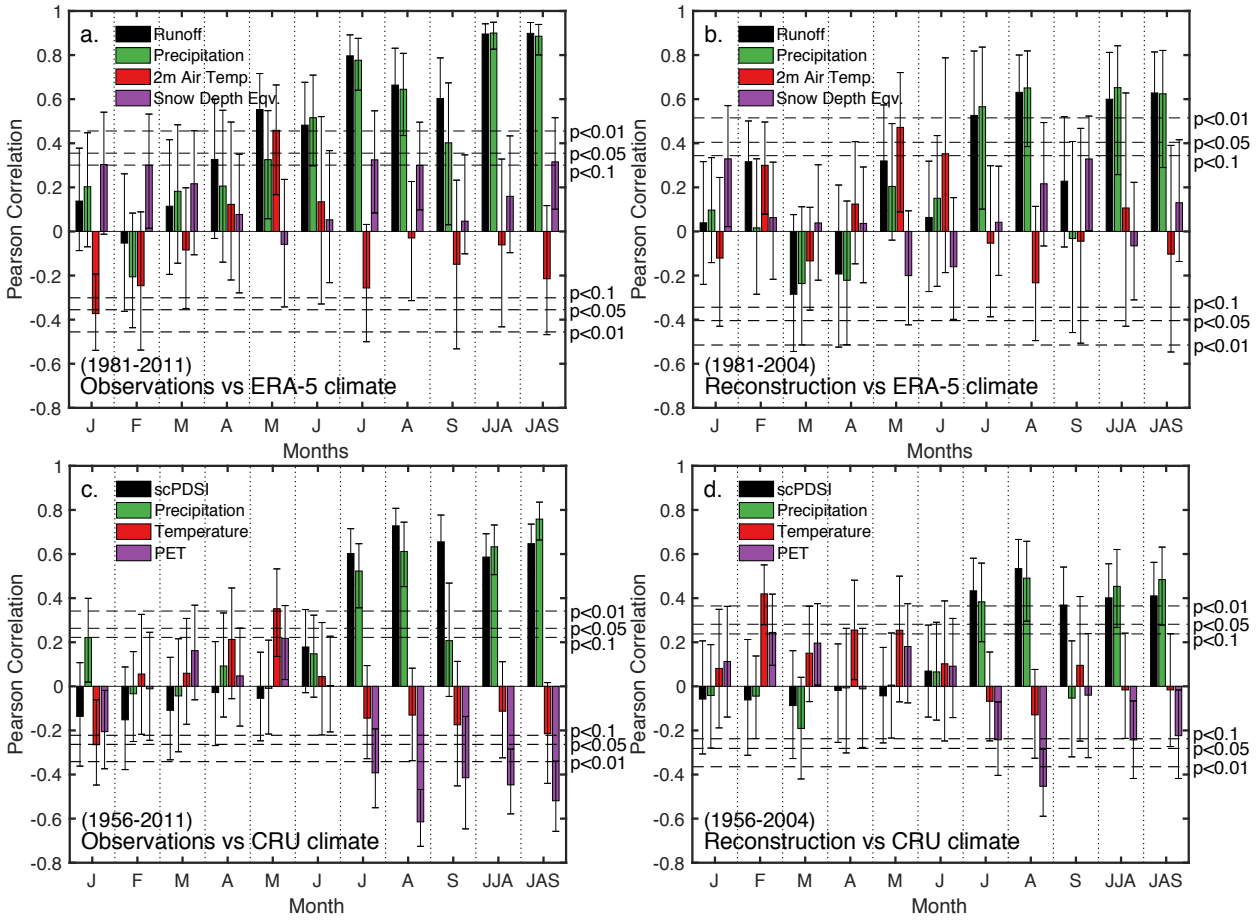

Figure B.4 Correlation response function plot for mean July-September (JAS) instrumental and reconstructed discharge of the Brahmaputra River at Bahadurabad, Bangladesh against upper basin (88.5-96.5°E and 27-30.5°N) monthly climate variables from the ERA-5 (parts a-b) CRU (parts c-d) datasets. This is the same region for which ERA-5 simulated runoff was averaged in Supplementary Fig. S3 (grey box), to compare simulated upper basin runoff against observations of discharge at Bahadurabad, Bangladesh. The climate variables used from the ERA-5 dataset (parts a-b) include monthly simulated runoff, precipitation, 2m air temperature, and snow depth equivalent averaged over the upper basin. The climate variables from the CRU dataset include scPDSI, precipitation, temperature, and potential evapotranspiration (PET) also averaged over the upper basin. The left panels (a and c) are for instrumental observations between 1981-2011 and 1956-2011 respectively. The right panels (b and d) are for reconstructed discharge between 1981-2004 and 1956-2004 respectively. The six horizontal dashed lines in each plot indicate three different thresholds for each monthly correlation to be statistically significant using a 2-tailed t-test. The median correlation and the error bars around each correlation bar are computed from 1,000 bootstrapped draws with replacement from the observed/reconstructed discharge series and the climate series. The last two columns of each subplot are the correlation between mean JAS observed/reconstructed discharge and mean upper basin climate averaged between July-August (JJA) and JAS.

Both instrumental observations and the reconstruction of JAS discharge correlate significantly with upper basin precipitation in the months of June-August (JJA) and July-September (JAS) for the ERA-5 and CRU climate datasets ($p<0.01$). However, these relationships are weaker for reconstructed discharge than for instrumental discharge (right vs left panels). scPDSI - self calibrating Palmer Drought Severity Index[*van der Schrier et al.*, 2013].

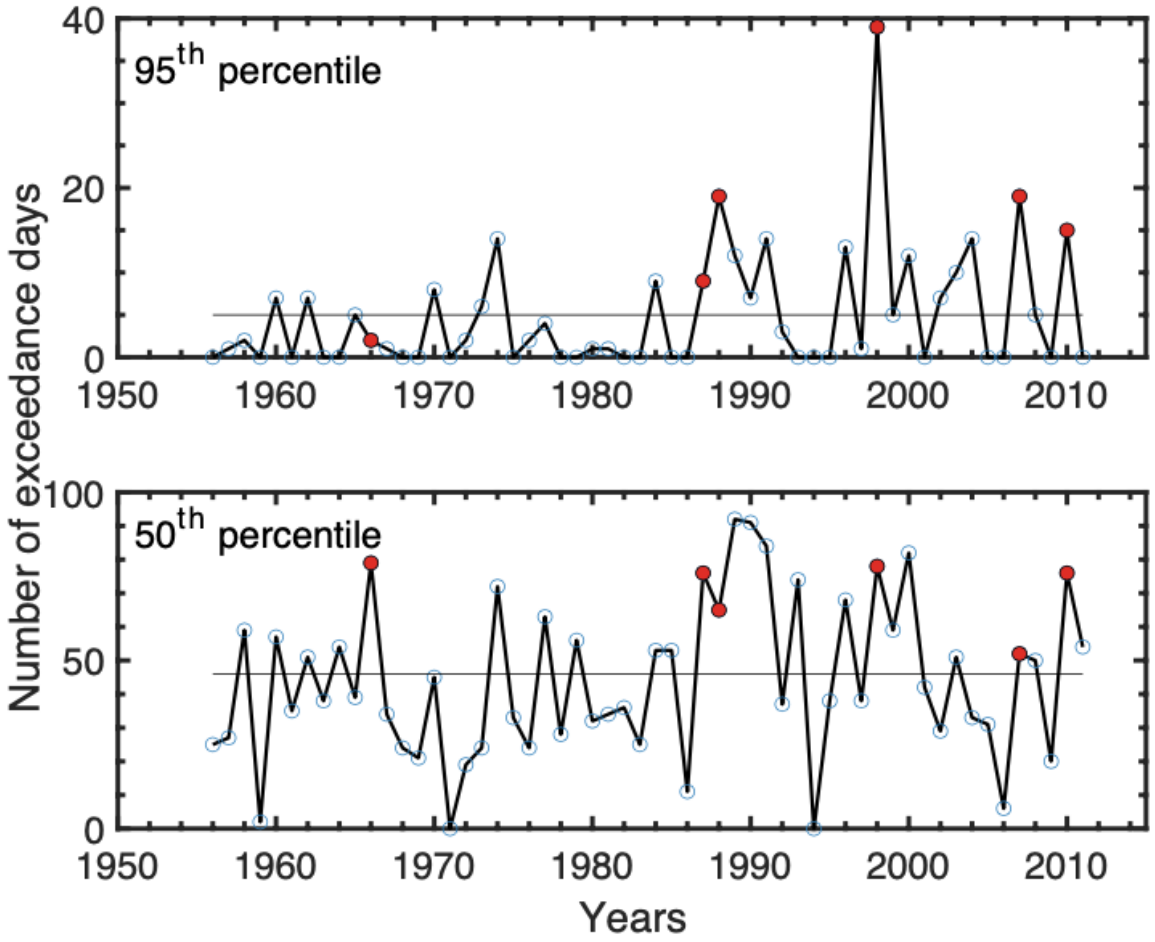

Figure B.5 Total number of days in JAS in which daily flows at Bahadurabad exceeded the 95th percentile (top panel) and 50th percentile (lower panel) flow for the same day (1956-2011 C.E.). The 95th and 50th percentile daily flows were calculated between 1956 and 2011 C.E. The horizontal lines at 5 days and 46 days on the upper and lower panels represent 5% and 50% of the total of 92 days between July and September, and are the average exceedance days expected by chance in any given year. Red filled in circles indicate known instrumental period flood years in 1966, 1987, 1988, 1998, 2007, and 2010 C.E. Note that in 1966 C.E. daily flow never exceeded the 95th percentile of daily flow.

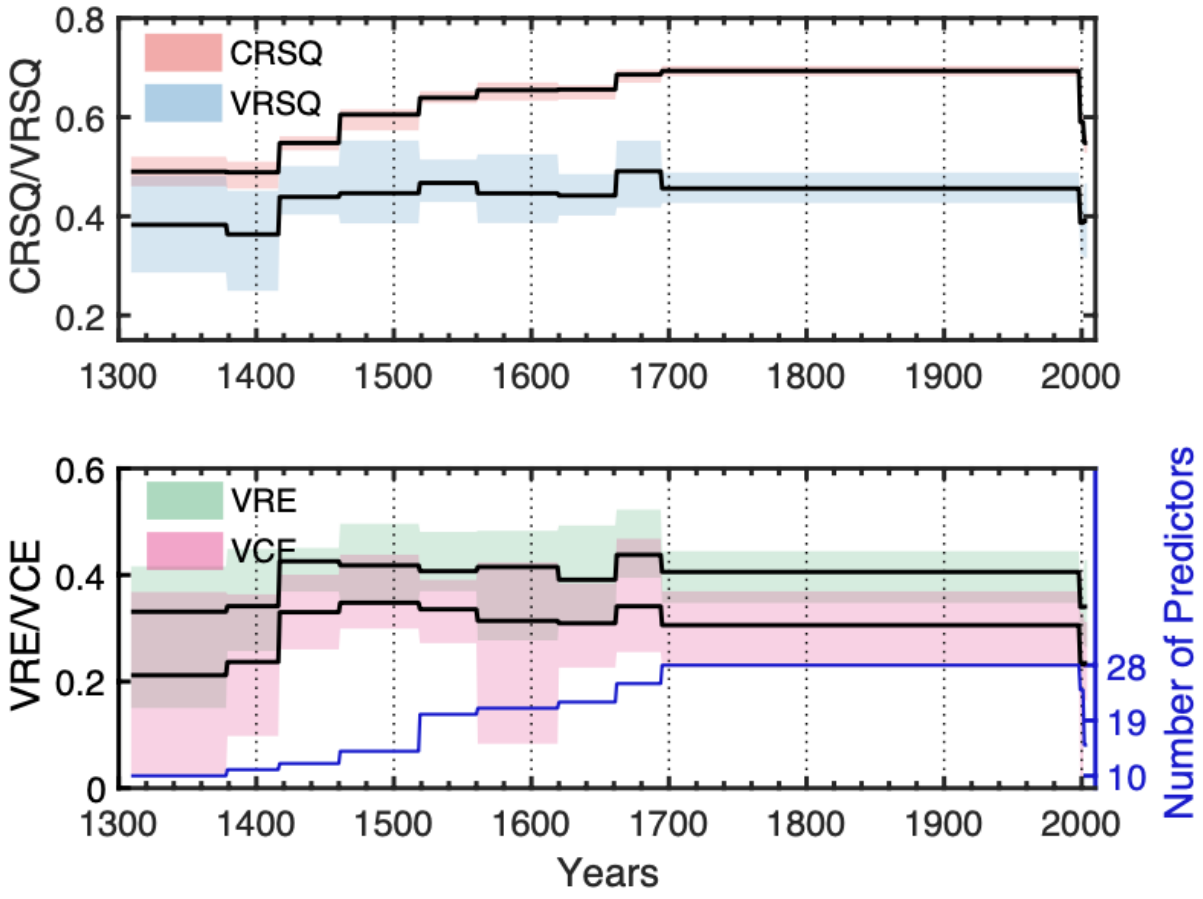

Figure B.6 Calibration and validation statistics of the mean JAS discharge reconstruction of the Brahmaputra River at Bahadurabad, Bangladesh along with the number of tree ring series used as predictors in each nest. The shaded uncertainties represent the range of variation in the statistic depending on the choice of correlation weight used in the Principal Components matrix weighting procedure (see Methods section). CRSQ - calibration period coefficient of multiple determination; VRSQ - validation period square of the Pearson correlation; VRE - validation period reduction of error; and VCE validation period coefficient of efficiency. VRE and VCE values consistently greater than 0 suggest reconstruction skill. The median value of each statistic are: i. CRSQ: 65.58%, ii. VRSQ: 45.61 %, iii. VRE: 0.41, and iv. VCE: 0.31.

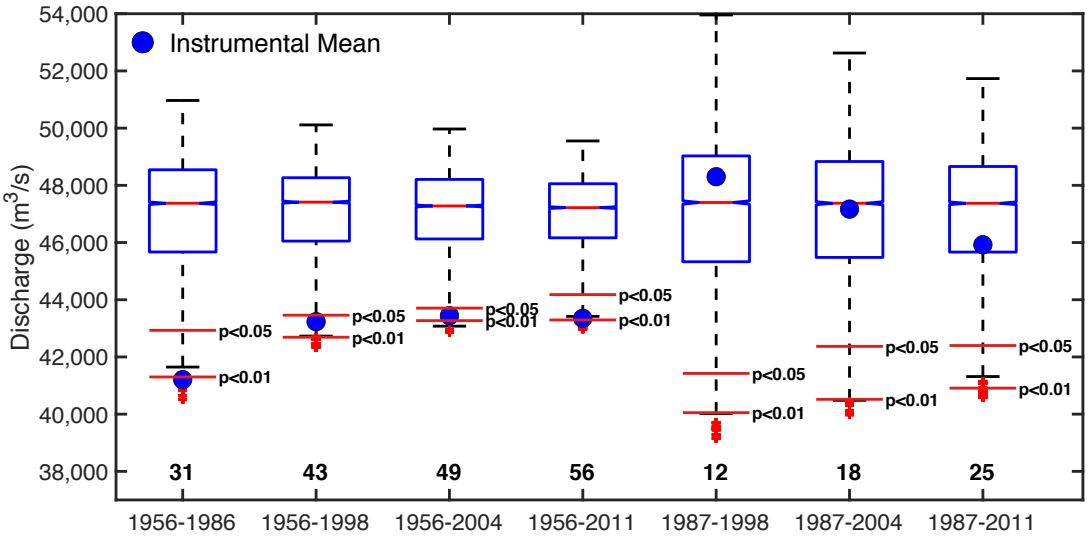

Figure B.7 Comparison between mean instrumental JAS Brahmaputra River discharge at 7 different time intervals (1956-1986; 1956-1998; 1956-2004; 1956-2011; 1987-1998; 1987-2004; and 1987-2011) as filled blue dots against distributions of the mean reconstructed discharge in 10,000 random draws of blocks of same length from the reconstruction. The block length used in each draw is mentioned below each box plot. The two red horizontal lines indicate the threshold for mean discharge to be significantly drier than reconstructed discharge at p<0.05 and p<0.01. The plot suggests that the first 31 years of instrumental discharge between 1956-1986 were exceptionally dry (p<0.05) while discharge since 1987 C.E. aligns more closely with mean reconstructed discharge rates in the context of the past 7 centuries.

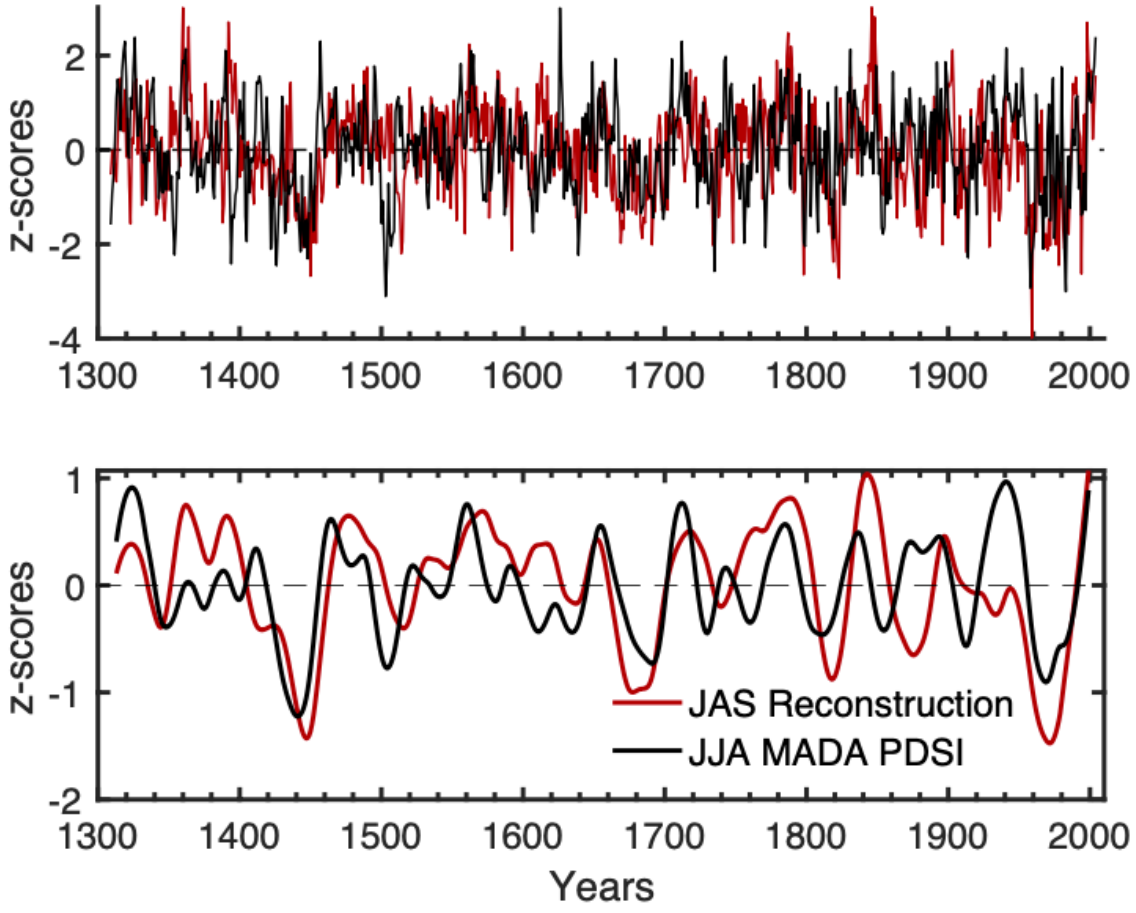

Figure B.8 A comparison between standardized versions of our JAS discharge reconstruction at Bahadurabad (in red) and a spatial average of the June-July-August (JJA) mean Palmer Drought Severity Index (PDSI) over the Brahmaputra watershed reconstructed by the Monsoon Asia Drought Atlas [MADA - *Cook et al.*, 2010a] between 1309-2004 C.E. (Pearson r=0.27, n=696, p<0.001). While both datasets share many of the underlying predictors, they have different reconstruction target fields (Brahmaputra discharge vs gridded PDSI) and were produced using different reconstruction methods (Bayesian Regression vs spatial point-by-point regression). The lower panel compares 50-year low-pass filtered versions of both reconstruction highlighting that multi-decadal dry and wet periods over the basin suggested by our JAS reconstruction are also suggested by larger scale reconstructions of spatial drought variability. The 2 low-pass filtered series correlate at 0.52. While the low-pass filtered versions of the reconstructions show good visual correspondence, we note that this correlation is not 'statistically significant' at p<0.05 using a 2-tailed t-test considering the small effective sample size of 13.9 years (calculated as 696/50). The correlation needed for a p<0.05 for a sample size of 13.9 is 0.5342. The wet and dry periods we observe here also largely consistent with those found by refs. [*Chen et al.*, 2020; *He et al.*, 2018; *Shi et al.*, 2018a; *Wang et al.*, 2020].

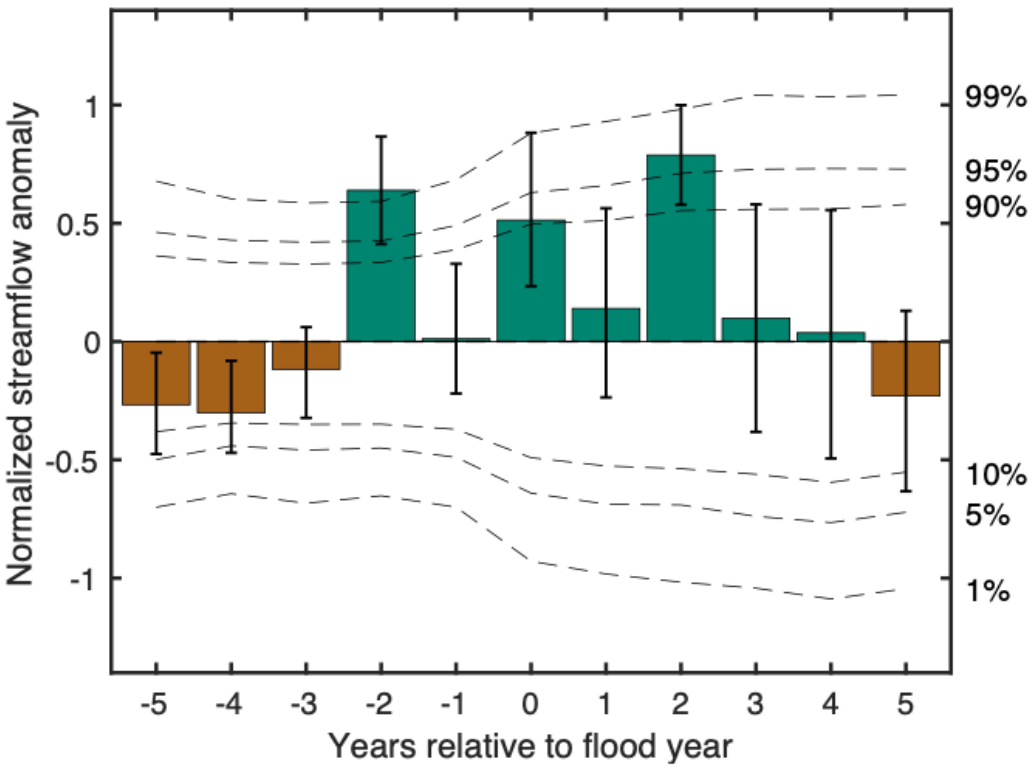

Figure B.9 Superposed Epoch Analysis (SEA) for discharge in 12 historical flood years that occurred prior to the start of instrumental observations in 1956 C.E. The vertical lines on the response bars are the 5th, 50th, and 95th percentiles of mean flow across 495 unique draws of 8 flood years at random out of 12. The horizontal dotted lines indicate the threshold required for epochal anomalies to be statistically significant using random bootstrapping at three different statistical thresholds. These thresholds were calculated by compositing 10,000 draws of 8 years at random (or 'pseudo-flood years') from the reconstruction between 1780 and 2004. The relationship between high discharge during flood years in much weaker than that for just the instrumental period flood years (Main Text, Fig. 2b) and for all 16 flood years (Main Text, Fig. 4a). The median response of the 495 unique draws of 8 flood years out of 12 is not significant at $p<0.05$ when compared to 10,000 draws of 8 'pseudo-flood' years at random.

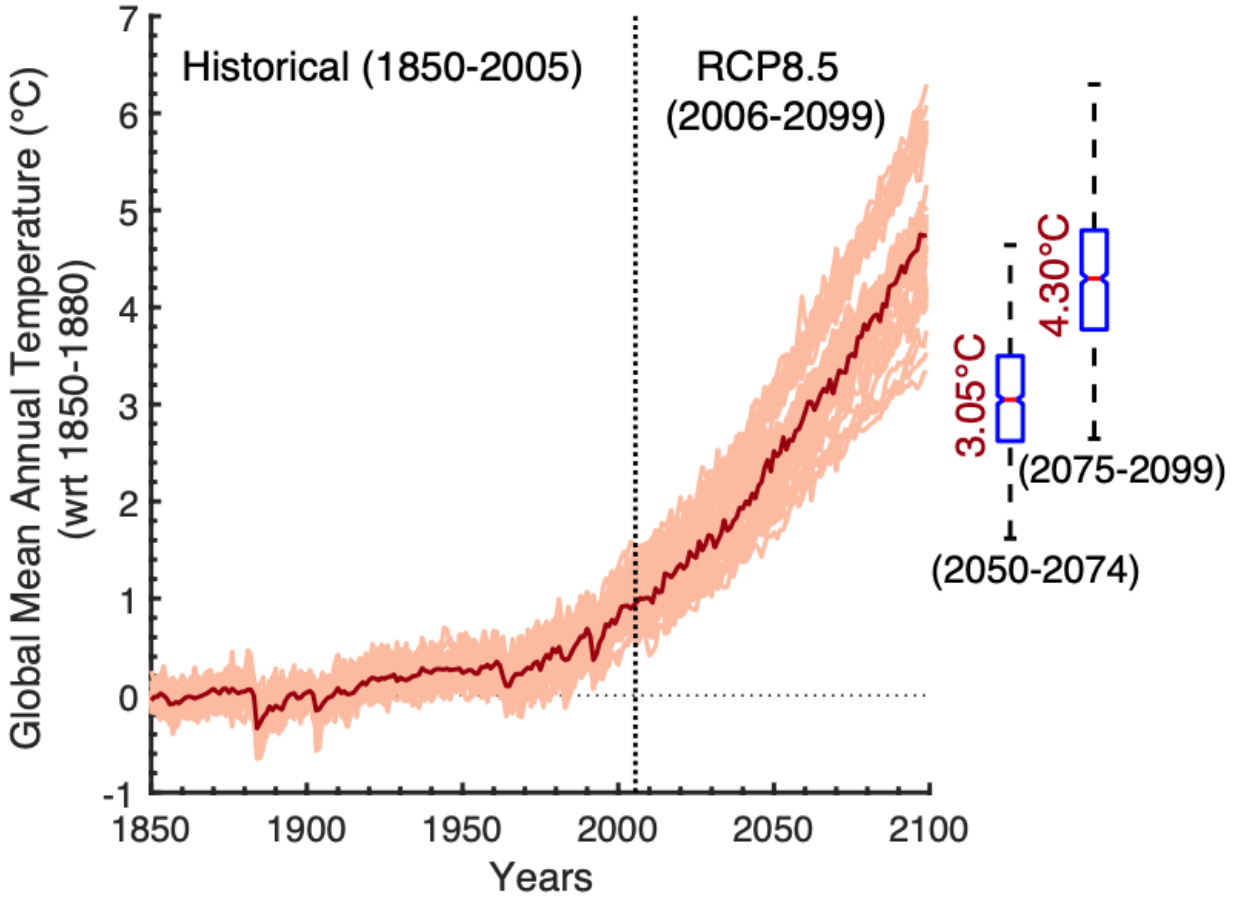

Figure B.10 Expected change in global mean annual surface temperature between 2050-2074 C.E. and 2057-2099 C.E. relative to pre-industrial 1850-1880 C.E. mean conditions using CMIP-5 RCP8.5 projections. The multi-model median warming for these two periods is projected to be 3.05°C and 4.30°C respectively. We used the same suite of 20 models and 42 ensemble members an in our modelled runoff calculations for this analysis. The full list of models and the respective ensemble members can be found in Table B.1.

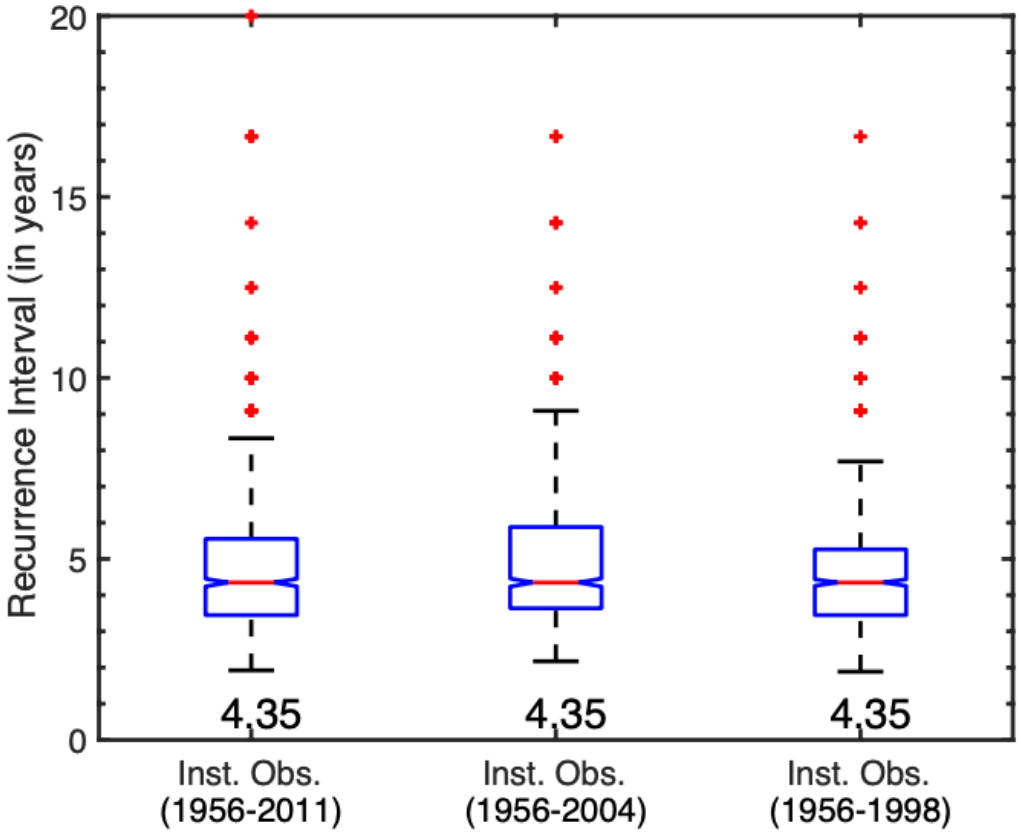

Figure B.11 Recurrence interval (in years) of discharge greater than the 2007 flood year in three different time periods of the observed instrumental data, i. 1956-2011 C.E., ii. 1956-2004 C.E., and iii. 1956-1998 C.E. The first period includes all instrumental observations, the second is the period of overlap between the instrumental observations and the reconstruction, and the third is the calibration-validation period for the reconstruction. The median recurrence interval is 4.35 for all three time periods, though there are slight differences in the range of variability across the 1,000 draws of 30-years with replacement. We note that the lack of difference in the median return interval could be in part due the short instrumental series.

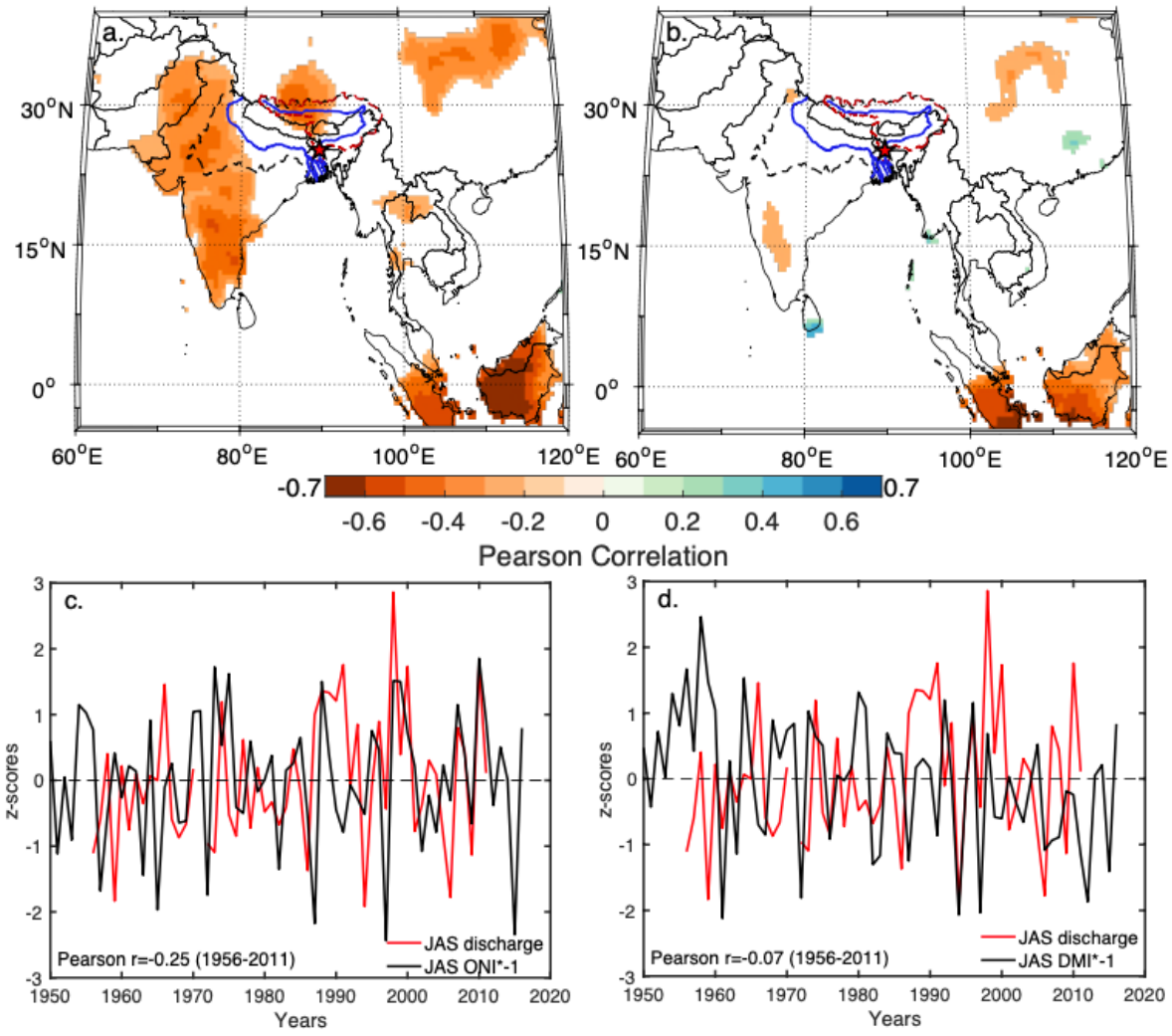

Figure B.12 Spatial correlation between mean JAS CRU Ts 4.01 precipitation and (a) mean JAS Oceanic Niño Index (ONI) and (b) mean JAS Indian Ocean Dipole (IOD) conditions based on the Dipole Mode Index (DMI) between 1950-2016 C.E. Over South Asia, correlations between JAS precipitation and ONI are the strongest over western India and Pakistan and are largely located outside the Brahmaputra basin. Correlations between DMI and regional precipitation are largely insignificant. Only correlations significant at p<0.05 using a 2 tailed t-test are shown in (a) and (b). The two lower panel plots show standardised anomalies of mean JAS Brahmaputra discharge at Bahadurabad plotted against standardised anomalies (c) JAS ONI and (d) JAS DMI. Neither correlation is significant at p<0.05 using a 2-tailed t-test, though we note that the relationship in c. may be non-stationarity. Note that ONI and DMI indices are multiplied by -1 in c and d. ONI data is available here: https://catalog.data.gov/dataset/climate-prediction-center-cpcoceanic-nino-index, and DMI data at this link: https://psl.noaa.gov/gcos_wgsp/Timeseries/DMI/.

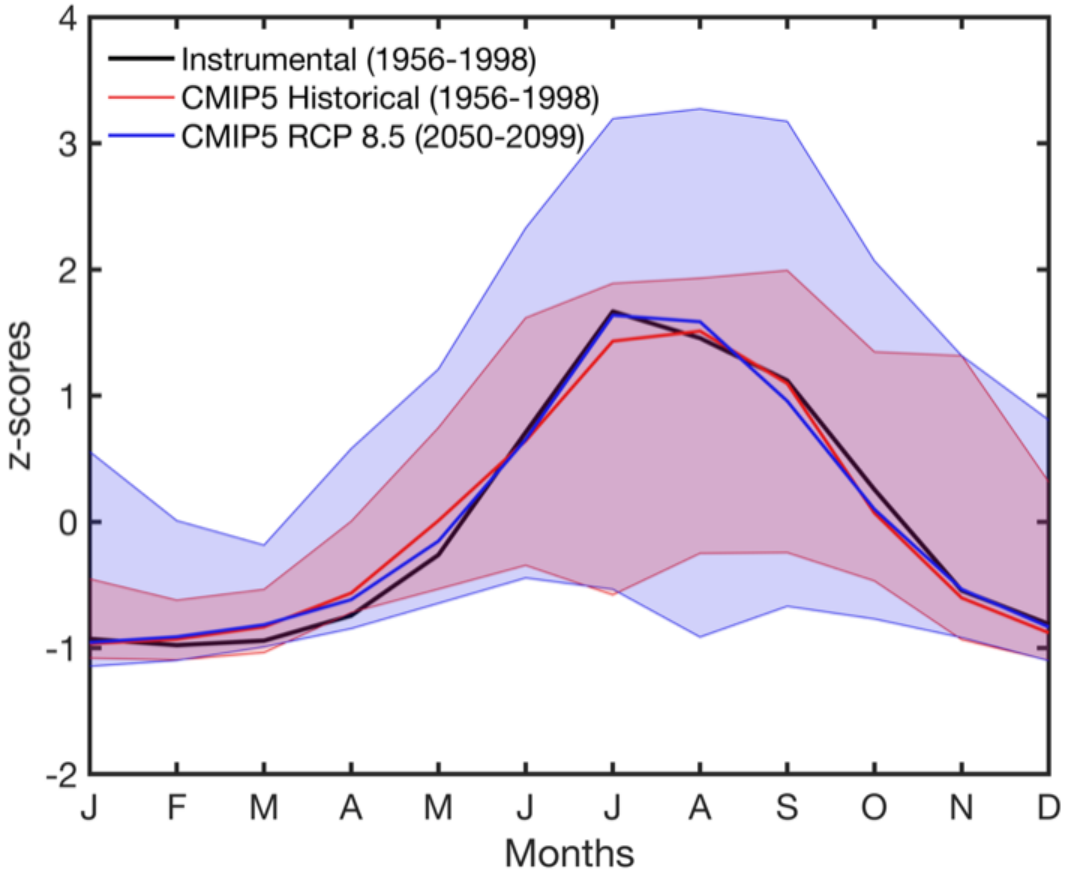

Figure B.13 Standardized anomalies of annual mean discharge of the Brahmaputra River at Bahadurabad, Bangladesh between 1956-1998 C.E. (in black) compared against standardized anomalies of annual runoff integrated over the Brahmaputra watershed upstream of Bahadurabad from the CMIP5 climate model suite between 1956-1998 C.E. from the 'historical' simulation period (multi-model ensemble median in red) and 2050-2099 C.E. from the RCP8.5 simulation (multi-model ensemble median in blue). The shaded envelope represents the 10th and 90th percentiles across all 42 model simulations.

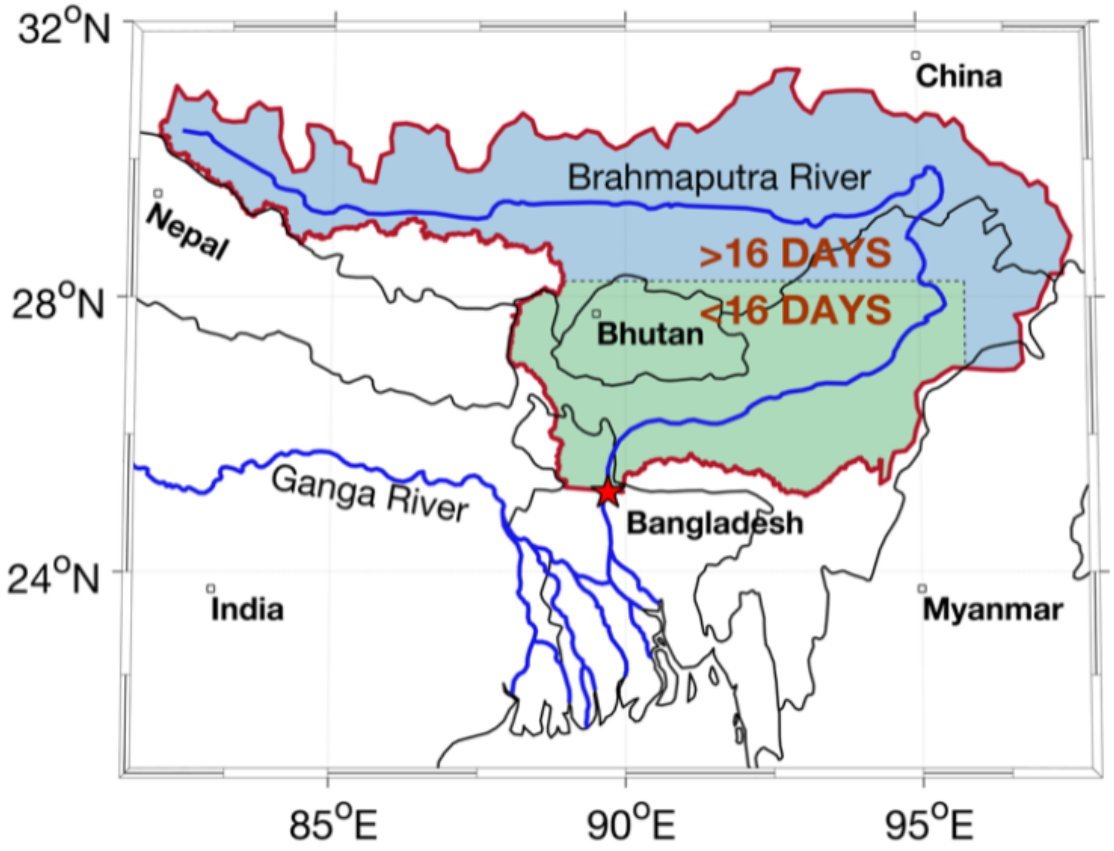

Figure B.14 Spatial partitioning of the Brahmaputra watershed into an upper and lower section (in blue and green respectively) based on the number of days discharge at a given location would take to eventually make it to the Brahmaputra River at the gauging station Bahadurabad, Bangladesh (red star). The partitioning of the watershed was based on daily isochrone maps developed by refs. - [*Jian et al.*, 2009; *Webster et al.*, 2010] and converted to two sections to account for that CMIP 5 runoff data was only available at a monthly resolution, and therefore and discharge at Bahadurabad arriving from the upper section of the watershed is in fact runoff from the previous month.

Table B.1. Tree-ring predictors used in mean JAS Brahmaputra discharge reconstruction. Pearson correlation between each predictor and JAS discharge, and predictor principal component (PC1 & PC2) loadings are calculated between 1956-1998. *Lag t+1 predictors. +The two chronologies from Myanmar are new series developed by co-authors. TRW - Tree Ring Width, LWW - Late Wood Width.

	Country	Site	Species	Start Year	End Year	Lat (°)	Lon (°)	Pearson ρ	PC1 loading	PC2 loading	Distance from watershed (km)	Reference
1+	Myanmar	Chin Hills	*Pinus kesiya, TRW*	1695	2013	21.22	94.02	0.26	0.11	0.55	443	-
2+	Myanmar	Chin Hills	*Pinus kesiya, LWW*	1695	2013	21.22	94.02	0.46	0.47	0.51	443	-
3	Nepal	Chardung	*Abies spectabilus*	1689	1998	27.17	86.42	0.35	0.56	0.11	157	[*Cook et al.*, 2003]
4*	China	Xinlong	*Abies forrestii*	1663	2007	30.87	100.28	0.49	0.44	0.5	329	[*Cook et al.*, 2013a]
5	Bhutan	Ghasa	*Juniperus recurva*	1660	2006	27.92	89.75	0.38	0.42	-0.3	within	[*Cook et al.*, 2010a] [*Cook et al.*, 2011c]
6	Bhutan	Laya	*Larix griffithiana*	1644	2006	27.98	89.75	0.33	0.63	-0.22	within	[*Cook et al.*, 2010a]; [*Cook et al.*, 2011b]
7	Bhutan	Chele La	*Larix griffithiana*	1620	2005	27.38	89.32	0.53	0.69	0.24	within	[*Cook et al.*, 2010a]; [*Cook et al.*, 2011a]
8	Nepal	Lamite Bhajyung	*Abies spectabilus*	1561	1999	27.48	87.90	0.47	0.58	0.09	16	[*Krusic*, 2005c]
9*	China	Hebei Low	*Juniperus przewalskii*	1520	2002	34.78	100.82	0.53	0.89	-0.15	669	[*Cook et al.*, 2013a]
10	China	Shangri La	*Abies forrestii*	1516	2007	27.62	99.80	0.31	0.41	0.43	244	[*Cook et al.*, 2010a]; [*Wright et al.*, 2011]
11	Nepal	Eastern Nepal	*Abies spectabilus*	1509	1999	27.73	87.20	0.38	0.44	0.09	85	[*Krusic*, 2005b]
12*	China	Maxiong Valley	*Abies forrestii*	1509	2006	29.15	99.93	0.34	0.09	0.71	229	[*Li et al.*, 2017]
13	Nepal	Yalung Khola	*Tsuga dumosa*	1500	1999	27.83	88.02	0.39	0.49	-0.02	14	[*Krusic*, 2005a]
14*	China	Hebei High	*Juniperus przewalskii*	1500	2002	34.78	100.82	0.29	0.55	-0.32	669	[*Cook et al.*, 2013a]
15*	Bhutan	Dhur	*Juniperus recurva*	1462	2014	27.72	90.68	-0.30	-0.45	0.1	within	[*Krusic et al.*, 2015]
16	Nepal	Dobini Danda	*Juniperus recurva*	1445	1998	27.43	86.20	0.53	0.78	-0.12	161	[*Cook et al.*, 2003]
17	Nepal	Bhule Pokari	*Juniperus recurva*	1417	1998	27.42	86.27	0.42	0.59	-0.2	162	[*Cook et al.*, 2003]; [*Krusic and Cook*, 2002]
18*	China	Maxiong Valley All	*Abies forrestii*	1380	2007	29.15	100.00	0.29	0.14	0.82	235	[*Li et al.*, 2017]
19*	China	Hebei Median	*Juniperus przewalskii*	1310	2002	34.78	100.82	0.41	0.7	-0.22	669	[*Cook et al.*, 2013a]
20*	China	Zaduo	*Juniperus przewalskii*	1290	2006	32.67	95.72	0.40	0.48	-0.21	229	[*Cook et al.*, 2013a]
21*	China	ZD31	*Juniperus spp.*	1290	2006	32.67	95.72	0.40	0.48	-0.21	229	[*Cook et al.*, 2013a]
22*	China	QML-ZD31	*Juniperus spp.*	1290	2006	32.73	95.83	0.29	0.47	-0.41	238	[*Cook et al.*, 2013a]
23*	China	Central Tibet	*Juniperus tibetica*	1285	2008	29.35	92.00	0.27	0.13	0.5	within	[*Cook et al.*, 2013a]
24*	Nepal	Eastern Nepal	*Tsuga dumosa*	1260	1999	27.45	87.00	-0.30	-0.2	-0.35	103	[*Cook et al.*, 2013a]
25*	China	TDC	*Juniperus przewalskii*	1130	2002	35.07	100.35	0.46	0.71	-0.3	665	[*Cook et al.*, 2013a]
26	China	Maquina-A	*Juniperus przewalskii*	1082	2001	35.07	100.35	-0.32	-0.1	-0.47	665	[*Gou et al.*, 2007] [*Li et al.*, 2017]
27	China	Maquina-C	*Juniperus przewalskii*	1082	2001	35.07	100.35	-0.38	-0.33	-0.38	665	[*Gou et al.*, 2007] [*Li et al.*, 2017]
28*	China	Qamdo	*Juniperus tibetica*	449	2004	31.12	97.03	0.34	0.31	0.27	140	[*Cook et al.*, 2013a]

Table B.2 List of CMIP5 models[*Taylor et al.*, 2012] used in Brahmaputra discharge simulations and in the estimates of global mean annual temperature change. We used model and its respective scenario run only if it extended through both the historical (1850-2005) and RCP8.5 (2006-2099) simulation period. For each model we first calculated the median discharge projection across ensemble members within each model, and only then calculated the median and interquartile range across models. We did this to ensure that each of the 20 models are represented equally in the final multi-model ensemble estimate.

	Model Name	**Scenarios**	**Modelling Center**
1.	ACCESS1-0	r1i1p1	Centre for Australian Weather and Climate Research (CAWCR)
2.	ACCESS1-3	r1i1p1	
3.	bcc-csm1-1	r1i1p1	Beijing Climate Center, China Meteorological Administration (CMA)
4.	CanESM2	r1i1p1; r2i1p1; r3i1p1; r4i1p1; r5i1p1	Canadian Centre for Climate Modelling and Analysis
5.	CCSM4	r1i1p1; r2i1p1; r3i1p1; r4i1p1; r5i1p1; r6i1p1	NCAR/UCAR Community Climate System Model
6.	CNRM-CM5	r1i1p1; r2i1p1; r4i1p1; r6i1p1	Centre National de Recherches Meteorologiques / Centre Europeen de Recherche et Formation Avancees en Calcul Scientifique (CNRM/CERFACS)
7.	FIO-ESM	r2i1p1; r3i1p1; r2i1p1; r3i1p1	First Institute of Oceanography, State Oceanic Administration, China
8.	GFDL-ESM2G	r1i1p1	NOAA Geophysical Fluid Dynamics Laboratory
9.	GFDL-ESM2M	r1i1p1	
10.	GISS-E2-R	r1i1p1	NASA Goddard Institute for Space Studies
11.	inmcm4	r1i1p1	Institute for Numerical Mathematics
12.	IPSL-CM5A-LR	r1i1p1; r2i1p1; r3i1p1; r4i1p1	Institut Pierre-Simon Laplace
13.	IPSL-CM5A-MR	r1i1p1	
14.	IPSL-CM5B-LR	r1i1p1	
15.	MIROC-ESM	r1i1p1	Atmosphere and Ocean Research Institute (The University of Tokyo), National Institute for Environmental Studies, and Japan Agency for Marine-Earth Science and Technology
16.	MIROC-ESM-CHEM	r1i1p1	
17.	MIROC5	r1i1p1. r2i1p1; r3i1p1	
18.	MPI-ESM-LR	r1i1p1; r2i1p1; r3i1p1	Max Planck Institute for Meteorology (MPI-M)
19.	MRI-CGCM3	r1i1p1	Meteorological Research Institute
20.	NorESM1-M	r1i1p1	Norwegian Climate Centre (NorClim)
		Total: 42	

Appendix C

Text C.1

The Palmer Drought Severity Index (PDSI) is a metric of wet and dry conditions, with increasingly positive (negative) values representing wet (dry) conditions. The most important variables involved in its calculation are precipitation and evapotranspiration [*Schrier et al.*, 2006]. PDSI has high inherent autocorrelation, and values for a given month or season integrate precipitation and evapotranspiration anomalies over the preceding months [*Dai*, 2011]. Thus, while tree growth and climate relationships may reflect diverse seasonality [*Fritts*, 1976], the high month-to-month persistence of PDSI allows for the reconstruction of JJA season PDSI in the 'drought atlas' [see *Cook et al.*, 1999a; *Cook et al.*, 2015b]. Nevertheless, the original climate-growth seasonality remains embedded within the drought atlas [*George et al.*, 2010]. Consequently, the JJA PDSI reconstruction in the OWDA reflects climate across multiple preceding seasons, that must be taken into account while analyzing the post-volcanic eruption response.

To interpret the seasonality of climate embedded in the OWDA JJA PDSI reconstruction we calculate Pearson correlations between instrumental gridded climate (CRU temperature and precipitation) across multiple seasons (prior fall, winter, spring and summer) between 1901-1978. Because the reconstructed PDSI in the pre-1979 period is estimated solely from tree rings [*Cook et al.*, 2015b], we use the 1901-1978 time period for the correlation analysis. We also show the correlation between gridded instrumental precipitation and temperature to better understand how the two are related, as soil moisture-precipitation-temperature feedbacks play an important role in modulating drought impacts in the region [*Fischer et al.*, 2007a; *Seneviratne et al.*, 2006].

The *Pauling et al.* [2006] precipitation reconstruction is largely independent (i.e. number of shared common predictors) to the OWDA, and is based on instrumental series, documentary series, and multi-proxy series (tree-rings, corals, and one speleothem). It reconstructs precipitation for four distinct seasons, namely winter (DJF – December through February), spring (MAM – March through May), summer (JJA – June through August), and fall (SON – September through November). The volcanic response in *Pauling et al.* [2006] has been presented in *Fischer et al.* [2007b], however, we document the response using an updated list of 'key years' (see Table S1) that have become available more recently [*Plummer et al.*, 2012; *Sigl et al.*, 2013; *Sigl et al.*, 2015]. Using the OWDA we can study the volcanically forced hydroclimate response over the past millennium, include an additional 7 eruptions, notably the two major eruptions of Samalas in 1257, and Kuwae in 1458 (Table S1), that otherwise is not possible with the *Pauling et al.* [2006] precipitation reconstruction. Possible key years for the OWDA and *Luterbacher et al.* [2016] temperature include eruptions between 1100-1991 C.E., and include eruptions between 1500-1991 C.E. for *Pauling et al.* [2006] precipitation. In our study we limit our analyses to large tropical volcanic eruptions, as the winter climate response over Europe may differ for tropical and northern hemisphere extratropical eruptions [*Robock*, 2000] and might confound the spring and summer hydroclimate signal observed in the reconstructions due to integrative nature of soil-moisture.

Text C.2

The National Oceanic and Atmospheric Administration – Climate Prediction Center (NOAA-CPC) teleconnection index data for North Atlantic Oscillation (NAO) and the East Atlantic Pattern (EAP) become available only after 1949. These indices are calculated by conducting rotated principal components analysis (RPCA) of standardized monthly 500 hPa geopotential heights (GPH) over the northern hemisphere [*Barnston and Livezey*, 1987]. Using the same procedure, we develop an estimate of the EAP extending back to 1766 C.E., by conducting varimax RPCA on a 500 hPa geopotential heights (GPH) reconstruction for Europe and the North Atlantic, based solely on long instrumental records of climate, developed by *Casty et al.* [2007]. To be consistent with the NOAA-CPC data, we perform the RPCA on the *Casty et al.* [2007] monthly 500 hPa GPH anomalies, standardized using January 1950 through December 2000 base period monthly mean and standard deviations for each grid cell, and weight grid cell by the square root of the cosine of its latitude.

The first rotated empirical orthogonal function (REOF) loadings that emerge from the RPCA shows a strong north-south, negative-positive, dipole between Iceland and Azores Islands. This pattern explains 28% of the variance in the dataset (Figure C.7). Its corresponding standardized Principal Component (PC) scores correlate significantly with the monthly NOAA-CPC NAO index (r=0.75, p=0, N=636, N effective for autocorrelation (N')=609, 2-sided Students' t-test) between 1950 and 2002. The fourth EOF loading explains 26% of the total variance, shows a south-eastward displaced dipole compared to EOF1. Its corresponding standardized PC time-series correlates significantly with the monthly NOAA-CPC EAP index dataset (r=0.73, p=0, N=636, N'=614, 2-sided Student's t-test) between 1950 and 2002.

Consequently, we interpret the first and fourth EOF modes and corresponding PC time-series to represent estimates of monthly NAO and EAP respectively back to 1766.

The estimated mean April through July (AMJJ) EAP between 1800 to 2002 using standardized PC4 scores is shown in Figure 3.5b of the main text. This longer time-series allows us to study post-eruptive response of mean AMJJ EAP following large volcanic eruptions that occurred during the nineteenth century prior to 1950 (1809 – unknown, 1815 – Tambora, Babuyan – 1831, Cosiguina – 1835, and 1883 – Krakatau), the period for which the NOAA-CPC EAP index data are available. However, it should be noted that the number of pressure gauge stations in the *Casty et al.* [2007] 500 hPa GPH reconstruction decline rapidly prior to 1870 (their Figure 1a), and thus our estimate of past EAP variability (main text Figure 3.5b) should be viewed with caution, considering the uncertainties regarding the spatio-temporal stationarity of past estimates of teleconnection variability [*Raible et al.*, 2014].

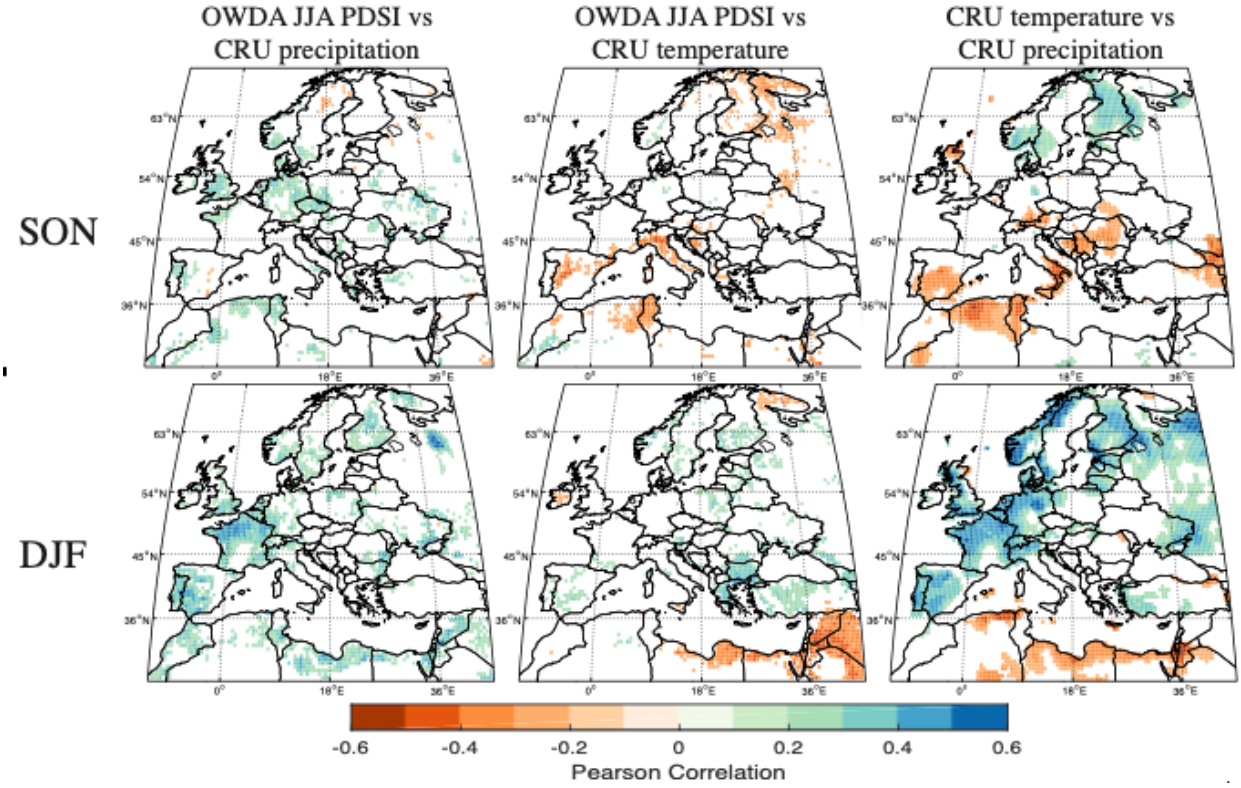

Figure C.1 Same as Figure 3.1 but for (top panel) mean September through November (SON), and (lower panel) December through February (DJF) seasons. Correlations are for the time period 1901-1978. Only correlations significant at p<0.05 (two-sided, Student's t-test) are shown.

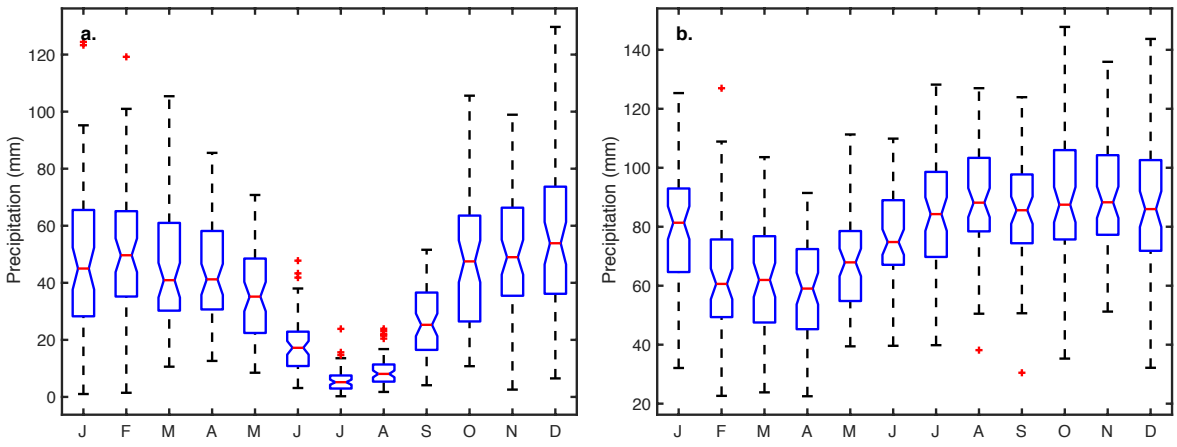

Figure C.2 Boxplot for CRU Ts 3.21 monthly precipitation between 1950-2012 averaged for the (a.) western Mediterranean (blue box in Figure 3.2) and (b.) northwestern Europe (red box in Figure 3.2). Note the different ordinate range. Based on the varying tree-growth climate response in different regions [Fritts, 1976], JJA OWDA PDSI primarily reflects MAM precipitation over western Mediterranean, and a combination of both MAM and JJA precipitation over northwestern Europe (Figure 3.1).

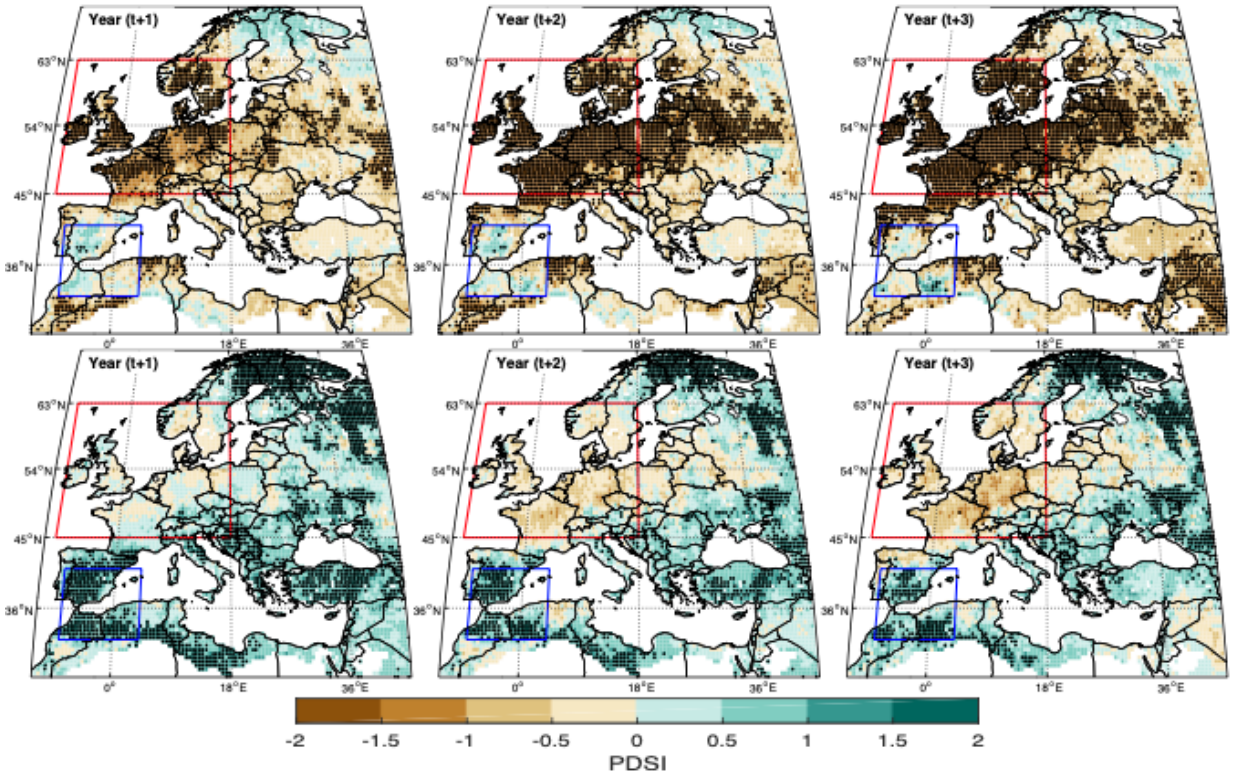

Figure C.3 Same as Figure 3.2, but showing the 10th (upper panel) and 90th percentile (lower panel) response based on multiple resampling of (n1=1,000) non-repeating subsets of n2=10 key years from the master key event year list (Table S1) for years t+1 through t+3 to determine the uncertainty in the response and sensitivity to a choice of a different set of key event years.

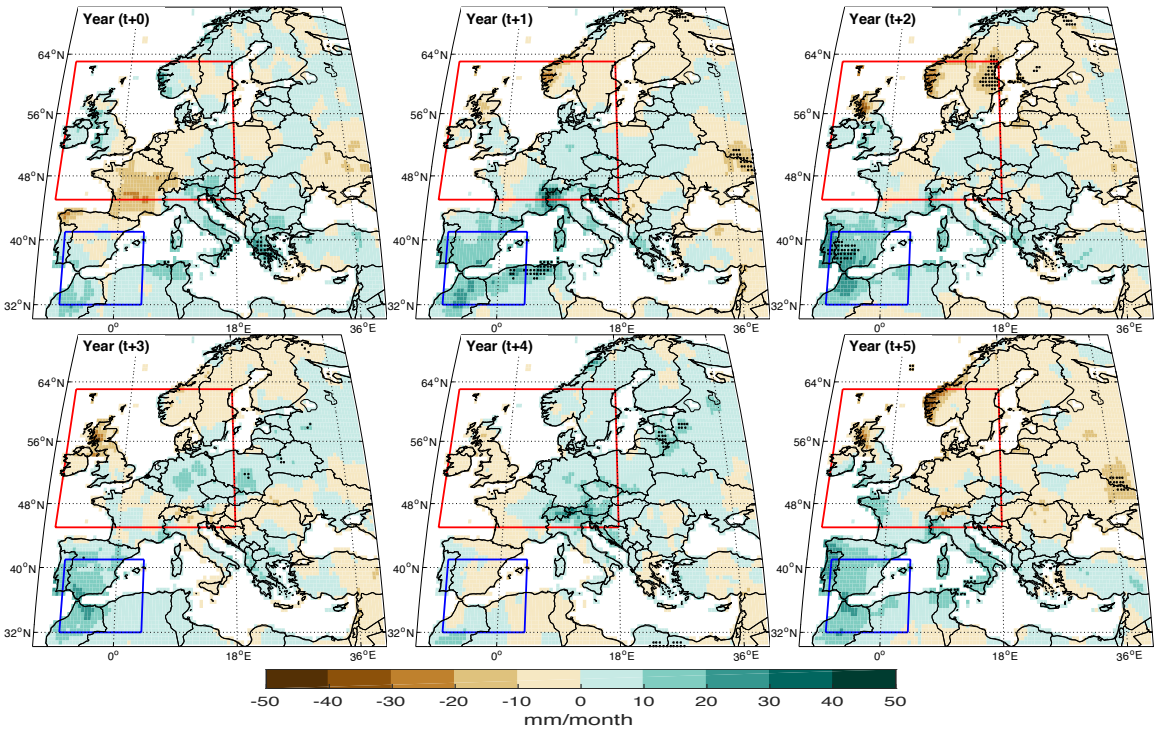

Figure C.4 Same as Figure 3.2 but median post-volcanic response for spring (MAM) precipitation in mm/month [Pauling et al., 2005] between 1500-2000 C.E. Significant ($p<0.05$ one-sided) positive or wet epochal are observed in the western Mediterranean in Year t+1 and t+2. Units are in mm/month. Shading in brown (green) indicated drying (wetting).

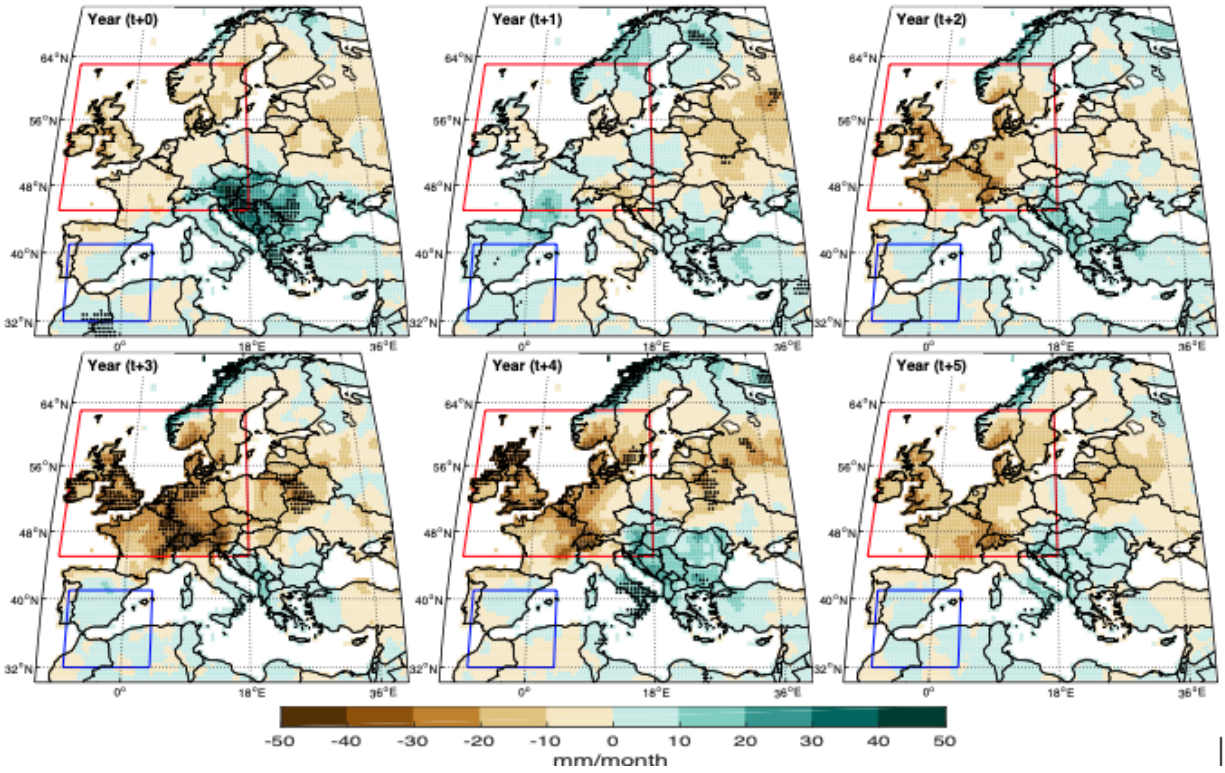

Figure C.5 Same as Figure 3.2 but median post-volcanic response for summer (JJA) precipitation in mm/month [Pauling et al., 2005] between 1500-2000 C.E. Significant ($p<0.05$ one-sided) negative or dry epochal are observed in northwestern Europe in Year t+3 and t+4. Units are in mm/month. Shading in brown (green) indicated drying (wetting).

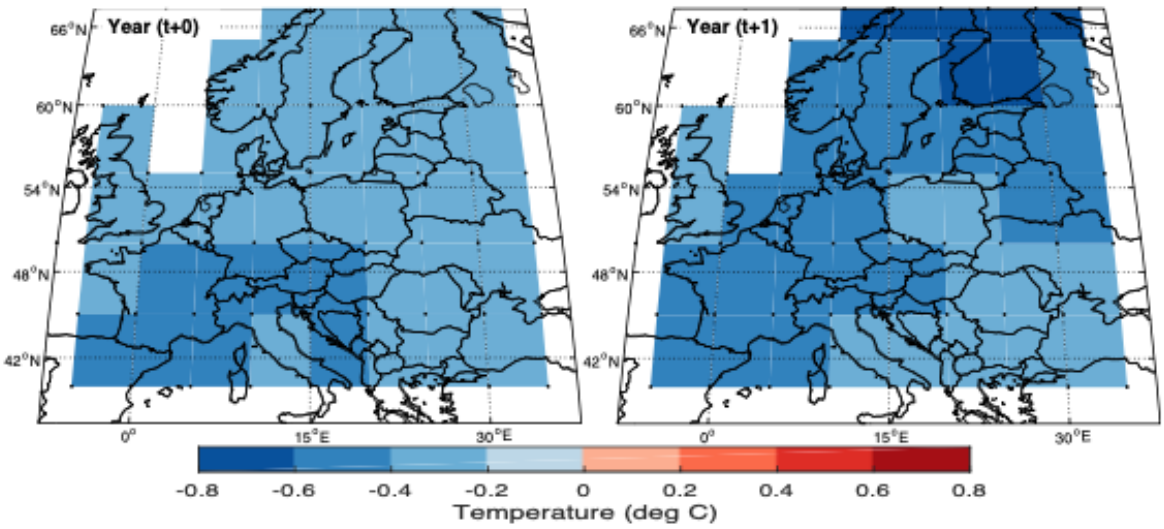

Figure 3.6 Same as Figure 2 showing median response for summer JJA temperature in [Luterbacher et al., 2016] for Years t+0 and t+1 for eruptions between 1100-2003 C.E. Units are in °C. Shading in blue (red) indicates cooling (warming). Widespread and significant ($p<0.05$ one-sided epochal anomalies) cooling is observed across the entire region in both years. While cool conditions persist for up to a decade after the eruptions (not shown), cooling is strongest and statistically significant ($p<0.05$ one-sided epochal anomaly) for every gridbox in the domain only in Years t+0 and t+1.

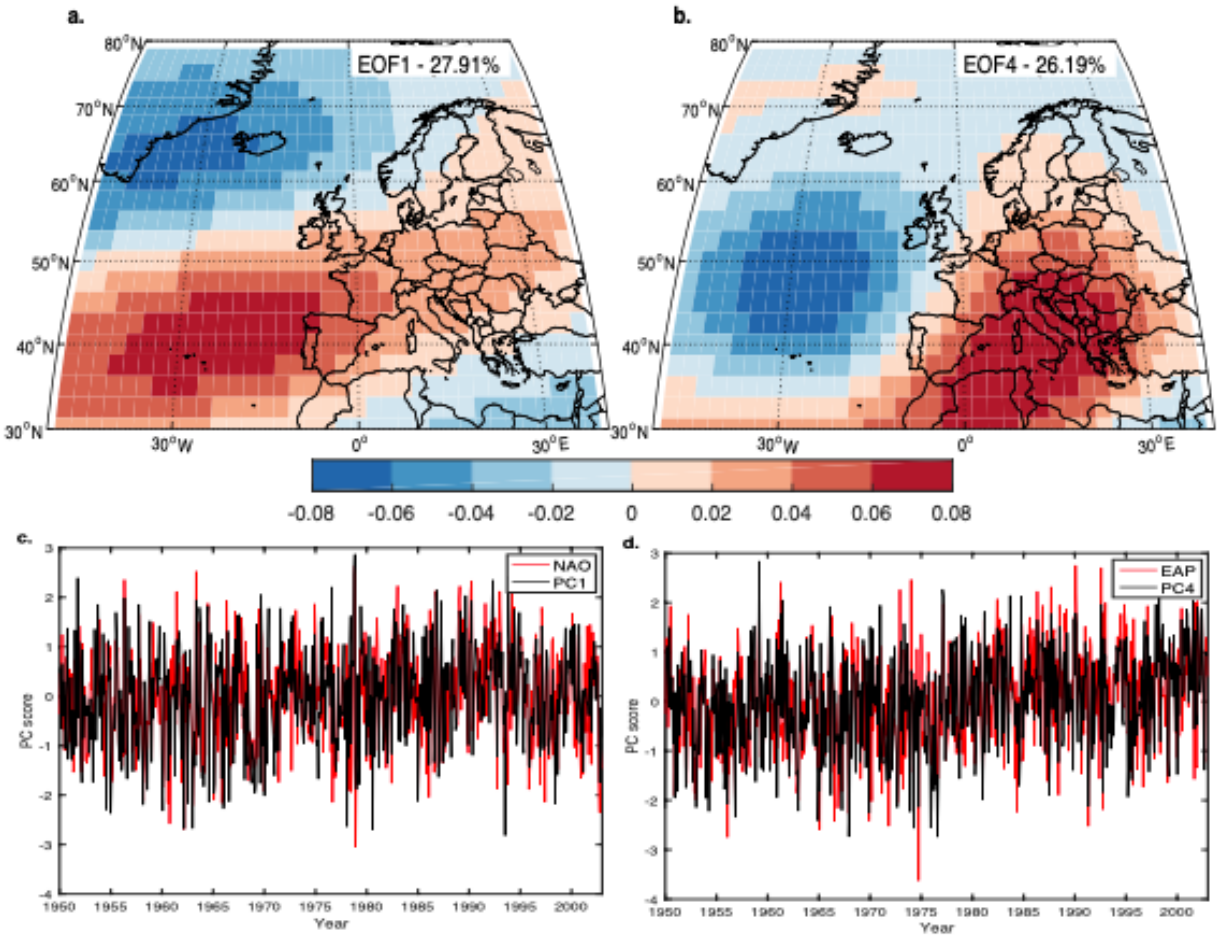

Figure C.7 Rotated Principal Components Analysis (RPCA) of *Casty et al.* [2007] monthly 500 hPa geopotential heights reconstruction (1765-2003) showing a.) first and b.) fourth spatial Rotated Empirical Orthogonal Function (REOF) loadings and the variance explained by each, along with corresponding c. and d. standardized principal component (PCs) scores between 1950-2002 (in black). Red lines represent monthly c.) North Atlantic Oscillation (NAO) and d.) East Atlantic Pattern (EAP) index data from the NOAA-CPC dataset for the same time period. Pearson correlations between c.) NOAA-CPC monthly NAO and PC1 and d.) NOAA-CPC monthly EAP and PC4 are 0.75 and 0.73 respectively (p=0, N=636, 2-sided Student's t-test).

Table C.1 Volcanic event years used to create the master key year list.

Study	**Volcanic event years** (last millennium only)
Sigl et al 2015 (n=12) Tropical events in Extended Data Table 4 global forcing >-9.4W/m^2	1108, 1171, 1230, 1258, 1286, 1345, 1458, 1601, 1641, 1695, 1809, 1815
Sigl et al 2013 (n=12) Deposition at ice cores WDC06A and NEEM S1 > 15kgSO_4/km^2	1169, 1229, 1258, 1285, 1344, 1458, 1594, 1600, 1694, 1809, 1815, 1991
Plummer et al 2012 (n=12) Deposition at ice cores Law Dome and NGRIP > 15kgSO_4/km^2	1168, 1229, 1257,1344, 1459, 1601, 1641, 1695, 1809, 1816, 1836, 1884
Gao + Crowley (n=11) Event years present in both Gao et al [2008] and Crowley and Unterman [2013]	1227, 1258, 1284, 1459, 1584, 1600, 1641, 1809, 1815, 1831, 1835